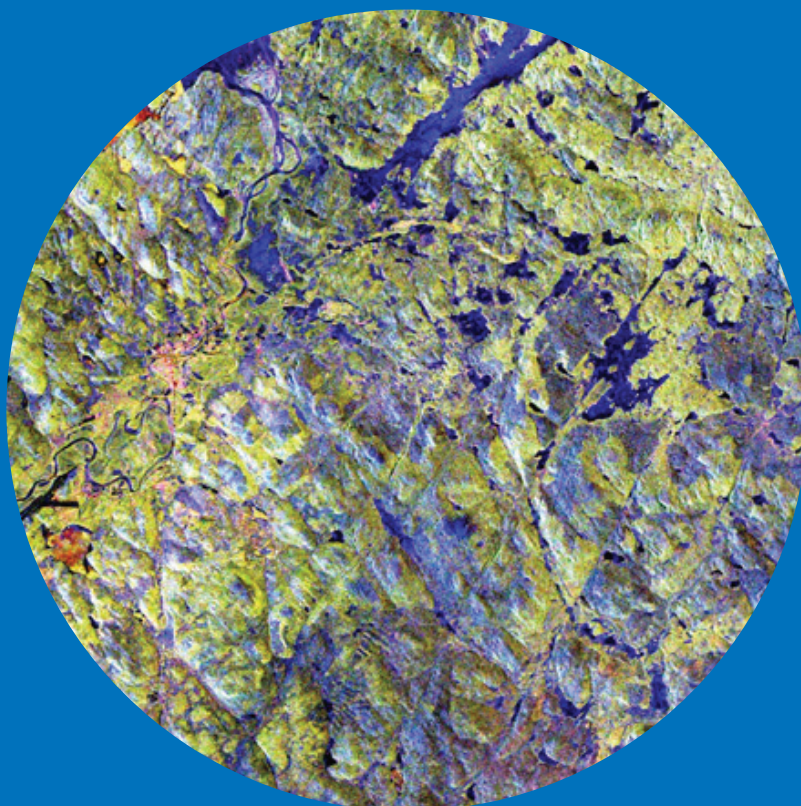


Department of Radio Science and Engineering

# Land cover and forest mapping in boreal zone using polarimetric and interferometric SAR data

---

Oleg Antropov





Land cover and forest mapping  
in boreal zone using  
polarimetric and  
interferometric SAR data

**Oleg Antropov**

A doctoral dissertation completed for the degree of Doctor of Science (Technology) to be defended, with the permission of the Aalto University School of Electrical Engineering, at a public examination held at the lecture hall S1 of the school on 14 January 2014 at 12.

**Aalto University**  
**School of Electrical Engineering**  
**Department of Radio Science and Engineering**

**Supervising professor**

Prof. Martti Hallikainen, Aalto University, Finland

**Preliminary examiners**

Prof. Erkki Tomppo, Finnish Forest Research Institute (Metla), Finland

Dr. Paul Siqueira, University of Massachusetts, USA

**Opponent**

Prof. Irena Hajsek, ETH Zürich, Switzerland, and German

Aerospace Center (DLR), Germany

Aalto University publication series

**DOCTORAL DISSERTATIONS 3/2014**

© Oleg Antropov

ISBN 978-952-60-5522-0

ISBN 978-952-60-5523-7 (pdf)

ISSN-L 1799-4934

ISSN 1799-4934 (printed)

ISSN 1799-4942 (pdf)

<http://urn.fi/URN:ISBN:978-952-60-5523-7>

Images: Fragment of polarimetric SAR mosaic over Saariselkä,  
shown in Pauli color-coded representation. Image processing © VTT.  
Data © JAXA and METI 2007

Unigrafia Oy  
Helsinki 2014

Finland



**Author**

Oleg Antropov

**Name of the doctoral dissertation**

Land cover and forest mapping in boreal zone using polarimetric and interferometric SAR data

**Publisher** School of Electrical Engineering

**Unit** Department of Radio Science and Engineering

**Series** Aalto University publication series DOCTORAL DISSERTATIONS 3/2014

**Field of research** Space technology

**Manuscript submitted** 12 August 2013

**Date of the defence** 14 January 2014

**Permission to publish granted (date)** 17 December 2013

**Language** English

**Monograph**

**Article dissertation (summary + original articles)**

**Abstract**

Remote sensing offers a wide range of instruments suitable to meet the growing need for consistent, timely and cost-effective monitoring of land cover and forested areas. One of the most important instruments is synthetic aperture radar (SAR) technology, where transfer of advanced SAR imaging techniques from mostly experimental small test-area studies to satellites enables improvements in remote assessment of land cover on a global scale. Globally, forests are very suitable for remote sensing applications due to their large dimensions and relatively poor accessibility in distant areas.

In this thesis, several methods were developed utilizing Earth observation data collected using such advanced SAR techniques, as well as their application potential was assessed. The focus was on use of SAR polarimetry and SAR interferometry to improve performance and robustness in assessment of land cover and forest properties in the boreal zone. Particular advances were achieved in land cover classification and estimating several key forest variables, such as forest stem volume and forest tree height.

Important results reported in this thesis include: improved polarimetric SAR model-based decomposition approach suitable for use in boreal forest at L-band; development and demonstration of normalization method for fully polarimetric SAR mosaics, resulting in improved classification performance and suitable for wide-area mapping purposes; establishing new inversion procedure for robust forest stem volume retrieval from SAR data; developing semi-empirical method and demonstrating potential for soil type separation (mineral soil, peatland) under forested areas with L-band polarimetric SAR; developing and demonstrating methodology for simultaneous retrieval of forest tree height and radiowave attenuation in forest layer from interferometric SAR data, resulting in improved accuracy and more stable estimation of forest tree height.

**Keywords** Synthetic Aperture Radar, SAR polarimetry, SAR interferometry, scattering model, land cover, boreal forest, tree height, forest stem volume

**ISBN (printed)** 978-952-60-5522-0

**ISBN (pdf)** 978-952-60-5523-7

**ISSN-L** 1799-4934

**ISSN (printed)** 1799-4934

**ISSN (pdf)** 1799-4942

**Location of publisher** Helsinki

**Location of printing** Helsinki

**Year** 2014

**Pages** 166

**urn** <http://urn.fi/URN:ISBN:978-952-60-5523-7>



## Preface

These pages, so conveniently located at the beginning of this book and, as it is always the case, written at the very end of a fascinating journey called “writing a doctoral dissertation”, appear to be not the easiest ones to write, though probably one of the most pleasant ones to share. It was during the work on this thesis that I’ve opened a whole new world of new countries, people and activities around me, and at times it seemed hard to judge what the goal of this journey was and what just served as a background.

Research described in this thesis became possible and was primarily performed at VTT Technical Research Centre of Finland, under the guidance of my VTT supervisors Yrjö Rauste and Tuomas Häme. They have invited me to work in this northern country, the one that first seemed so distant and unknown, but suddenly became so familiar and close. They introduced me to and enriched my experience not only with fascinating world of “imaging radar for forest resource mapping,” but rather formed a solid picture of Earth Observation needs, practices, development trends and potential application areas, as well as offered opportunity to work on many interesting projects with different kinds of remote sensing data. Though independent research work is something deeply nested in Finnish scientific lifestyle, and serves as a good school for a young researcher, it is not easy to recall any day when either Yrjö or Tuomas were in the office and we didn’t end up discussing and working on something, a really impressive example of cooperation and friendly atmosphere within a research team. Tuomas was taking care to introduce me to Finnish culture and traditions, and I really appreciate time with him and his family. Eija Parmes is gratefully acknowledged for being a helpful and friendly office-mate during last four years. Other VTT colleagues from the broader Remote Sensing team are kindly acknowledged for their friendly attitude, close cooperation and enjoyable time together.

Completing this work would not be possible without kind help and guidance of my Aalto University supervisors Jaan Praks and Martti Hallikainen. Welcoming attitude and desire to help with everyday study issues and peculiarities of SAR polarimetry and SAR interferometry, accompanied by fruitful and friendly discussions not only limited to research activities, allowed myself to feel at home not only when being at VTT, but also at Aalto University Department of Radio Science and Engineering premises.

For financial support I am grateful to VTT Graduate School, that allowed me to concentrate on basic research and doctoral studies. Finnish Academy of Science and Letters is acknowledged for funding my research exchange to Friedrich Schiller University of Jena. Several projects whose outcome has partly contributed to this thesis were funded by European Commission, European Space Agency, Academy of Finland and Tekes – the Finnish Funding Agency for Technology and Innovation.

There are never too many friends, and their presence helps a lot in life and work. There are also the closest and beloved ones, and many sincere thanks go to them for sharing their friendship, time and activities with me. Last but not least, my sincere gratitude to my mother who always supported me.

Espoo, December 2013  
Oleg Antropov

## List of publications and author's contribution summary

This thesis consists of an overview and of the following publications which are referred to in the text by their Roman numerals.

- I Oleg Antropov, Yrjö Rauste, Tuomas Häme, "Volume scattering modeling in PolSAR decompositions: Study of ALOS PALSAR data over boreal forest," *IEEE Transactions on Geoscience and Remote Sensing*, vol. 49, no. 10, part 2, pp. 3838–3848, Oct. 2011.
- II Oleg Antropov, Yrjö Rauste, Anne Lönnqvist, Tuomas Häme, "PolSAR mosaic normalization for improved land-cover mapping," *IEEE Geoscience and Remote Sensing Letters*, vol. 9, no. 6, pp. 1074–1078, Nov. 2012.
- III Oleg Antropov, Yrjö Rauste, Heikki Ahola, Tuomas Häme, "Stand-level stem volume of boreal forests from spaceborne SAR imagery at L-band," *IEEE Journal of Selected Topics in Applied Earth Observations and Remote Sensing*, vol. 6, no. 1, pp. 35–44, Feb. 2013.
- IV Oleg Antropov, Yrjö Rauste, Heikki Astola, Jaan Praks, Tuomas Häme, Martti Hallikainen, "Land cover and soil type mapping from spaceborne PolSAR data at L-band with probabilistic neural network," *IEEE Transactions on Geoscience and Remote Sensing*, in press.
- V Jaan Praks, Oleg Antropov, Martti Hallikainen, "LIDAR-aided SAR interferometry studies in boreal forest: Scattering phase center and extinction coefficient at X- and L-band," *IEEE Transactions on Geoscience and Remote Sensing*, vol. 50, no. 10, pp. 3831–3843, Oct. 2012.

In Paper I, Paper II, Paper III and Paper IV original ideas, theoretical method development, literature overview, processing of experimental SAR data and further analysis of results obtained were responsibility of the author of this thesis. In all those papers Yrjö Rauste was also involved in planning of experiments and initial preprocessing of spaceborne SAR data, and also he and Tuomas Häme were involved in interpretation of the results obtained. Other co-authors contributed primarily in discussions related to the subject of the papers.

In Paper V, which was a collaborative effort, the work was performed primarily by Jaan Praks and the author. The author's role was in analysis of literature, cross testing and implementing the modeling approach, contributing to interpretation of the results obtained and helping with writing the paper. Initial preprocessing of airborne SAR data was done externally by DLR.

# Contents

<b>Preface</b> .....	<b>5</b>
<b>List of publications and author’s contribution summary</b> .....	<b>7</b>
<b>List of acronyms</b> .....	<b>10</b>
<b>List of symbols</b> .....	<b>12</b>
<b>List of figures</b> .....	<b>15</b>
<b>List of tables</b> .....	<b>17</b>
<b>1. Introduction</b> .....	<b>18</b>
1.1 Motivation.....	19
1.2 Advanced SAR techniques in spaceborne applications .....	20
1.2.1 Key concepts.....	21
1.2.2 Current status of advanced SAR techniques in spaceborne applications .....	23
1.3 State of the art in land cover and forest mapping based on SAR polarimetry and SAR interferometry.....	24
1.3.1 Land cover mapping .....	24
1.3.2 Mapping forest variables .....	27
<b>2. Materials and methods</b> .....	<b>30</b>
2.1 Study sites, SAR and in situ data .....	30
2.2 Methods.....	33
2.2.1 Land cover mapping with PolSAR data .....	33
2.2.1.1 Entropy-alpha-anisotropy analysis .....	34
2.2.1.2 Wishart classification.....	34
2.2.1.3 Probabilistic Neural Network.....	34
2.2.1.4 PolSAR model-based decomposition .....	36
2.2.1.5 Retrieval of soil type under vegetation.....	40
2.2.1.6 PolSAR mosaic normalization.....	41
2.2.2 Forest parameter retrieval with multi-parametric and interferometric SAR.....	43

2.2.2.1	Forest stem volume estimation with multitemporal SAR	43
2.2.2.2	Forest parameter retrieval using SAR interferometry	47
<b>3.</b>	<b>Results and discussion</b>	<b>52</b>
3.1	Generalized volume scattering model in PolSAR decompositions	52
3.1.1	Qualitative comparison	52
3.1.2	Eigenvalue non-negativity constraint for the remainder covariance matrix	55
3.2	Land cover and soil type mapping using PolSAR data	57
3.2.1	Relative performance of the maximum likelihood and PNN-based classification	58
3.2.2	Temporal variability of the classification performance	59
3.2.3	Inferring soil type properties	61
3.2.4	Comparison of the polarimetric feature sets	61
3.2.5	PolSAR suitability for wide-area land cover mapping	62
3.3	Implication of PolSAR mosaic normalization on thematic mapping	62
3.4	Robust SAR-based forest stem volume retrieval	66
3.4.1	General model fitting performance	66
3.4.2	Comparison with other stem volume retrieval approaches	70
3.5	Improved forest parameter retrieval using SAR interferometry	71
3.5.1	X-band InSAR data processing	71
3.5.2	L-band InSAR data processing	74
<b>4.</b>	<b>Conclusions</b>	<b>77</b>
<b>5.</b>	<b>Future research</b>	<b>79</b>
	<b>References</b>	<b>80</b>
	<b>Errata</b>	<b>98</b>
	<b>Appendices</b>	
	Papers I–V	

## List of acronyms

ALOS	Advanced Land Observing Satellite
CHM	Canopy Height Model
CLC2006	CORINE Land Cover 2006
DEM	Digital Elevation Model
DLR	German Aerospace Center
EO	Earth Observation
ESA	European Space Agency
E-SAR	Airborne SAR system of DLR
GCP	Ground Control Point
GVSM	Generalized Volume Scattering Model
JAXA	Japanese Aerospace Exploration Agency
JERS	Japanese Earth Resources Satellite
InSAR	SAR Interferometry
LIDAR	Light Detection And Ranging
ML	Maximum Likelihood
PALSAR	Phased Array type L-band Synthetic Aperture Radar
pdf	probability density function
PoI-InSAR	Polarimetric SAR Interferometry
PoSAR	SAR polarimetry
PNN	Probabilistic Neural Network
RADAR	Radio Detection And Ranging
RGB	Red Green Blue
RMSE	Root Mean Square Error
RV	Random Volume

RVoG	Random Volume over Ground
SAR	Synthetic Aperture Radar
SM	Scattering Mechanism
SPC	Scattering Phase Center
TanDEM-X	TerraSAR-X add-on for Digital Elevation Measurement
TP	Total backscattered Power

## List of symbols

$\alpha$	average alpha angle
$\beta$	empirical coefficient in backscatter models
$\gamma$	interferometric complex coherence
$\gamma_V$	interferometric coherence volume decorrelation
$\gamma_B$	interferometric coherence baseline decorrelation
$\gamma_{SNR}$	interferometric coherence noise decorrelation
$\varepsilon$	logarithmic HH-VV ratio
$\phi_0$	ground phase
$\phi_f$	DEM-to-phase fitting constant
$\phi_\gamma$	interferometric phase
$\eta$	HH-VV (co-polarization) ratio
$\kappa$	wavenumber
$\kappa_z$	vertical wavenumber
$\lambda$	wavelength
$\theta$	incidence angle
$\mathcal{G}$	scattering model complex coefficient
$\rho$	HH-VV correlation coefficient
$\sigma^0$	radar scattering coefficient (sigma nought)

$\sigma_{i,meas}^0$	measured and modeled scattering coefficient from $i$ -th forest stand
$\sigma_{i,model}^0$	
$\sigma_{gr}^0$	ground backscatter parameter in models
$\sigma_{veg}^0$	vegetation backscatter parameter in models
$\sigma_{pq}$	radar cross section
$\sigma_m$	local extinction coefficient of volume
$\sigma_v$	extinction coefficient of volume
$\zeta$	scattering model complex coefficient
$\vec{\omega}$	polarization vector
$A$	anisotropy
$C_1, C_2, C_3$	coefficients in forest backscatter models
$\mathbf{C}$	covariance matrix
$E_p^i, E_q^i$	components of incident electric field
$E_p^s, E_q^s$	components of scattered electric field
$e$	HV-HH (cross-polarization) ratio
$f_s, f_d, f_v$	coefficients in scattering decomposition models
$G$	decision rule parameter
$H$	target entropy
$h_{DEM}$	terrain elevation
$h_f$	constant for DEM fitting
$h_v$	forest volume layer height
$\mathbf{k}, \mathbf{k}_P$	target vector in lexicographic and Pauli basis formats
$L_i$	regression parameters in models

$M$	ground-to-volume scattering ratio
$m_g$	ground contribution parameter
$P_s, P_d, P_v$	powers of scattering mechanisms
$P_{total}$	total power
$p$	polarization, when in subscript
$p_i$	pixel value
$q$	polarization, when in subscript
$R_{rl}$	normalization ratio
$r$	distance
$S_{pq}$	scattering matrix element for $p$ receive and $q$ transmit polarizations
<b>S</b>	scattering matrix
$V$	stem volume

## List of figures

<b>Figure 2.1.</b> Location of study sites in Finland. ....	30
<b>Figure 2.2.</b> Typical structure of probabilistic neural network (Paper IV). ....	35
<b>Figure 2.3.</b> Processing chain for soil type retrieval under forest vegetation (Paper IV). ....	41
<b>Figure 2.4.</b> Flowchart of the forest stem volume retrieval approach (Paper III). ....	46
<b>Figure 2.5.</b> The proposed forest tree height retrieval algorithm (Paper V). ....	51
<b>Figure 3.1.</b> Color coded representations of decomposed PolSAR image (45 x17.5 km <sup>2</sup> ) over Kuortane acquired in May 2007 using the Freeman-Durden (left) and GVSM (right) approaches; double-bounce scattering contribution depicted in red color, volume in green, and surface in blue (Paper I). ....	54
<b>Figure 3.2.</b> Histogram of HH-VV ratio as a function of $\epsilon$ for the averaged PolSAR image, averaging window size: 3x3, 5x5, 11x11 (Paper I). ....	55
<b>Figure 3.3.</b> Classification maps from PolSAR data acquired over Kuortane, with the highest total accuracies (Paper IV). ....	60
<b>Figure 3.4.</b> Land cover mapping from fully polarimetric SAR mosaic produced from ALOS PALSAR data acquired over Saariselkä (Paper II). ....	64

<b>Figure 3.5.</b> Model fitting performance for SAR image acquired over Kuortane on 27.06.2007, HH-polarization (Paper III). .....	67
<b>Figure 3.6.</b> Scatterplots illustrating agreement between predicted and measured stem volume using validation sets for both study sites, multiple regression (2.19) with HH polarization SAR data used (Paper III). .....	68
<b>Figure 3.7.</b> Relationship between interferometric SPC and LIDAR-measured tree height at X-band, VV-polarization InSAR data, Kirkkonummi (Paper V). .....	72
<b>Figure 3.8.</b> Random volume model inversion results for areas with negligible ground contribution at X-band, VV-polarization InSAR data, Kirkkonummi (Paper V).....	73
<b>Figure 3.9.</b> Relationship between retrieved tree height and LIDAR-measured tree height at X-band for areas with negligible ground contribution, VV-polarization InSAR data, Kirkkonummi (Paper V). .....	73
<b>Figure 3.10.</b> Relationship between interferometric SPC and LIDAR-measured tree height at L-band, HH and HH-VV polarizations used, Kirkkonummi (Paper V). .....	75
<b>Figure 3.11.</b> Random volume model inversion results for areas with negligible ground contribution at L-band, HV-polarization used, Kirkkonummi (Paper V).....	75
<b>Figure 3.12.</b> Relationship between retrieved tree height and LIDAR-measured tree height at L-band (HV-pol) for areas with negligible ground contribution (Paper V).....	76

## List of tables

<b>Table 2.1.</b> Dual-polarization SAR data for stem volume mapping in Kuortane and Heinävesi (Paper III). .....	33
<b>Table 3.1.</b> Percentage of pixels with non-negative PolSAR covariance matrix eigenvalues for the Kuortane study site (Paper I). .....	55
<b>Table 3.2.</b> Classification summary for different combinations of polarimetric features for PolSAR imagery acquired over the Kuortane study site (Paper IV). .....	58
<b>Table 3.3.</b> Results of PolSAR mosaic based land cover classification of the Saariselkä study site, with the overall accuracy estimates given both for multi-class and forest-nonforest (in brackets) classification (Paper II). .....	65
<b>Table 3.4.</b> Stem volume estimation from dual-pol ALOS PALSAR data acquired over the Kuortane and Heinävesi study sites (Paper III) . .....	69

# 1. Introduction

Recently, the popularity of imaging radar in Earth Observation (EO) has grown, and advanced from the level of mostly experimental, scientific or military usage towards implementation of near-operational services. It was shown to be useful in assessment of properties and continuous monitoring of land cover, forests, snow, crops, ship detection, and hazard assistance, to name a few. Advanced Synthetic Aperture Radar (SAR) techniques, previously available only on airborne platforms, start to be implemented on newly launched satellites, bringing new dimensionality to SAR data to be processed and making it potentially possible to perform multi-polarization, multifrequency, and multitemporal acquisitions in a timely and systematic manner over global areas. A new generation of satellite SAR sensors, starting from ALOS PALSAR, Radarsat-2, CosmoSkyMed constellation, TerraSAR-X/TanDEM-X to forthcoming and planned missions (e.g., ESA Sentinels, ESA BIOMASS, Radarsat Constellation) enable application of fully polarimetric, interferometric and, potentially, polarimetric interferometric SAR techniques and SAR tomography from orbit. It is the possibility of global assessment of large territories with frequent repetition capability that makes spaceborne applications of SAR data very attractive and cost-effective. It is the possibility of SAR data acquisition under practically any environmental, seasonal and weather conditions, as well as independence of daylight, that promotes usefulness and utility of SAR technology compared to, e.g., use of optical spaceborne data.

There is, however, a price to pay for all these benefits mentioned, and among the particularly challenging aspects in SAR image processing, aside from the basic hardware-related signal processing, is the need for initial preprocessing of acquired SAR imagery including elimination of artifacts. It is also the general difficulty of interpretation of preprocessed SAR imagery that requires the attention of the scientific community and remote sensing experts to develop new, more effective image processing techniques. In the case of SAR imaging, the target response (backscattered signal) is primarily determined by geometrical and electrophysical (mostly moisture-related) properties of the target, which are expected to be linked to descriptors of ecological classes or other phenomena of interest.

Visual interpretation of SAR images is a complicated task due to the often present mixture of different scattering mechanisms in a single resolution cell. In order to achieve quantitative analysis of target properties from radar scattering behavior,

the accurate and adequate modeling of backscattered signal is needed. The inherent limitations on the number of SAR observables that can be collected, or the dimensionality of the inversion problem, is a confounding factor. After appropriate backscattering model is available, computer-based classification methods, both supervised and unsupervised, can be used on pixels (resolution cells) or groups of pixels, to perform SAR based mapping. Another option is to use the underlying model in inversion scenario in order to directly retrieve parameters of interest.

In this thesis, the problem of optimal modeling of backscatter from forest canopies, as well as assessment of underlying land cover properties in general, together with application aspects in real test site scenarios, is addressed. The treatment is based on the assumption that measured SAR signals are generally multi-polarized. Special emphasis is put on wide area mapping, with focus on near-operational use of techniques developed for the needs of the forestry sector, government agencies and other interested parties.

The thesis is organized as follows. Further in this chapter motivation for the development of improved methods in land cover and forest monitoring is given. Then several relevant basic concepts in polarimetric and interferometric SAR imaging are briefly introduced, followed by an overview of the current state-of-the-art in the topic and analysis of some problems that will be treated in the thesis. In Chapter 2, materials and methods are described, while Chapter 3 concentrates on analysis and discussion of the results obtained. Finally, conclusions on the work performed in the framework of the thesis are drawn, and recommendations for future research are given.

## 1.1 Motivation

One of the main drivers for the need of consistent monitoring of forests and land cover in general is due to present uncertainties in climate predictions determined by feedback between climate and changes in land surface processes. Northern high latitudes are particularly important because of the vast store of carbon in northern forests and peatlands. Certain key processes, notably land cover change, vegetation activity and seasonality, biomass change, cryospheric dynamics, soil freeze-thaw periods, fire activity and soil moisture can all be recovered from satellites. Globally, forests are very suitable for remote sensing applications due to their large dimensions and relatively poor accessibility in remote areas. The boreal forest, with an area of 11.35 Mkm<sup>2</sup>, is the largest terrestrial biome, and stores about 32% of the world's forest carbon stock [1]. Europe contains 25% of the world's boreal forests, while more than 70% of Finnish territory is covered by forest, making it of a major interest for forest sector, government agencies and society. Thus, the demand comes from the need for adequate modeling of the interaction between forests and the atmosphere [2], [3], general monitoring of on-going climate changes [4] as indicated by processes of deforestation, forest degradation and afforestation, as well as for supporting daily and seasonal forest management activities.

Imaging radar is especially suitable for land cover monitoring in primarily forested areas. Though it may be less sensitive to forest species than optical data, it can provide the so-called “volume” component, especially when using SAR polarimetry and SAR interferometry. One of the key challenges in the boreal forest zone is frequent cloud cover during most of the year, which hinders the use of optical sensors. Use of optical sensors is further complicated in winter because atmospheric correction becomes more difficult and less reliable with decreasing sun elevation angle. In addition to fully opaque clouds, other atmospheric artifacts, such as smoke, aerosol contamination, and various forms of cloud shadow effects affect the quality and usability of optical data. In contrast, radar data can be obtained on every orbit of the satellite regardless of the weather conditions, which makes it ideal for applications requiring long, regular time-series of data with a constant time separation between observations.

SAR polarimetry and interferometry are powerful yet emerging techniques potentially capable of strongly improving EO capability. However, the current level of maturity does not allow operational use of spaceborne SAR data. For example, in the forestry sector, accuracies in estimating such crucial forest parameters as tree height or stem volume from imaging radar data are still significantly lower than in conventional forest inventories or airborne LIDAR surveys. Thus, more effort is needed in this direction, and research work described in this thesis aims at developing new and improving existing methods and applications that effectively utilize advanced SAR techniques, thus contributing to advance them to the higher technology readiness levels.

### **1.2 Advanced SAR techniques in spaceborne applications**

Radar (radio detection and ranging) technology is based on emitting a microwave signal followed by measuring scattered signal. SAR is an imaging radar system which uses coherent microwave signals to illuminate a target, or an area, to focus the signal and form an image of a scene using the forward motion of sensor platform. Advanced SAR techniques that are in this thesis utilize the full vector nature of electromagnetic waves, and primarily rely on use of different combinations of polarizations for transmitting and receiving antennas (in SAR polarimetry), as well as coherent combination of two backscattered signals acquired under slightly different incident angles (in SAR interferometry).

Basic principles of SAR image formation and preprocessing, as well as understanding polarimetry, polarimetric synthesis and basics of interferometric processing are outside the focus of this thesis and are omitted here. Relevant information is broadly covered in several books and review articles, e.g. [5]-[11], as well as tutorials available online [12], [13].

In what follows, several key concepts in SAR polarimetry and interferometry that are later referred to at the thesis are listed, followed by brief overview of the current status of implementing these advanced SAR techniques on satellites.

### 1.2.1 Key concepts

Polarization is a fundamental property of electromagnetic waves, and, as such, it is defined by orientations of the electric and magnetic field vectors. While polarization is not strictly important in terms of radio wave propagation in free space, the initial polarization of electromagnetic wave affects the response of illuminated target, and is often changed in the scattered wave compared to incident wave. In this context, radar polarimetry is a technique that allows describing the properties of the target via the change of polarization state of electromagnetic waves.

In fully polarimetric radar systems, transmitted and received wave polarization states are identified by measuring coherently four polarization combinations in orthogonal pairs. Then, in the plane wave approximation, assuming propagation in free-space, the general dependence of backscattered wave upon incident wave as observed from radar, in the monostatic backscattering case, at a single wavelength  $\lambda$ , can be described [5] as

$$\begin{bmatrix} E_p^s \\ E_q^s \end{bmatrix} = \frac{\exp(jkr)}{r} \begin{bmatrix} S_{pp} & S_{pq} \\ S_{qp} & S_{qq} \end{bmatrix} \begin{bmatrix} E_p^i \\ E_q^i \end{bmatrix}. \quad (1.1)$$

Here,  $S_{pq}$  is complex reflectivity, associated with pair  $(p, q)$  of orthogonal, but otherwise general polarizations;  $k = 2\pi / \lambda$  denotes wavenumber; and  $r$  is a distance to the observation point. The incident and scattered electric fields are represented by their complex components  $(E_p^i, E_q^i)$  and  $(E_p^s, E_q^s)$ . Then, e.g., scattering matrix components  $S_{pp}$  and  $S_{pq}$  describe the  $p$ -polarized scattering response of the target due to  $p$ - and  $q$ -polarized incident fields.

Radar cross section is defined [5] as

$$\sigma_{pq} = 4\pi |S_{pq}|^2. \quad (1.2)$$

The whole 2x2 matrix on the right-hand side of (1.1) is called the polarization scattering matrix. The scattering matrix is the fundamental measured entity in SAR polarimetry, and often linear vertical and horizontal transmit and receive polarizations are used:

$$\mathbf{S} = \begin{bmatrix} S_{hh} & S_{hv} \\ S_{vh} & S_{vv} \end{bmatrix}. \quad (1.3)$$

$S$  is, mathematically, a linear operator, representing transformation from the incident to backscattered wave upon interaction with the target. It can be expanded into the target vector, represented in lexicographic format as

$$\mathbf{k} = [S_{hh} \quad S_{hv} \quad S_{vh} \quad S_{vv}]^T, \quad (1.4)$$

that under the reciprocity condition ( $S_{hv} = S_{vh}$ ) transforms to

$$\mathbf{k} = [S_{hh} \quad \sqrt{2}S_{hv} \quad S_{vv}]^T. \quad (1.5)$$

Alternative representation of the target vector in the Pauli basis format [24] is given by:

$$\mathbf{k}_P = [S_{hh} + S_{vv} \quad S_{hh} - S_{vv} \quad S_{hv} + S_{vh} \quad j(S_{hv} - S_{vh})]^T. \quad (1.6)$$

and, assuming reciprocity,

$$\mathbf{k}_P = 1/\sqrt{2}[S_{hh} + S_{vv} \quad S_{hh} - S_{vv} \quad 2S_{hv}]^T. \quad (1.7)$$

The above target vector is suitable for description of isolated, discrete point scatterers. If the target is distributed, second-order statistics of backscattered field, fully describing polarimetric information content for complex and natural distributed targets, is usually employed. It is obtained as ensemble averaged Kronecker product of the target vector. The corresponding covariance matrix (or coherency matrix, if Pauli basis target vector used) is positive semi-definite Hermitian. For example, under reciprocity condition, the following expression for covariance matrix is obtained:

$$\mathbf{C} = \begin{bmatrix} \langle S_{hh} S_{hh}^* \rangle & \langle \sqrt{2} S_{hh} S_{hv}^* \rangle & \langle S_{hh} S_{vv}^* \rangle \\ \langle \sqrt{2} S_{hv} S_{hh}^* \rangle & \langle 2 S_{hv} S_{hv}^* \rangle & \langle \sqrt{2} S_{hv} S_{vv}^* \rangle \\ \langle S_{vv} S_{hh}^* \rangle & \langle \sqrt{2} S_{vv} S_{hv}^* \rangle & \langle S_{vv} S_{vv}^* \rangle \end{bmatrix}. \quad (1.8)$$

SAR interferometry is based on analysis of phase difference between two SAR measurements (or scenes) acquired under slightly different incidence angles. Cross track interferometry can be achieved either by placing two antennas separated by cross-track baseline on the same platform, or organizing separate repeat passes of a single SAR instrument.

Interferometric coherence, or degree of correlation between two complex SAR measurements, is given by

$$\gamma = \frac{\langle p_1 p_2^* \rangle}{\sqrt{\langle |p_1|^2 \rangle \langle |p_2^*|^2 \rangle}}, \quad (1.9)$$

where  $p_1$  and  $p_2$  denote complex reflectivity of resolution elements in SAR scenes. The full power of this technique is available when SAR measurements are fully polarimetric, and called polarimetric SAR interferometry (Pol-InSAR). Both amplitude of interferometric coherence (or degree of interferometric decorrelation) and interferometric phase are useful for interpretation. Interferometric coherence can be expressed as a set of components contributing differently to the overall decorrelation:

$$\gamma = \gamma_B \cdot \gamma_{SNR} \cdot \gamma_V, \quad (1.10)$$

where  $\gamma_B$  represents baseline (spatial and temporal) decorrelation,  $\gamma_{SNR}$  – decorrelation caused by system noise, and  $\gamma_V$  – decorrelation caused by the “volume” component. The latter provides sensitivity to the vertical dimension of the underlying scatterers, e.g., vertical forest structure, and is of particular interest in this thesis.

### 1.2.2 Current status of advanced SAR techniques in spaceborne applications

Spaceborne imaging radars have been employed for studies on land cover mapping, as well as assessment of properties of forested areas for quite a long time, starting from Seasat mission in 1978. However, the general limiting factor on the way to operational use of spaceborne SAR technology for retrieval of useful information about the environment is lack of SAR observables, or the lack of unique relationships between scattering models and these observables. Thus, the general trend in land cover and forest mapping with SAR instruments is toward the use of multi-parameter SAR data, including multi-polarimetric, interferometric, multi-source, multi-frequency and multitemporal SAR data [11], [14]. While airborne experiments with SAR data are mostly intended for experimental verification of novel techniques and small test-area studies, spaceborne SAR data offers possibility to cover large areas in a systematical and timely manner, and looks a promising candidate for enabling new environmental and security services. Advanced SAR techniques, such as PolSAR, InSAR and Pol-InSAR data with an increased

number of observed variables offer improved possibilities in all respects, and specific use of spaceborne PolSAR data for wide area land cover/use mapping in this thesis seems to be pioneering, as compared to numerous studies with airborne or spaceborne PolSAR data on small test sites.

Currently, not all SAR techniques available by airborne observation are implemented on orbit. Moreover, those that are even implemented are often quite far from maturity, and lots of additional development is needed. With the launch of new generation of spaceborne SAR instruments and constellations, the situation is improving; however, improvements in processing of single-acquisition PolSAR imagery are still of significant benefit when multitemporal acquisitions of spaceborne PolSAR data over wide areas are not possible.

In the framework of land cover and forest mapping in the boreal forest zone, the opportunity to use multi-polarization (including quad-polarimetric) and multitemporal SAR data at L-band was offered by a Phased Array type L-band Synthetic Aperture Radar (PALSAR) sensor on-board ALOS during its life span of more than 5 years [15]. This satellite is expected to be followed by its more advanced successor in the near future [16]. However, due to relatively long repetition period of ALOS-1, possibility of using interferometric SAR acquisitions in a systematic manner was limited due to high temporal decorrelation. The first opportunity to take advantage of spaceborne multi-polarization single-pass interferometer is offered by the TanDEM-X mission [17].

### **1.3 State of the art in land cover and forest mapping based on SAR polarimetry and SAR interferometry**

In further subsections of this section, the mapping of forest cover and land cover/use mapping are treated separately. This was done despite the fact that in the simplest case the forest/non-forest classification can be considered a specific case of more general land cover classification. On the other hand, forest parameters are usually continuous variables as opposed to discrete land cover classes, even though specific number of classes might be unknown. Also, there are quite a few forest variables for assessment, e.g. forest stem volume or above ground biomass, tree height, forest species, fraction of forest cover, etc. In this way, mapping forest cover represents a separate study subject and cannot be considered a simple case of land cover classification.

#### **1.3.1 Land cover mapping**

Segmentation and classification of PolSAR data has been a popular research topic and addressed in quite a few studies, with imagery acquired by both airborne and spaceborne SAR instruments, and using empirical, statistical and physics-based approaches. The common assumption about PolSAR data exhibiting circular Gaussian probability density function (pdf) has led to development of a supervised classification approach, which uses second order statistics of PolSAR data

modeled by multilook Wishart distribution [18]. This approach appeared to be fruitful and was implemented in a number of supervised and unsupervised classification methods, e.g. [19]. It is generally applicable for any PolSAR data; however, it is deemed to be more suitable for data acquired over natural terrain. Further developments take advantage of more complicated statistical models for the description of PolSAR imagery [20], [21], [22], with inclusion of textural information, relaxing the Gaussianity assumption and, e.g., adopting the K-Wishart distribution [23] of polarimetric coherency matrix instead.

On the other hand, there is a variety of well-established incoherent target decomposition techniques for PolSAR imagery, with broad overviews given in [11], [24]. Incoherent target decomposition techniques are mostly based either on analysis of eigenvalues of the PolSAR coherency matrix [24], [25], or employ specific physical models of scattering mechanisms for representation of the PolSAR covariance matrix as the weighted sum of these more simple contributions [26], [27]. The first approach is primarily of mathematical nature and seems to be intended exclusively for classification purposes [28], while the second approach has potential for physics model-based inversion. Its benefit is in the possibility of direct physical interpretation of PolSAR data, as well as in simplicity of image processing algorithm for implementation. Once contributions of different scattering mechanisms are estimated, more advanced polarimetric models can be used for further geophysical parameters analysis or inversion in various applications [29], [30], [31], [32].

In general, the applicability of any given decomposition varies considerably, and suitability of each chosen method for PolSAR data analysis might be determined on the basis of previous experience in similar conditions [29], [30], [31], [32], [33].

The widely known difficulty in decomposing polarimetric data for further analysis and interpretation is that environmental and image acquisition conditions cannot be controlled in general, and there is a growing need for either more universal models or, at least, some adjustment of model parameters for each particular site. The unambiguous inversion of forward models is also difficult because of the lack of polarimetric observables when compared to the quantity of parameters in forward modeling. Thus it is even more appreciated, if such model adjustment can be done using only PolSAR data as such, without any reference to *in situ* data [27], [31], [34], allowing for a more flexible choice of parameters describing different scattering contributions, primarily volume scattering. Another important issue is to avoid non-physical solutions sometimes appearing in the process of decomposition, which has drawn increased interest lately, such as non-negativity of eigenvalues of covariance matrices at each decomposition step [35], [36], [37], [38], [39].

Incoherent decompositions can be combined with statistical classifiers to produce more robust results [40], [41]. One of the possible ways to exploit PolSAR decompositions is to use their components as the so-called polarimetric features. Then, it is possible to take advantage of all the existing classification techniques originally developed for intensity data, applying them in a straightforward manner on these features. Other polarimetric descriptors include Touzi parameters [42],

backscattering coefficients, co-polarization and depolarization ratios, and various phase differences [43]. However, one of the common problems with these features is the generally high correlation between them. Thus, selection of a relatively small subset of polarimetric features might be enough for practical application. Studies [44], [45] aimed to assess relative performance of several popular polarimetric features in the benchmarking comparison using back-propagation neural network, however, resulted in no clear identification of the most fruitful combination. One can apply statistical feature selection [43], machine learning strategies, e.g. [46], [47], or resort to direct physics-based reasoning [40], [48], in order to form a respective set of features useful for some particular application. Yet another possible choice is to use all of the available features in the framework of linear (principal component analysis) or nonlinear (see, e.g. [49]) dimensionality reduction. The drawback here is the exponential increase in the number of parameters, and difficulty in interpretation of the obtained results. It is particularly problematic to assign any actual physical behavior to artificially generated feature vector.

Most experiments with PolSAR classification at L-band aimed at land cover assessment and performed comparisons against reference ground data, optical spaceborne imagery or value added products [50], [51]. However, notable gaps identified in the literature include the scarcity of attempts of soil type assessment (peatland, mineral soil) under non-inundated conditions, in particular under high forest vegetation, from single-acquisition space borne SAR imagery at L-band [52]. This problem is strongly coupled with soil moisture retrieval, and can benefit from the use of relevant techniques.

When performing classification, polarimetric features are usually assigned some beforehand known statistical behavior, usually Gaussian pdf. It is important to see if any improvement in classification performance can be gained if this assumption for features is relaxed, analogously to PolSAR data itself [53]. While it may not be always possible to establish a link between pdfs of original PolSAR data and pdfs of derived polarimetric features [53], a feasible way to assess probabilistic characteristics of the features is to resort to non-parametric estimation of their pdfs. This can be achieved, provided the PDFs are smooth, using, e.g., probabilistic neural network (PNN) technique [54], [55], so far demonstrated in few remote-sensing applications [56], [57], [58]. Quick training, relative stability to data outliers and absence of any prior assumptions about probabilistic distribution of the data are among its advantages, to mention a few. Also, a PNN model can exhibit a reasonable computational and memory efficiency if the number of training samples is limited to moderate values [54].

Keeping in mind the need for operational monitoring of wide areas, the ability to combine separate PolSAR scenes into homogeneous mosaics, analogically to single-polarization and dual-polarization SAR data [59], [60], [61], [62], would boost the applicability and effectiveness of PolSAR mapping techniques. It is of particular interest in situations when it appears hard to find adequate reference data for each individual PolSAR image. Generally, availability of PolSAR data, e.g., time intervals between acquisitions of neighboring scenes, as well as the sensitivity of PolSAR signatures to environmental factors limit production and

further use of such mosaics. Thus, it is important to see how multitemporal PolSAR data acquisitions influence mosaic classification accuracy and to identify techniques that are suitable for the processing of such multi-polarization data. Other important issues include identification of application areas where multi-date PolSAR mosaic can be effectively used, as well as pinpointing possible challenges and drawbacks of such mosaicing [63].

There were several studies indicating suitability of single-polarization InSAR data for simple land cover stratification or forest delineation, e.g. [64], [65], though generally it seems less applicable for land cover assessment due to smaller number of observables. The potential of InSAR data in spaceborne applications is better revealed when combining both polarimetric and interferometric capabilities of SAR, and is particularly useful in retrieving forest parameters, as discussed in next section.

### 1.3.2 Mapping forest variables

Key forest variables of interest that can be inferred via SAR based remote sensing are forest biomass or forest stem volume, forest tree height and, to a lesser extent, forest tree species. In the framework of this thesis we concentrate on the first two.

Numerous evaluations of SAR-instruments at different wavelengths have been performed over the past two decades, pursuing the goal of high-quality assessment of forest cover characteristics. These included relevant studies using data acquired by instruments onboard satellite and airborne platforms over boreal, temperate and tropical forests using both standard and advanced (experimental) SAR imaging modes, as well as combinations of several sensors [66]-[87],[30]. Due to higher penetration through forest canopy at a longer wavelength, L- and P-band SAR data are more suitable for the purpose of forest biomass or forest stem volume retrieval [88], [89], [90].

**Forest stem volume.** Previous experience with multi-polarization SAR at L-band over boreal forest was rather limited, as L-band spaceborne imaging radars before ALOS PALSAR [91]-[93] were operating in a single-polarization mode. Literature known from airborne SAR studies over selected test sites mostly indicates higher sensitivity to biomass of cross-polarized backscatter at L-band, though sometimes the difference can be very small, particularly in the boreal forest environment [89]. Also, a number of studies indicate the advantages of using multitemporal acquisitions for biomass (or stem volume) estimation when compared to a single-image-based approach, particularly over boreal forest [73], [76], [94]. In [95] some potential of ALOS PALSAR data for stand-wise stem volume retrieval in the boreal forest zone was indicated, noting multitemporal dependence of results. However, the problem is that approaches demonstrated so far with spaceborne SAR data at L-band give good results only when produced biomass estimates are aggregated to relatively large areas [94], or suffer from inversion artifacts [95], that may complicate routine stem volume estimation.

**Forest tree height** can be considered as an independent forest variable of interest, or it can be further used for assessing forest biomass provided the allometric equations are available for a given forest type [96]. Technically, the most direct way to measure tree height from space platform is via SAR interferometry. Naturally, L- and P-bands are most useful here as well. However, in less dense boreal forest areas information about tree height, as indicated by a number of previous studies, can be retrieved even with shorter wavelength radar, e.g. at X-band.

Model-based analysis of InSAR data for retrieval of forest parameters was the scope of many studies. Traditional coherent forward models proved useful for the description of forest canopies [97]-[102]. Their drawback was, however, in the requirement of many input parameters, which limits possibilities to invert forest variables due to the lack of interferometric SAR observables. The number of independent observations can be increased using multi-polarization, multi-frequency, multi-incidence-angle and multibaseline acquisitions [103], [104], as well as adding supplementary topography information. Another solution is to adopt simpler models for data interpretation, which are still capable to provide essential information about the canopy properties. Among these, the Random Volume over Ground (RVoG) model [105]-[110] introduced in polarimetric SAR interferometry (Pol-InSAR), has gained particular popularity. Under some assumptions, it can provide estimates of forest height, extinction, and ground-to-volume scattering ratio. The RVoG model was extensively studied and found to be suitable in different forest environments ranging from tropical rainforest [104], [109], [110] and temperate broad-leaved forests [111] to boreal forest [112], [113], [114], [115], mostly at X, C and L frequency bands, as well as at longer wavelengths [116], [117].

A particular difficulty with the RVoG model inversion is that it is not applicable for single-pol InSAR data, as the inversion problem becomes under-determined. However, results from the FINSAR campaign indicate that X-band single polarization interferometric coherence can be successfully used to retrieve forest height under certain conditions [115], [120]. The common simplifications of the RVoG model include the use of external ground DEM, fixing the forest extinction coefficient to a certain value [110], [115] and, at higher frequencies, even completely discarding the ground scattering contribution [110] due to high attenuation in the vegetation layer. One more step further compared to, e.g., forest parameter retrieval reported in [115], [118], [119] would be simultaneous estimation of the scattering phase center (SPC) height and extinction coefficient [120]. This scenario is of particular interest for retrieval of forest parameters using imaging capabilities of the TanDEM-X mission [121].

At X-band, the ground is usually not visible, and a simple model representing a single layer of randomly oriented volume (RV) can be inverted in order to estimate tree height using single-polarization InSAR data when the ground topography is known. A similar approach was envisaged in, e.g., [122], [123], [124]. Moreover, the inversion for extinction might be also possible in several cases where ground is not visible. Then, if information on extinction coefficient is available, it can be further used for improving the accuracy of tree height estimation. In [125], an advanced extinction coefficient model with fractal trees was used for more accurate

recovery of the tree heights, however requiring some additional reference information. Also, if extinction can be retrieved from InSAR data, an obvious benefit is the possibility of producing extinction coefficient look up tables for selected forest species, with respect to density and structure orientation. Following the idea mentioned in [126], such a look up table can be further used for more accurate height estimation via model-based inversion.

Another key application wavelength is L-band, primarily due to ALOS PALSAR, and keeping in mind that before implementation of the BIOMASS mission by ESA it is the most suitable wavelength for assessment of forest cover properties. At L-band, the ground is usually visible [115], [127], therefore the ground contribution cannot be neglected in a typical inversion scenario. Polarimetric diversity of the polarization-dependent ground response is usually further employed for extraction of the model's parameters from Pol-InSAR data. However, use of topographic phase available from an external ground DEM can still improve reliability and stability of the inversion process, as well as to provide means for estimating the mean extinction value for areas with very high and dense forest, where ground may not be visible [Paper V].

## 2. Materials and methods

Here we describe the study/test sites with available in-situ and reference data and SAR data used.

### 2.1 Study sites, SAR and in situ data

The focus is on mapping land cover and forest in the boreal forest zone. All study sites are located in Finland.

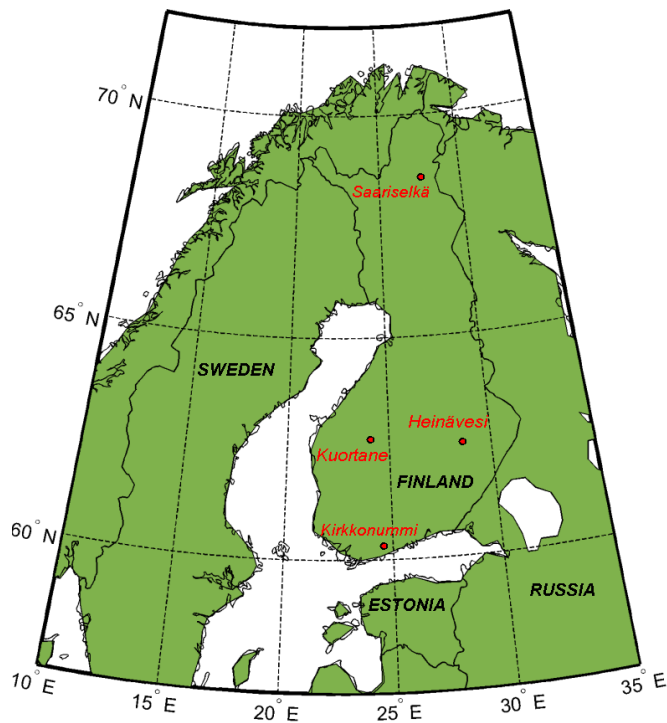


**Figure 2.1.** Location of study sites in Finland.

The **Kuortane** site (center coordinates: 62°49'N, 23°32'E) is located in western Finland, in the vicinity of lake Kuortane. This study site was used both for studies on land cover mapping (Paper I, Paper IV) and forest stem volume retrieval (Paper III). The Kuortane area represents typical Finnish, conifer-dominated mixed forestland. The area is covered by coniferous (managed pine-dominated) and mixed forest. In addition to Scots pine, Norway spruce and birch are common. The soil is mostly till, but the proportion of sandy soils and peat land is also high. In addition to forests and lakes, the municipality of Kuortane with surrounding agricultural areas is inside the study site. The area is flat to hilly. Terrain elevation varies between 80 and 130 m in the area of forest inventory ground data, and between 40 and 226 m in the whole Digital Elevation Model (DEM) used for ortho-rectification of the ALOS PALSAR data. The DEM from the Finnish National Land Survey at the Kuortane site covers an area of 50 km by 50 km. The DEM has a pixel spacing of 25 m and has a vertical accuracy of about 2.5 m.

PoSAR data used in land cover mapping were collected by the ALOS PALSAR sensor in November 2006, March 2007, and May 2007. During the November acquisition, some snow was already present on the ground, but the water surfaces were mostly open. The temperature was around 0 °C, with a snow fall at that time. In the March scene, the lakes were covered with ice and some water on top. The temperature was 6 °C and the day was clear. In the May scene, the temperature at the time of acquisition was 11 °C with light precipitation. Dual-pol SAR data acquired over the study site and used in forest stem volume mapping is summarized in Table 2.1.

Reference data for land-cover mapping study were primarily represented by Finnish CORINE Land Cover 2006 (CLC2006). It is a newer, updated and corrected version of the national land cover/use map of Finland [128], [129], [130]. The spatial resolution of the land cover data is 25 m. Also some optical and airborne imagery was used for selecting training data. Stand-wise forest inventory data were obtained from Etela-Pohjanmaan Metsakeskus, who produce forest management plans for private forest owners in the area, and was updated to year 2006. The forest inventory was produced using standard methods for stand-wise inventory, primarily based on sample plots and visual interpretation. It has been estimated [131] that the error in terms of standard deviation of forest stem volume for this method of inventory is on the average 24.8 percent. Forest stem volume varied (in the area of forest inventory ground data) between 0 and 314 m<sup>3</sup>/ha (area-weighted median 99 m<sup>3</sup>/ha, area-weighted mean 95 m<sup>3</sup>/ha). A total of 123 forest stands from the site were used in the study, with an average stand size of 3 ha.

The **Heinävesi** site (center coordinates: 62°17'N, 28°26'E), located in eastern Finland, was used in the study of forest stem volume retrieval. The area is covered by coniferous (mainly spruce dominated) and mixed forest. The main tree species are the same as at the Kuortane site. The forest inventory ground data of the Heinävesi site was extracted from the forest inventory database of UPM Ltd, which owns the forest area. The earlier ground-measured stem volume data were considered to have a standard deviation of less than 20 percent. In the newest version, the stem volume was obtained from a laser scanning survey (with extensive

## 2. Materials and methods

---

ground sampling) conducted by Arbonaut Ltd in 2004. The laser-derived stem volume data were considered to be more accurate than the earlier ground-measured data. Though no update to year 2006 was performed, the accuracy of forest inventory data can be assumed to be within the same limits as for the Kuortane test site. Stem volume varied between 0 and 425 m<sup>3</sup>/ha (area-weighted median 115 m<sup>3</sup>/ha, area-weighted mean 110 m<sup>3</sup>/ha). The average stand size was 4.8 ha, with 103 forest stands in total. There are practically no agricultural areas in or close to the study site.

The soil at the Heinävesi site is mainly till (glacial drift). The study site is gently hilly. Terrain elevation varies between 82 and 139 m in the area of the forest inventory ground data, and between 70.4 and 200 m in the area of the DEM obtained for an area of 80 km by 110 km from the Finnish National Land Survey.

Dual-pol SAR data acquired over Heinävesi and used in forest stem volume mapping is summarized in Table 2.1.

**Kirkkonummi.** This study site (central coordinates: 60° 11'N, 24°29'E) for study on forest parameter retrieval from Pol-InSAR data, described in Paper IV, was situated near Helsinki, in the municipality of Kirkkonummi. The forest in the area is heterogeneous and consists of small stands alternating with fields and lakes. Forested areas are mostly located on the top of small hills. The dominant tree species are Scots pine, Norway spruce, birch and alder. According to forest inventory information, the stem volume is up to 250 m<sup>3</sup>/ha, with tree heights up to 30 m.

SAR data were collected in Finland during the autumn of 2003 within the FINSAR campaign. It was jointly carried out by the Helsinki University of Technology (now part of Aalto University) and the German Aerospace Center (DLR) Microwaves and Radar Institute. The main instrument used was the DLR E-SAR. The majority of the measurements took place on September 29, 2003. The DLR E-SAR collected five L-band (1.3 GHz) repeat-pass fully polarimetric images with 5 m, 10 m, 12 m, and 0 m baselines from a 3 km altitude. Additionally, an X-band (9.6 GHz) single-pass VV-polarization interferometric image pair was acquired.

**Saariselkä.** The study site for PolSAR mosaicing study (Paper II) was chosen at a high enough latitude to ensure overlap between PolSAR images from the neighboring orbits of the ALOS satellite. The center coordinates of the study site were 68°30'N, 27°30'E. The site represents typical Finnish taiga, with dense and sparse forest covering the majority of the area, with some considerable proportion of open bogs and other peat land. The study area covered the southern part of lake Inari in the north and the eastern end of the Lokka reservoir in the south.

Polarimetric scenes from two adjacent orbits were used in the mosaic production, with imagery acquired on April 2, 2007 (orbit 6327, the eastern part of the mosaic) and on April 19, 2007 (orbit 6575, the western part). For both acquisition days, the temperature had fluctuated near 0 °C during the previous days, with a clear sky before the image acquisition. The snow cover was characterized by processes of transition from dry to wet state. All the scenes were fully polarimetric with an incidence angle of 24 degrees. These polarimetric products have a pixel spacing of about 3.5 m along track (azimuth) and 9.4 m cross track (slant range). Image swath width was 29.3 km.

**Table 2.1.** Dual-polarization SAR data for stem volume mapping in Kuortane and Heinävesi (Paper III).

Scene Id	Site	Mode	Incidence (deg)	Acquisition Time
KD <sub>1</sub>	Kuortane	Dual-pol	39	27.06.2007
KD <sub>2</sub>	Kuortane	Dual-pol	39	12.08.2007
KD <sub>3</sub>	Kuortane	Dual-pol	39	27.09.2007
HD <sub>1</sub>	Heinävesi	Dual-pol	39	12.06.2007
HD <sub>2</sub>	Heinävesi	Dual-pol	39	28.07.2007
HD <sub>3</sub>	Heinävesi	Dual-pol	39	12.09.2007

## 2.2 Methods

In this section, methods used in the studies, both established and newly developed, are described. In the case of spaceborne imagery, the SAR data is radiometrically corrected and orthorectified using in-house software. All the original PolSAR data were single look complex. PolSAR images were preprocessed following the procedures described in [132], [133]. The data were re-sampled independently using bi-linear interpolation with in-house ortho-rectification program [132]. A radiometric normalization was performed to eliminate radiometric variation due to terrain elevation variation. Power of each pixel was normalized with respect to the projected area of the scattering element, analogously to description given, e.g., in [133]. The projection was made to a plane perpendicular to the propagation direction of the incoming radar pulse. This form of radiometric normalization eliminates the topographic effects on received power in terrain types whose radar cross-section per unit of projected area is independent of the incidence angle. More detailed discussion and derivation of methods used can be found in corresponding sections of Papers I–V.

### 2.2.1 Land cover mapping with PolSAR data

When performing classification or segmentation of PolSAR data acquired over natural area, the second order statistics of PolSAR data are usually used. These include methods suitable for operating with covariance matrices themselves, or with polarimetric features derived from them. In the latter case, all classification methods originally intended for intensity data can be used. On the other hand, many techniques, tailored especially for PolSAR data, are well-known, and can be easily found in literature, starting from Wishart distance classifier to decision trees. First, well-established techniques are mentioned briefly, followed by more in-depth overview of techniques that contribute to originality of studies reported in the thesis.

## 2. Materials and methods

---

### 2.2.1.1 Entropy-alpha-anisotropy analysis

A popular unsupervised target classification method is based on eigendecomposition of the polarimetric coherence matrix [24], [40]. It uses such polarimetric characteristics for description of target properties as entropy and the averaged alpha angle. Entropy  $H$  covers a dynamic range from 0 to 1, being a measure of randomness of the scatterer, from deterministically polarized to isotropically depolarized scatter, respectively. The alpha angle  $\alpha$  characterizes through a unitary transformation a scattering mechanism (0 is a sphere symmetry, 45 a dipole, 90 a dihedral or helix) independently from a rotation of the measurement coordinates. The mentioned model is further augmented by the anisotropy measure  $A \in [0, 1]$  to distinguish between different classes with similar cluster centers, differentiating between single and multiple target return.

The categorized map of the alpha angle against entropy provides initial classification of PolSAR imagery, after which anisotropy can be used for further analysis.

### 2.2.1.2 Wishart classification

More advanced semi-supervised approaches [134], [135] use maximum likelihood (ML) classification, initially seeded by the H/A/ $\alpha$  classes and further iterated by the complex Wishart distribution of the coherency matrix. The complex Wishart algorithm is generally a ML-estimator, assigning each sample coherency matrix to one of the associated classes on the basis of the minimum Wishart matrix distance. Further manual labeling of the obtained segments is performed to produce a land cover/use map.

In supervised Wishart classification, training areas are defined manually for each class from the Pauli color-coded presentation or reference ground plot data. Then the classifier calculates the Wishart statistics of the training areas and assigns each pixel to the closest class using maximum likelihood decision rule. The accuracy of the classification is further evaluated against the reference data. An interface implementation provided by the ESA PolSARpro software [136] was used for supervised Wishart classification.

Use of the Wishart matrix pdf based techniques is a widely accepted practice in PolSAR classification, and they were particularly employed in Paper II and Paper IV, primarily for benchmarking purposes.

### 2.2.1.3 Probabilistic Neural Network

In order to capture non-Gaussian statistics of polarimetric features, nonparametric classification method based on PNN was used. It belongs to the kernel density estimation techniques and was originally introduced in [54]. The PNN is a feed-forward artificial neural network, and it takes advantage of non-parametric pdf estimation. More particularly, it uses Parzen window probability density estimation [137], which allows approximating smooth pdfs, when the window size and estima-

tion kernel function are provided. Choice of the Parzen window weighting function affects the generalization capability of PNN. Typically the Gaussian function is adopted for this purpose, and then the only parameter to be supplied externally is the sigma smoothing parameter, defining the size of a pixel neighborhood taken into account during calculation of the pdf-approximation. If the weighting function is too narrow, the performance will be the same as for the nearest neighbor classifier. PNN normally consists of 4 layers: input layer, hidden (pattern) layer, class (summation) layer, and decision layer (or node). The typical structure of PNN is shown in Figure 2.2.

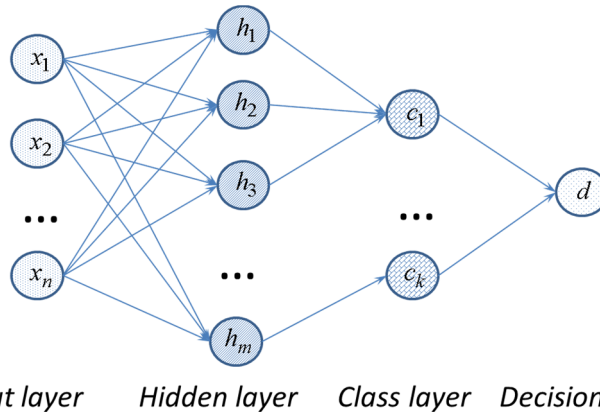


**Figure 2.2.** Typical structure of probabilistic neural network (Paper IV).

The **input layer** consists of neurons corresponding to predictor variables (i.e., features describing a pixel). The input neurons supply the input values to each of the neurons in the hidden (pattern) layer. Data supplied into the network should be normalized to unitary length. The **hidden (pattern) layer** is represented by  $m$  nodes corresponding to training samples (e.g., each pixel from the training data set). The nodes store values of the features for the training sample along with the target class value. A hidden neuron computes the distance of the test case from the neuron's center point and then applies the radial basis kernel function using the sigma smoothing parameter. The result is passed further to the neurons in the class layer. The **class (summation) layer** consists of neurons for each category of the target variable. The actual target category of each training sample is stored with each hidden neuron. The weighted value coming out of a hidden neuron is fed only to the class neuron that corresponds to the hidden neuron's category. The class neurons add the values for the class they represent (hence, it is a weighted vote for that category). This way a pdf-approximation is effectively obtained for each class (target category). The **decision layer (node)** compares the weighted votes for each target category accumulated in the class layer and uses the largest vote to predict the class according to the Bayesian decision rule.

When the number of training plots increases to infinity, the estimated pdfs converge to the true ones, and the PNN-classifier converges to the optimum Bayesian classifier. The network does not require training as such, compared to multilayered perceptron. It is easy to extend by incorporating additional training data as the hidden layer neurons, and does not exhibit over-fitting typical for back-propagation neural networks. However, some limitations on the use of PNNs include: high memory requirements, as the whole network must be stored in the memory; relatively low classification speed, as each processed pixel, in order to be classified, should be propagated through the whole network model; slightly poorer generalization capability than that of multilayered perceptron. The effect of these drawbacks can be somewhat reduced by more efficient or adaptive configuration of PNN [138], [139], [140]. The main drawback, typical for any non-parametric approach, is sensitivity of PNN to the representativeness of the training data.

### 2.2.1.4 PolSAR model-based decomposition

Model based decompositions are used in order to express the covariance matrix as a linear combination of different scattering contributions. For analysis of backscatter in natural environment the Freeman-Durden decomposition is widely used. It models the covariance matrix as

$$\mathbf{C} = P_d \mathbf{C}_d + P_s \mathbf{C}_s + P_v \mathbf{C}_v, \quad (2.1)$$

where  $C_i$  and  $P_i$  represent double-bounce, surface and volume scattering components and powers respectively, with

$$\text{Span}(\mathbf{C}) = P_s + P_d + P_v. \quad (2.2)$$

It assumes the presence of reciprocal medium with reflection symmetry, leading to complete decorrelation of the co-polarized and cross-polarized backscattering coefficients, which was shown to be approximately valid for majority of natural and distributed targets using P-, L-, and C-band sensors.

According to the algorithm outlined in [26], the volume component power can be estimated directly and subtracted from other contributions. A drawback of this approach is possibility of obtaining negative power estimates of surface or double-bounce scattering in urban and geometrically complicated forest environments. The primary reason for this is speckle, which can be tackled by additional extensive averaging [27]. Another reason is that the volume component power tends to be overestimated in the Freeman-Durden model, as all the cross-polarized backscatter power is assigned the volume scattering mechanism.

Different solutions for this problem were widely discussed in the recent literature [35], [36], [37], [38], [39], [141] leading to a series of improvements and empirically based adaptations, particularly with respect to the analysis of urban areas. These modifications can be roughly divided into two main categories. The first

category introduces additional scattering components into the overall backscatter model. For instance, use of additional helix scattering contribution was suggested in [34], while the combination of helix and wire terms in the multiple-component scattering model demonstrated in [142] was reported to improve analysis of buildings in urban areas using airborne PolSAR data. However, these contributions are expected to be negligible in forest dominated natural terrain. The second category deals directly with the model for description of volume backscatter. Discussion on the benefits and drawbacks of some of these models can be found in Paper I. Because accurate modeling of the volume scattering component defines the possibility of successful physically consistent decomposition, it is addressed here in more detail.

In Paper I, a generalized volume scattering mechanism model was proposed, motivated by geophysical media symmetry considerations. The model accounts for the  $\langle |S_{hh}|^2 \rangle \neq \langle |S_{vv}|^2 \rangle$  case in the continuous form when modeling backscatter from canopy, which may be beneficial compared to decision rule approach adopted in, e.g. [34]. Under the reflection symmetry assumption for reciprocal media, the covariance matrix for backscatter, regardless of actual physical scattering mechanism (volume or surface), obeys the following expression [143]:

$$\mathbf{C} = \frac{1}{1 + e + \eta} \begin{bmatrix} \gamma & 0 & \rho\sqrt{\eta} \\ 0 & e & 0 \\ \rho^*\sqrt{\eta} & 0 & 1 \end{bmatrix}, \quad (2.3)$$

with ratios  $\eta = \langle |S_{hh}|^2 \rangle / \langle |S_{vv}|^2 \rangle$ ,  $e = \langle 2|S_{hv}|^2 \rangle / \langle |S_{vv}|^2 \rangle$  and the complex-valued HH-VV correlation coefficient  $\rho = \langle S_{hh}S_{vv}^* \rangle / \sqrt{\langle S_{hh}S_{hh}^* \rangle \langle S_{vv}S_{vv}^* \rangle}$ .

This result is valid not only for forest, but also for several other types of anisotropic media. If further a rotation symmetry requirement for all elements of covariance matrix is additionally imposed, it will result in standard volume scattering model [26], valid for azimuthally symmetric media.

Assuming HH-VV correlation coefficient  $\rho$  to be real valued, and setting rotation symmetry requirement only for  $\langle S_{hh}S_{vv}^* \rangle$  term in the linear rotation basis, it can be shown as in [143] that  $e = (1 + \gamma - 2\rho\sqrt{\eta})/2$ . After substitution of  $e$  into (2.3), the following covariance matrix model for volume backscatter is obtained:

$$\mathbf{C}_v = \frac{1}{\frac{3}{2}(1+\eta) - \rho\sqrt{\eta}} \begin{bmatrix} \gamma & 0 & \rho\sqrt{\eta} \\ 0 & \frac{1+\eta}{2} - \rho\sqrt{\eta} & 0 \\ \rho^* \sqrt{\eta} & 0 & 1 \end{bmatrix}. \quad (2.4)$$

This model, called the Generalized Volume Scattering Model (GVSM), was shown to agree with the majority of other existing models (see Paper I). However, in order to derive a new three-component model based decomposition, model (2.4) should be simplified. Freeman has shown in his two-component model fitting [27] that for different types of forests value of the “shape parameter”  $\rho$  is likely to be between 0.3 and 0.4, making the model of thin dipoles [26] generally valid. Setting  $\rho = 1/3$  yields

$$\mathbf{C}_v = \frac{1}{\frac{3}{2}(1+\eta) - \sqrt{\eta}/3} \begin{bmatrix} \eta & 0 & \sqrt{\eta}/3 \\ 0 & \frac{1+\eta}{2} - \sqrt{\eta}/3 & 0 \\ \sqrt{\eta}/3 & 0 & 1 \end{bmatrix}. \quad (2.5)$$

Model (2.5), as well as (2.4), is suitable under the transformation  $\eta' = 1/\eta$ , which allows its use for description of both randomly oriented particles and particles aligned in some preferable direction (i.e. dipoles, because of the limitations on  $\rho$ ). A particular advantage of model (2.3) is that it continuously covers the whole dynamic range of values for  $\varepsilon = 10 \log(\eta)$ , especially where the majority of pixels are usually expected to belong ( $|\varepsilon| < 2$  dB). There is also a parallel between models (2.4), (2.5) and the straightforward regularized approach suggested in [35]. The difference is, however, that while parameter  $a$  influences  $\langle S_{hh} S_{hh}^* \rangle$  and  $\langle S_{vv} S_{vv}^* \rangle$  terms of the model in the same manner, GVSM allows subtracting more from the bigger term and less from the smaller one, which improves the solution. It is expected that model (2.5) will be adequate for canopy exhibiting the HH-VV ratio at the level of  $|\varepsilon| < 12$  dB, which is in agreement with limits obtained in [31] and seems to be enough for practical situations.

Model (2.5) was directly incorporated in the Freeman-Durden framework for analysis of backscatter in natural terrain, with surface and double-bounce scattering modeled as:

$$\mathbf{C}_s = \frac{1}{1 + |\zeta|^2} \begin{bmatrix} |\zeta|^2 & 0 & \zeta \\ 0 & 0 & 0 \\ \zeta^* & 0 & 1 \end{bmatrix}, \quad \text{Im}(\beta) = 0, \quad (2.6)$$

$$\mathbf{C}_d = \frac{1}{1 + |\varrho|^2} \begin{bmatrix} |\varrho|^2 & 0 & \varrho \\ 0 & 0 & 0 \\ \varrho^* & 0 & 1 \end{bmatrix}. \quad (2.7)$$

Denoting backscatter contributions to the VV cross-section as  $f_d = P_d / (1 + |\varrho|^2)$ ,  $f_s = P_s / (1 + |\zeta|^2)$  and  $f_v = P_v / (1.5(1 + \eta) - \sqrt{\eta}/3)$ , the following set of equations to be solved was obtained:

$$\langle |S_{hh}|^2 \rangle = |\varrho|^2 f_d + |\zeta|^2 f_s + \eta f_v, \quad (2.8)$$

$$\langle |S_{hv}|^2 \rangle = \left( \frac{1 + \eta}{2} - \frac{\sqrt{\eta}}{3} \right) f_v / 2, \quad (2.9)$$

$$\langle |S_{vv}|^2 \rangle = f_d + f_s + f_v, \quad (2.10)$$

$$\langle S_{hh} S_{vv}^* \rangle = \varrho f_d + \zeta f_s + \sqrt{\eta} / 3 f_v \quad (2.11)$$

As  $\eta$  is estimated directly “externally” (thus representing a data adjustment term), the flowchart of the decomposition adopted is the same as in the Freeman-Durden decomposition. Then powers of scattering mechanisms can be estimated trivially, yielding the final decomposition.

### 2.2.1.5 Retrieval of soil type under vegetation

In Paper IV, a problem of separating mineral soils and peatland in forest covered areas using L-band PolSAR was considered. As CLC2006 data were used in the study, primary classes (mineral and peatland under forest cover) were obtained by merging respective forest classes as defined in CLC2006: coniferous, deciduous, mixed forests over mineral soil and peatlands. In a common scenario of assessing properties of layer under vegetation, one should take care about removing the effect of vegetation. Several techniques, employed e.g. in radar-based soil moisture retrieval and snow cover mapping, compensate for vegetation contribution in the overall backscatter using physics-based modeling and semi-empirical approaches [31], [75], [144], [145], [146].

However, the aim was not to completely compensate forest vegetation effects. The under storey vegetation in the boreal forest reflects the site and soil types [147], [148], this way improving discrimination capability in soil type retrieval. On the other hand, in areas of very high and dense forest cover in unfrozen conditions it could be unrealistic to assume good penetration to ground layer, even at L-band.

In Paper IV, a semi-empirical scheme was proposed, utilizing a priori information about forestry practices and general environmental characteristics of the Finnish forest. According to the latter, areas with high forest are mostly grown over mineral soil areas, and can be directly assigned the corresponding soil type. Then, for the other areas, with presumably less high (and/or less dense) forest, where the ground contribution is relatively strong, the soil type classification is performed. As an indication of relative forest density and height, ratios of powers of basic scattering mechanisms were used as inputs to a linear decision rule. The powers can be provided by simple model-based PolSAR decompositions, yielding results in the manner close to the so-called Radar Vegetation Index [36], [149].

On the first step, a three-component polarimetric decomposition is performed over forest-covered areas. The initial forest-covered area can be either imported directly from CLC2006, or, in a more coherent classification scenario, results of the multi-class classification experiment can be used.

Then, the scattering mechanism powers obtained are used in a linear decision rule of the type  $(P_s > G * P_v)$ , where  $P_s$  and  $P_v$  are powers of surface and volume scattering, respectively, and  $G$  is a weighting coefficient. The double bounce contribution tends to be quite weak in the boreal forest environment [66], [75], and, for this reason, is not included in the decision rule. The default value of  $G$  is set to 1. Regions, where the decision rule is not fulfilled, are masked as areas with high and/or dense vegetation, and automatically assigned the mineral soil type. For other regions, marked as relatively sparse and/or low forest, because of the significant surface scattering contribution, one can implement any chosen classification method, e.g. ML- or PNN-based classifications. Afterwards, the results are assimilated to produce a final soil-type thematic map. The flowchart of the processing chain is depicted in Figure 2.3.

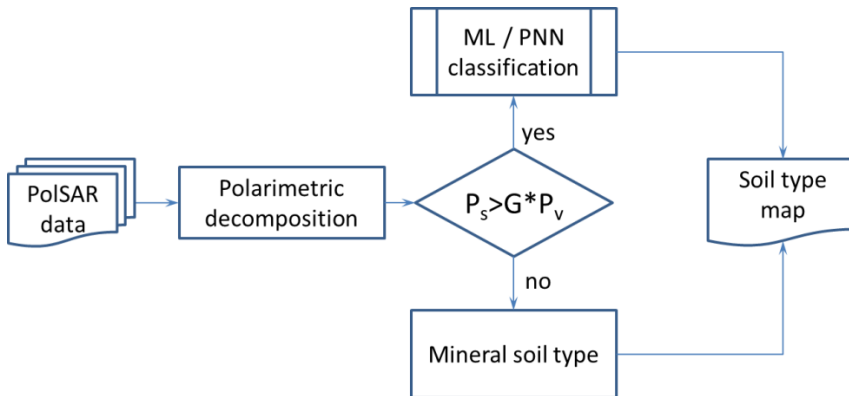


**Figure 2.3.** Processing chain for soil type retrieval under forest vegetation (Paper IV).

The coefficient  $G$  might be chosen using the training data set in such a manner, that it delivers a maximum possible separation between mineral and peatland pixels in the training data set. More specifically, the procedure of fitting the  $G$ -parameter value exactly follows the flowchart depicted in Figure 2.3, except that only the training data were used in this procedure. The value of  $G$  that delivers maximum accuracy on the training data set itself (calculated from the confusion matrix of the training data set) was chosen for the final classification procedure.

#### 2.2.1.6 PoISAR mosaic normalization

In order to avoid geometric errors and to supplement the available ALOS image geometry information, manually measured ground control points (GCPs) and automatically measured tie-points were used to revise image geometry. The GCPs were measured in the down-averaged PALSAR scenes and map data from the map service of the Finnish Land Survey. The tie-point and GCP observations were submitted to a block adjustment procedure [59], where three geometry-revision parameters were determined for each scene: translation in northing and easting, and rotation. These parameters were solved using least squares adjustment, which minimizes approximation error over the whole set of observations. The initial geometry information in ortho-rectification was based on the equations presented in [150].

In the context of the herein described polarimetric mosaic production we can identify several possible methods for further reduction of radiometric differences between the acquired PoISAR scenes. While it is not possible to correct for the change in scattering mechanisms that actually took place because of the seasonal changes (snow melting), eliminating radiometric difference between neighboring stripes (called further “normalization”) has proved to be an important image processing step capable of improving further classification results [61].

Such a normalization technique could be implemented, e.g., for each component of the polarimetric coherency (or covariance) matrix. This would, however, result in an unpredictable change of scattering mechanisms after normalization, if the correction coefficients were different for different components of the coherency matrix.

Another option is the use of span of the covariance matrix (or total backscattered power TP) in order to calculate the corrective gain. Afterwards, a pixel-by-pixel multiplication of the whole covariance matrix  $\mathbf{C}$  by the obtained corrective gain can be performed, ensuring preservation of scattering mechanisms for each processed pixel. Technically, the approach follows the method suggested for balancing the intensity between neighboring strips of single-polarization SAR imagery [61], but uses values of TP instead. In this study only two neighboring orbits were available, and scenes acquired on the right orbit are corrected with respect to the left-orbit scenes. The correction procedure simplifies to calculating normalization ratio

$$R_{rl} = \langle P_{total}^l \rangle / \langle P_{total}^r \rangle, \quad (2.12)$$

where  $P_{total}^i$  is the respective TP for  $i$ -th orbit, and  $\langle \rangle$  denotes spatial averaging over certain area. New covariance matrix values for the right-orbit scenes are obtained as

$$\hat{\mathbf{C}} = R_{rl} \cdot \mathbf{C}. \quad (2.13)$$

This approach preserves polarimetric relations and modifies only the respective TP values. As TP is an important feature characterizing a pixel, it was of interest to evaluate the effect of the seam-hiding procedure proposed on land cover classification performance.

Then possible normalization methods, further evaluated in this study, include the PolSAR mosaic correction using the normalization ratio  $B_{rl}$  calculated:

- Method 1)** at the whole extent of the mosaiced scenes;
- Method 2)** only from the overlapping areas between the mosaiced scenes;
- Method 3)** using only those pixels from the overlapping areas, where a dominating scattering mechanism is preserved [41]. This ensures that pixels that significantly changed their backscattering signature are excluded from calculation. The corresponding powers of the scattering mechanisms can be provided by incoherent PolSAR decompositions, considering the primarily natural-media composition of the imaged area.

### 2.2.2 Forest parameter retrieval with multi-parametric and interferometric SAR

Here, several methods useful in retrieval of forest parameters, namely forest stem volume and tree height, are discussed, along with the need for further development justified. Important modifications of inversion procedures for forest stem volume and forest tree height retrieval suggested in Paper III and Paper V are presented.

#### 2.2.2.1 Forest stem volume estimation with multitemporal SAR

Analysis of SAR backscatter aimed at establishing a relation between forest stem volume and  $\sigma^0$  is performed using the semi-empirical boreal forest model [151]. This model was originally developed for shorter wavelengths, and was primarily intended for interpreting SAR backscatter at C-band [152]. However, due to a relatively weak double-bounce backscattering mechanism in taiga forest due to the forest floor [66], [75], [85], [94], the model was found to give satisfactory results also at L-band [75], [76]. Moreover, it inherently captures the nonlinearity between the SAR backscatter and forest stem volume (or above ground biomass), thus being comparable to other empirical and semi-empirical methods [30].

This model itself was originally introduced in [151]. The model assumes a relatively homogeneous forest canopy within a forest stand (or compartment); the forest canopy backscatter is described as a function of stem volume and volumetric vegetation moisture [75], [152]. The general expression for backscatter from a forest stand with stem volume  $V$  takes the following form:

$$\sigma_{model}^0 = \frac{C_1}{-2C_2} \left( 1 - e^{2C_2V} \right) + C_3 e^{2C_2V}, \quad (2.14)$$

where the first additive term represents the backscattering component of the forest canopy and the second part is the backscattering contribution from the ground. Model (2.14) was originally developed for X- and C-band, where coefficients  $C_1$ ,  $C_2$ , and  $C_3$  had an actual physical meaning.  $C_1$  and  $C_2$  are related to the volumetric water content of forest canopy in terms of water cloud model [153] and represent the effective volume scattering coefficient and the effective forest canopy extinction coefficient, respectively, while  $C_3$  represents backscatter from the ground. At L-band, these coefficients are considered empirical, and should be estimated from the training (reference) data and SAR data. An alternative formulation of the model, making it somewhat easier to provide an interpretation, was given in, e.g., [85]:

## 2. Materials and methods

---

$$\sigma_{model}^0 = \sigma_{veg}^0 \left(1 - e^{-\beta V}\right) + \sigma_{gr}^0 e^{-\beta V}, \quad (2.15)$$

where  $\sigma_{veg}^0$  and  $\sigma_{gr}^0$  denote backscatter from the vegetation and ground respectively, and  $\beta$  is an empirical coefficient.

Then, on the first step of inversion, the model training is performed using non-linear least-squares fitting for available  $N$  training forest stands:

$$\left\{ \hat{\beta}, \hat{\sigma}_{veg}^0, \hat{\sigma}_{gr}^0 \right\} = \operatorname{argmin}_{\beta, \sigma_{veg}^0, \sigma_{gr}^0} \left\{ \sum_{i=1}^N \left[ \left\langle \sigma_{i,meas}^0 \right\rangle - \sigma_{i,model}^0 \left( V, \beta, \sigma_{veg}^0, \sigma_{gr}^0 \right) \right]^2 \right\}, \quad (2.16)$$

where  $\left\langle \sigma_{i,meas}^0 \right\rangle$  denotes measured backscattering coefficient spatially averaged over the  $i$ -th training forest stand.

On the second step, the model inversion for the  $j$ -th stand with backscattering coefficient  $\sigma_{j,meas}^0$ , and stand-wise stem volume estimation for the total test site area is performed as:

$$V_{j,model} = \left( -\frac{1}{\beta} \right) \ln \left( \frac{\sigma_{veg}^0 - \sigma_{j,meas}^0}{\sigma_{veg}^0 - \sigma_{gr}^0} \right). \quad (2.17)$$

However, in, e.g., [85], [95] fitting was performed using the forward model in the manner given by (2.16). On the other hand, when using the inverted model (2.17) in the fitting procedure, it becomes possible to avoid some of the drawbacks, associated with inversion of the model fitted by (2.15). In particular, this can help with the difficulty of estimating stem volume for some stands, where  $\sigma_{j,meas}^0 \geq \sigma_{veg}^0$ , or producing negative stem volume estimates under  $\sigma_{j,meas}^0 < \sigma_{gr}^0$ . Then, as presented in Paper III, the parameters of model (2.17) are estimated using nonlinear least-squares optimization in the following manner:

$$\left\{ \hat{\beta}, \hat{\sigma}_{veg}^0, \hat{\sigma}_{gr}^0 \right\} = \operatorname{argmin}_{\beta, \sigma_{veg}^0, \sigma_{gr}^0} \left\{ \sum_{i=1}^N \left[ V_i - V_{i,model} \left( \left\langle \sigma_{i,meas}^0 \right\rangle, \beta, \sigma_{veg}^0, \sigma_{gr}^0 \right) \right]^2 \right\}. \quad (2.18)$$

However, it still might be that estimates of stem volume go negative. In this case, a simple decision is to mask out these areas as non-forested areas, and to set the stem volume level for them to zero.

Fitting the inverted model might lead to somewhat suboptimal results when using estimated parameters in the forward model in order to explain the behavior of backscattered signal, but our goal here is to develop a reliable stem volume retrieval approach.

One possible way of exploiting multitemporal information is to perform multitemporal averaging. A considerable benefit of such multitemporal averaging is speckle reduction [154]. This is expected to work well if the acquisition geometry is the same in the processed multitemporal stack. This can be considered the most straightforward way, and was applied in, e.g., [86]. With this idea in mind, it makes sense to evaluate performance of the inversion approach (2.18) using such an averaged product. As it concerns linearly combining different polarization channels in multi-polarization imagery, the speckle reduction persists [155], but physical justification for use of the described inversion process becomes less clear.

Another way to take advantage of several available SAR scenes, as was implemented in Paper III, is to use them in a multiple regression approach, using the stem volume estimate from each particular scene as an independent variable. Then final estimation of stem volume based on  $k$  SAR images will be a linear combination of stem volume estimates from each individual SAR image. The expression for the optimal regressor takes the following form:

$$V_j^\Sigma = \overrightarrow{L_1} \overrightarrow{V_{j,est}} + L_2. \quad (2.19)$$

where  $V_j^\Sigma$  is an optimal estimate of stem volume of  $j$ -th forest stand,  $\overrightarrow{V_{j,est}}$  is a vector of length  $k$  of stem volume estimates of the same  $j$ -th stand from  $k$  individual SAR images according to (2.17)-(2.18). Parameter  $L_2$  is required to compensate for systematic bias, expected due to non-accounted scattering mechanisms in model (2.15), e.g., the missing contribution from ground-trunk interaction. Regression parameters  $\overrightarrow{L_1}$  and  $L_2$  are obtained at the training stage by solving the optimization problem in the least squares sense:

$$\left\{ \overrightarrow{\hat{L}_1}, \hat{L}_2 \right\} = \underset{\overrightarrow{L_1}, L_2}{\operatorname{argmin}} \left\{ \sum_{i=1}^N \left[ V_i - \left( \overrightarrow{L_1} \overrightarrow{V_{i,est}} + L_2 \right) \right]^2 \right\}. \quad (2.20)$$

These multiple regression coefficients are calculated using stem volume estimates inverted using a training dataset. Then the multiple regression coefficients obtained will be used for combining stem volume estimates inverted using (2.17) from the validation dataset. The basic flowchart of the overall training and inversion approach for stem volume retrieval is shown in Figure 2.4, and roughly corresponds to the operational scenario one might normally expect.

Accuracy of forest stand volume estimation is traditionally evaluated in terms of root mean square error (RMSE), given by

## 2. Materials and methods

$$RMSE = \sqrt{\left[ \sum_{i=1}^N (V_{i,meas} - V_{i,est})^2 \right] / N}, \quad (2.21)$$

where  $V_{i,meas}$  and  $V_{i,est}$  are the measured and estimated stem volume for  $i$ -th stand, and  $N$  is the number of stands. In case forest stands vary strongly in size, area-weighted RMSE might be used for interpretation. In this approach, the deviations of individual forest stands are weighted by the respective stand areas, and divided by the overall area before taking the square root:

$$RMSE = \sqrt{\left[ \sum_{i=1}^N (V_{i,meas} - V_{i,est})^2 S_i \right] / \sum_{i=1}^N S_i}, \quad (2.22)$$

where  $S_i$  is the area of  $i$ -th stand.

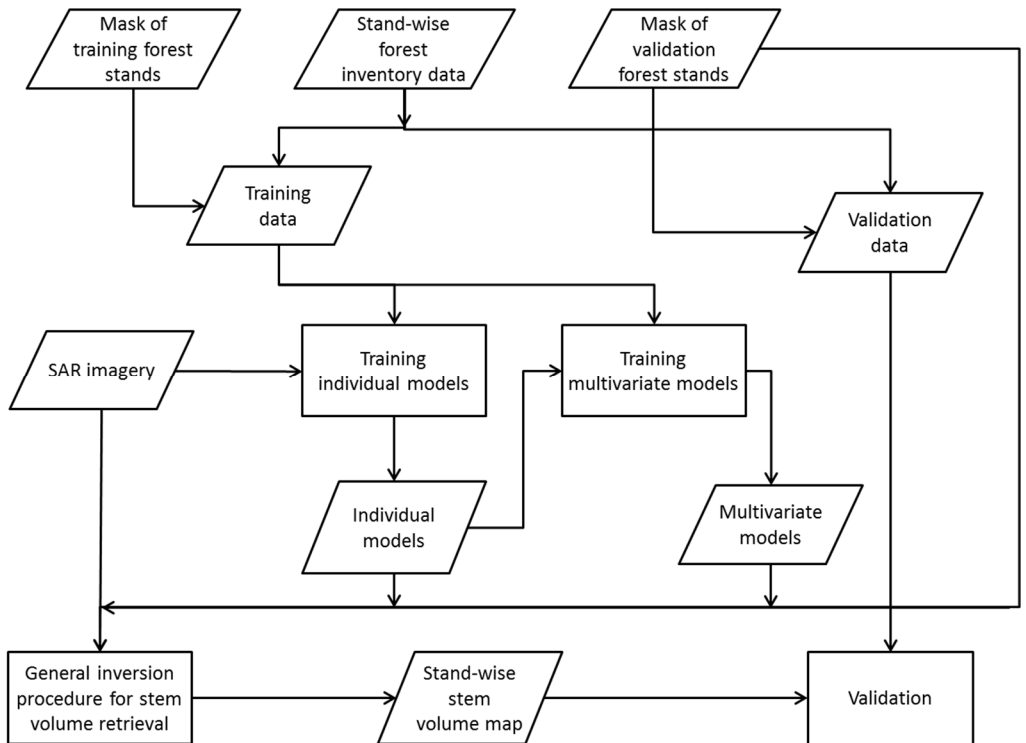


**Figure 2.4.** Flowchart of the forest stem volume retrieval approach (Paper III).

## 2.2.2.2 Forest parameter retrieval using SAR interferometry

In order to include ground phase from the reference DEM into RVoG based forest height retrieval, the LIDAR measured DEM and CHM were transferred to slant range coordinates by using E-SAR range and azimuth geocoding tables. The missing pixels in slant range maps were recovered by two-dimensional interpolation. The ground phase  $\phi_0$  can be represented in terms of the SAR vertical wavenumber  $k_z$  and terrain elevation  $h_{DEM}$  as

$$\phi_0 = k_z (h_{DEM} + h_f) + \phi_f, \quad (2.23)$$

where  $h_f$  and  $\phi_f$  are unknown constants, unique for each interferogram. The vertical wavenumber  $k_z$  is a parameter describing the interferometric measurement. It depends on the radar wavelength  $\lambda$ , incidence angle  $\theta$  and incidence difference between interferometric measurements  $\Delta\theta$  as  $k_z = 4\pi\Delta\theta(\lambda \sin(\theta))^{-1}$ . Note that this parameter varies along the range and depends on the actual flight tracks. The two unknown constants  $h_f$  and  $\phi_f$  were recovered by fitting the DEM-generated ground phase  $\phi_0$  with the SAR-measured ground phase  $\phi_\gamma$  in open areas in the least squares sense, assuming that they should coincide. The open areas were chosen by a simple empirical coherence value threshold ( $\gamma > 0.97$ ), and appropriate parameters were obtained as a solution to the optimization problem:

$$\hat{h}_f, \hat{\phi}_f = \arg \min_{h_f, \phi_f} \sum \left\| e^{i(k_z (h_{DEM} + h_f) + \phi_f)} - e^{i\phi_\gamma} \right\|^2, \quad (2.24)$$

The obtained values were further used to produce a ground phase  $\phi_0$  estimate for the entire test site using (2.23). The derived ground phase estimate was in good agreement with interferometric SAR phase in open areas and the assumption is that it also produces a good estimate for theoretical ground phase inside the forest canopy where radar signals do not reach ground level.

Further, the SPC height and forest extinction are analyzed with respect to reference topographic phase according to the RVoG model. RVoG is a simple model for describing interferometric coherence as a function of the following parameters of random volume layer: layer height or thickness, ground location, extinction coefficient, and ground reflection contribution. It assumes the presence of a uniformly dense layer that is characterized by mean wave extinction in the canopy, ignores the coherence drop due to independent double-bounce (ground-

volume reflection) contributions, and neglects higher-order ground-volume interactions. Stated simply, the model calculates the balance between the polarized ground reflection and random canopy reflection as a function of random volume parameters. The RVoG model states that the polarization dependent complex coherence  $\gamma(\vec{\omega})$  for a volume above the ground can be modeled as in [108] and is presented here as found in [118]:

$$\gamma(\vec{\omega}) = e^{i\varphi_0} \left[ (\gamma_V - 1) \left( 1 + M(\vec{\omega}) e^{h\sigma_m} \right)^{-1} + 1 \right], \quad (2.25)$$

where  $h$  is the height of the volume layer,  $\phi_0$  is the ground phase,  $M$  is the ground-to-volume amplitude ratio parameter, and  $\gamma_V$  is the volume decorrelation, i.e., the complex coherence affected exclusively by decorrelation of the random volume. The ground-to-volume amplitude ratio  $M$  is related to the ground contribution parameter  $m$ , and is often used in the RVoG model as  $m(\vec{\omega}) = M(\vec{\omega}) e^{h\sigma_m}$ . The volume decorrelation  $\gamma_V$  is calculated as

$$\gamma_V = \frac{e^{h(\sigma_m + ik_z)} - 1}{(1 + ik_z \sigma_m^{-1}) (e^{h\sigma_m} - 1)}, \quad (2.26)$$

where  $k_z$  is the vertical wavenumber, describing the measurement system.  $\sigma_m = 2\sigma / \cos\theta$  is defined by the mean extinction  $\sigma$  and local incidence angle  $\theta$ . The model (2.25) clearly consists of two main parts: volume decorrelation and ground contribution. If we assume that the ground phase  $\phi_0$  and the measured coherence phase  $\phi_\gamma$  are known, we can calculate the phase  $\Delta\phi = \phi_\gamma - \phi_0$  that is introduced solely by the canopy. Here, temporal decorrelation was neglected for L-band repeat pass and X-band single-pass acquisitions.

In Paper V, RVoG was used as a study framework and a basis for an algorithm development aimed at simultaneous retrieval of forest tree height and forest extinction. First, the analysis of the SPC location in the forest volume allowed identifying three special boundary cases where RVoG model can be strongly simplified for easier understanding:

**Case 1.** The ground contribution is missing,  $M \rightarrow 0$ , and extinction is very large,  $\sigma_m \rightarrow \infty$ . In this case, the phase height can be expressed as  $\Delta\phi = k_z h$  (see Paper V). SPC is located at the top of the volume layer, i.e., the backscatter arrives from the top of the canopy and is independent of polarization. This particular case is related to the Random Volume (RV) model used in [156],

where the tree crown was described as a random volume with no waves penetrating into the trunk and ground layers, and with all polarizations having the same penetration depth.

**Case 2.** The second boundary case appears when the ground reflection is negligible,  $M \rightarrow 0$ , and the canopy extinction is very small,  $\sigma_m \rightarrow 0$ . While this is merely a hypothetical case, it still provides some useful insight to the expected behavior of the model. Here, the expression for the phase height becomes  $\Delta\phi = 0.5k_z h$  (see Paper V); SPC is situated halfway within the random volume.

**Case 3.** The third distinguishable case is characterized by a significant ground contribution,  $M \gg 0$ . In this scenario, the phase height is  $\Delta\phi \approx 0$  regardless of forest height and extinction values. This means that when the phase center is located close to ground, interferometric coherence does not contain significant information anymore about the volume layer, which is also easy to understand intuitively.

It should be noted that according to the first two cases, the scattering center cannot be lower than half of the canopy height when the ground contribution is negligible or completely missing, regardless of the extinction value. Then, provided the ground phase  $\phi_0$  is known, both the volume height and the extinction coefficient can be calculated directly even with single-polarization complex coherence using the volume decorrelation equation (2.26). Also, the coherence amplitude has a special interpretation when the canopy is lossless, i.e.  $\sigma_m \rightarrow 0$ . The RVoG model when void of extinction is a non-normalized sinc-function (however, with only half of the argument). It is equivalent to the polarization-coherence-tomography [157], provided that the ground phase is accounted for. The so-called sinc-approximation can be used to calculate a rough tree height estimate using only coherence amplitude; however, this usually leads to height overestimation [158].

The three aforementioned boundary cases provide theoretical limits. However, in practical situations SPC can be located anywhere inside the canopy being only limited by a certain range of coherence values. Nevertheless, these boundary cases provide some useful interpretation tools. For example, if the SPC is located at lower than half of the actual tree height, it could indicate the presence of a ground reflection contribution according to the RVoG model. Generally, one can expect the first described boundary case of the RVoG model to be applicable to densely forested areas at X-band (significant extinction, ground contribution practically absent), and the third case could describe sparse forest at L-band (insignificant extinction along with strong ground contribution). When processing experimental data, it is realistic to expect that the observed backscatter will follow some intermediate scenario. Finally, the second case can be expected to provide a rough initial height estimate, primarily for a very high canopy.

Thus, the assumption that the ground contribution is not significant practically reduces the RVoG model to the random volume decorrelation model (2.26), with

the exception that the ground phase is accounted for in this representation. Then, when the ground phase is known, the RV decorrelation model is used to retrieve both the tree height and extinction coefficient from single-pol InSAR measurements.

However, in order to use this simplified approach, one should develop criteria to determine areas where ground contribution is so small that it can be neglected. This was done in Paper V, where both the ground phase and the forest tree heights were known. Then, for a given complex coherence, the following criteria can be used to determine whether ground contribution is insignificant:

**Criterion 1.** SPC is located above half of the tree height. As discussed above according to the RVoG model, the scattering phase center is always located in the upper half of the canopy volume when the ground contribution is missing.

**Criterion 2.** The magnitude of the coherence is larger than the “*sinc*-approximated” value for identical tree heights. According to the previous discussion, the “*sinc*-approximated” height overestimation is caused by canopy extinction.

Obviously, the above proposed criteria for selecting areas with insignificant ground contribution cannot be applied when independent tree height measurements are not available. In Paper V, analysis of LIDAR DEM and CHM against complex interferometric coherence allowed to select areas with negligible ground contribution based only on the SPC height and the coherence magnitude. For example, for X-band it was found that when: 1)  $|\gamma| > 0.9$ ; and 2) (SPC height)  $>$  (12 m above ground DEM); then the respective areas with no ground contribution were similar to those obtained using Criteria 1 and 2.

This altogether has led to development of a simple combined approach for forest parameter retrieval (Paper V). For areas with negligible ground contribution, inversion of model (2.26) was used to provide tree height and extinction estimates. The obtained average extinction may be then used for the rest of the test site for inverting the complete RVoG model while retrieving height and ground contribution, or, the RVoG model inversion can be performed with a fixed small ground-to-volume ratio. Generally, inversion that utilizes a fixed ground-to-volume ratio is expected to provide more stable results since shadowed areas and forest borders introduce large errors during the complete RVoG model inversion. The RVoG inversion for tree height is quite insensitive to small values of  $M$ , but estimates for extinction using the same assumptions become unreliable. As for the fixed but small ground contribution, in the algorithm we let  $M$  span from 0.01 to 0.1. However, it should be noted that the numerical values of the inversion process parameters might vary for different SAR measurement and forest type and density configurations. The flowchart of the proposed forest parameter retrieval algorithm is shown in Figure 2.5.

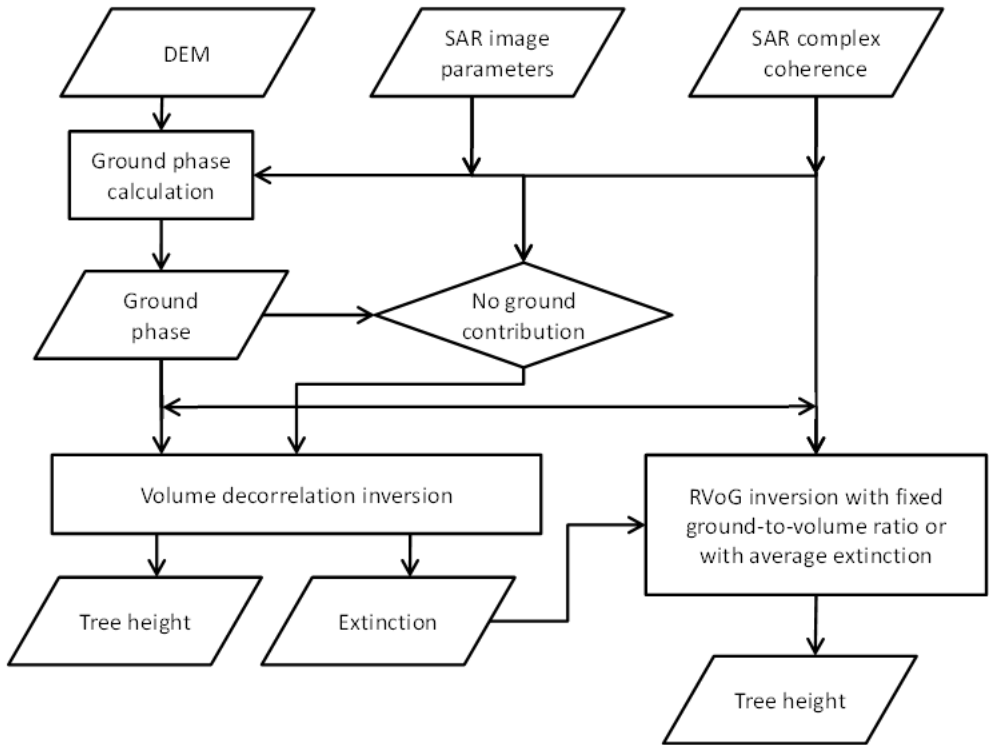


**Figure 2.5.** The proposed forest tree height retrieval algorithm (Paper V).

## 3. Results and discussion

Here, main results reported in Papers I–V are briefly presented and discussed, along with their implications to routine use of PolSAR data in land cover and forest mapping.

### 3.1 Generalized volume scattering model in PolSAR decompositions

The modified three-component decomposition with suggested GVSM was compared with two other approaches: the conventional three-component Freeman-Durden decomposition and the Freeman-Durden decomposition with modification of the volume scattering model after Yamaguchi *et al.* [34] (further called as the Yamaguchi three-component decomposition). No empirical power restrictions as in [34], [141] were used in evaluation of comparative performance of decompositions, and in case that either  $P_d$  or  $P_s$  are estimated to be negative they were clipped to zero.

#### 3.1.1 Qualitative comparison

As an example, the color coded representations of the Freeman-Durden and GVSM three-component decompositions of the May 2007 PolSAR image of Kuortane area with 5x5 analyzing window are shown in Figure 3.1. The latter appears to be less green, with urban and field areas identified more clearly, as the level of volume scattering power decreased up to 8% for some areas (about 2% for the whole scene in average). The Yamaguchi three-component decomposition provided practically the same results (not shown here) as the Freeman-Durden approach, with less than 3% of the data falling into the dynamic range where modification of the volume scattering component can be applied (a histogram for corresponding PolSAR image is shown in Figure 3.2).

As expected, volume scattering was the dominating contribution in the total backscatter for forested areas. Surface scattering dominated most for agricultural areas and peatlands. Backscatter for water areas was relatively small, and surface scattering was identified to be dominating for the majority of water pixels. A good fit to the surface scattering mechanism can be explained by the presence of wind.

The double-bounce mechanism was found to be not an important contribution in boreal forest areas, with high returns obtained mostly in urban areas. Pixel wise comparison of areas belonging to the urban class was the most challenging, as averaging influences it most because of the sparse and discontinuous nature of settlements and the presence of mature trees near summer cottages and single-family houses. As a result, volume scattering masks double bounce contribution for majority of urban class pixels.

Visual inspection shows that use of GVSM for description of the volume scattering contribution practically does not change the qualitative behavior of forested areas. It mostly affects areas where returns from several contributions are almost equal (mostly bordering regions and urban areas), and the corrected remainder covariance matrix can be assigned either double-bounce or surface scattering mechanism depending on the sign of the HH-VV correlation term.

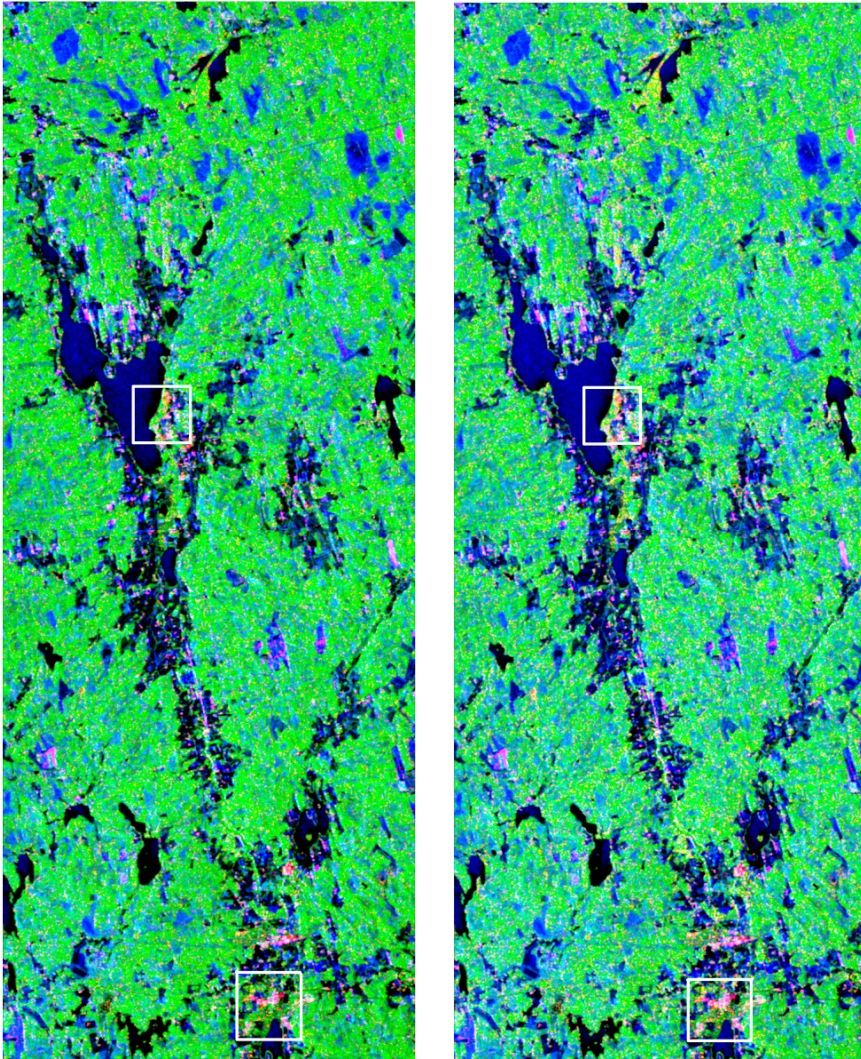


**Figure 3.1.** Color coded representations of decomposed PolSAR image ( $45 \times 17.5 \text{ km}^2$ ) over Kuortane acquired in May 2007 using the Freeman-Durden (left) and GVSM (right) approaches; double-bounce scattering contribution depicted in red color, volume in green, and surface in blue (Paper I).

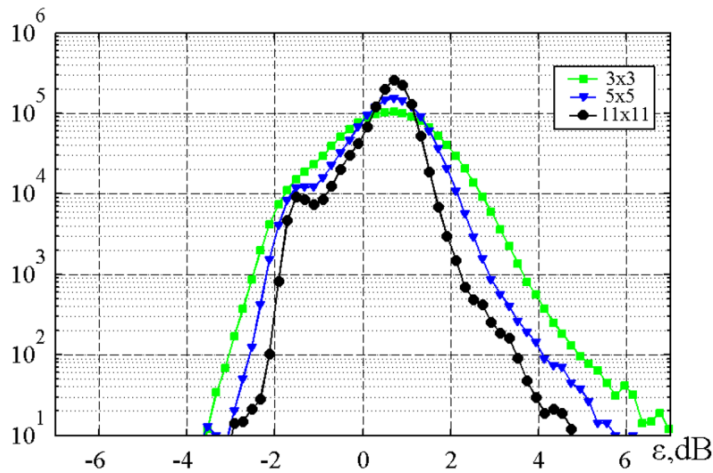


**Figure 3.2.** Histogram of HH-VV ratio as a function of  $\varepsilon$  for the averaged PolSAR image, averaging window size: 3x3, 5x5, 11x11 (Paper I).

### 3.1.2 Eigenvalue non-negativity constraint for the remainder covariance matrix

Although the visual inspection provides some insight into the relative performance of considered decompositions, it is very important to define some quantitative criteria for comparison as well. Here, eigenvalue non-negativity criterion from [35] was used for testing the physical consistency of the covariance matrix decompositions at each decomposition step. If any eigenvalue of the remainder covariance matrix (once volume contribution was subtracted) is negative, the pixel is considered as ill-posed. Results of calculations for two PolSAR images of Kuortane area, acquired on November 11, 2006 and May 14, 2007, using various averaging windows, are shown in Table 3.1.

**Table 3.1.** Percentage of pixels with non-negative PolSAR covariance matrix eigenvalues for the Kuortane study site (Paper I).

Decomposition method	Averaging window size			
	3x3	5x5	11x11	25x25
<b>May 2007 data set</b>				
Freeman-Durden	60,16	71,87	88,51	99,02
Yamaguchi (3-component)	64,35	73,07	88,57	99,02
GVSM (3-component)	69,02	81,31	96,04	99,98
<b>November 2006 data set</b>				
Freeman-Durden	74,10	87,23	98,63	99,96
Yamaguchi (3-component)	77,32	87,93	98,64	99,96
GVSM (3-component)	79,95	91,45	99,31	99,98

The overwhelming majority of pixels with the ill-posed covariance matrices in both PolSAR images belong to strongly vegetated areas. Connection between occurrence of negative eigenvalues in the remainder covariance matrix and the high level of cross-polarized return from vegetation can be further illustrated using the November 2006 PolSAR image, under frozen conditions in leaf-off season. Here, percentages of correctly processed pixels are significantly higher for all decomposition approaches.

In both data sets of Table 3.1, the advantage given by using GVSM (2.5) instead of the traditional model in the Freeman-Durden decomposition can be followed. The Yamaguchi modification of the volume scattering model gives intermediate results, with difference between the Freeman-Durden and the Yamaguchi three-component decompositions exponentially decreasing as the size of averaging window grows.

Let us analyze the way GVSM helped to cure the solution when compared to the traditional model of randomly oriented thin dipoles in more detail. One reason is a generally smaller estimate for the volume contribution  $f_v$ . Another reason is the presence of multiplier  $\eta$  in equation (2.8), which allowed to subtract more from the bigger term ( $\langle |S_{hh}|^2 \rangle$  or  $\langle |S_{vv}|^2 \rangle$ ), and less from the smaller one, reducing the probability of either of them becoming negative.

Further, the decrement to  $\langle S_{hh} S_{vv}^* \rangle$  term is also multiplied by the factor of  $\sqrt{\eta}$ . Recall that after van Zyl [25], surface scatter is considered dominant if  $\text{Re}(\langle S_{hh} S_{vv}^* \rangle)$  is positive in the remainder covariance matrix. As in areas dominated by surface scattering  $\eta$  was mostly less than one, then backscatter from the rough surface was easier to identify correctly, as even smaller value was subtracted from  $\langle S_{hh} S_{vv}^* \rangle$ . The same reason worked for the urban areas, dominated by the double-bounce scattering component ( $\eta > 1$ ), thus contributing to better identification with negative value of  $\text{Re}(\langle S_{hh} S_{vv}^* \rangle)$ .

On the other hand, for the L-band forest area backscatter, where majority of ill-posed pixels are obtained, HH to VV ratio was higher than one,  $\eta > 1$ . It means that  $\langle S_{hh} S_{vv}^* \rangle$  is decreased more than in the Freeman-Durden decomposition, as follows from (2.11). It is easy to show using eigenvalue characteristic equation, that an appropriate criterion from [35] can be formulated as  $\langle |S_{hh}|^2 \rangle \langle |S_{vv}|^2 \rangle \geq |\langle S_{hh} S_{vv}^* \rangle|^2$ . After subtraction of the volume scattering contribution, it was observed for majority of pixels in experimental data, that

$\left\langle S_{hh} S_{vv}^* \right\rangle^2$  decreased slightly more than  $\left\langle |S_{hh}|^2 \right\rangle \left\langle |S_{vv}|^2 \right\rangle$ , which seems to be one of the main contributing factors.

Note that this solution of the pixel ill-posedness problem when decomposing PolSAR data is also different from the way adopted in PolSARpro software (provided by ESA, [136]), where the  $\left\langle S_{hh} S_{vv}^* \right\rangle$  term was simply multiplied by the

factor of  $\sqrt{\left\langle |S_{hh}|^2 \right\rangle \left\langle |S_{vv}|^2 \right\rangle} / \left\langle S_{hh} S_{vv}^* \right\rangle^2$ .

The suggestion that speckle noise is mostly responsible for the occurrence of negative eigenvalues can be clearly followed, once the number of the ill-posed pixels is reduced by additional extensive averaging (Table 3.1). It is in line with results in [27], [159], once again illustrating sensitivity of incoherent target decompositions to presence of speckle, though implemented spatial averaging approach makes preservation of scattering mechanism more problematic. As the volume scattering power overestimation is mostly observed in highly vegetated areas, and extensive averaging decreases resolution for both distributed and concentrated targets, one might apply state-of-the-art polarimetric filters, e.g. [160], [161], [162], [163], instead of simple multilooking. However, while preserving resolution for improved image analysis, especially in urban areas in the context of this study, these filters were found to give practically no benefit with respect to the eigenvalue non-negativity criterion for this PolSAR data when compared to simple boxcar filtering. It means that simple spatial averaging should be preferred if there is no specific requirement for preserving resolution. One possible application of the proposed GVSM modification is to use the respective decomposition as a part of polarimetric filtering algorithms preserving dominating scattering mechanism, like the one described by Lee *et al.* [164]. Also, even with very high averaging, some pixels with covariance matrices not satisfying eigenvalue non-negativity constraints still can be found, which might require some external regularization as was pinpointed in [35] or adjustment of the HH-VV correlation term as currently implemented in PolSARpro.

Further, a rule-based classification showed that quite good results can be achieved with summer scene, with forest non-forest mapping overall accuracy reaching 83.42% with the simple use of scattering mechanism powers (or power ratio).

### 3.2 Land cover and soil type mapping using PolSAR data

Supervised classification was performed for three polarimetric images acquired over Kuortane test site using PNN and maximum likelihood classification. The adopted polarimetric features ( $Span/H/A$ ) were calculated over 5x5 spatially averaged coherency matrix. Keeping in mind the performed multilooking during ortho-rectification, the performed amount of averaging is at reasonable level for practical application [159].

Using the described sigma fitting approach the value of sigma was set to 0.01 for PNN. The classification performance was relatively stable for an interval 0.01–0.1, giving quite a broad range of suitable values for sigma parameter of PNN.

### 3.2.1 Relative performance of the maximum likelihood and PNN-based classification

PNN outperformed Gaussian maximum likelihood classification on both of the considered combinations of polarimetric features in practically all of the performed experiments (see Table 3.2). However, the obtained additional gain in accuracy appeared to vary and was sometimes very modest, especially in the multi-class experiments, and also in forest delineation in the late-autumn scene. Aside from the domination of natural terrain with relatively homogeneous texture over majority of the study site area, this can be explained by the quite long radar wavelength, performed multilook processing, and some averaging during calculation of features. It is reasonable to assume that the texture-induced influence to features' pdfs is decreased with higher amount of averaging, analogously to the similar effect on the SAR data itself [23]. Note that the multilook effect on the polarimetric feature values was not corrected here, which can be a further interesting extension of the study keeping in mind the work presented in [165]. The PNN approach is expected to be of significant utility in complicated non-homogeneous land cover classes, particularly when SAR imaging is performed at shorter wavelengths. Then, an additional advantage can be use of appropriate SAR speckle filters [166], applying differentiated strategies towards filtering based on the scattering mechanisms and local textural and statistical characteristics of PolSAR data.

**Table 3.2.** Classification summary for different combinations of polarimetric features for PolSAR imagery acquired over the Kuortane study site (Paper IV).

CLASSIFICATION EXPERIMENT	SPAN, ALPHA ANGLE, ENTROPY, ANISOTROPY			SPAN, SURFACE SCATTERING FRACTION, SCATTERING DIVERSITY, ANISOTROPY		
	Nov. 2006	March 2007	May 2007	Nov. 2006	March 2007	May 2007
<b>Maximum likelihood</b>						
5 classes	79.68	76.70	79.94	79.46	76.30	79.15
forest/non-forest	88.51	85.25	88.74	88.32	84.91	88.07
soil type under vegetation	66.26	58.90	57.06	64.89	58.54	57.05
<b>Probabilistic neural network</b>						
5 classes	81.87	78.99	82.65	81.75	78.78	82.58
forest/non-forest	89.35	88.10	90.83	89.18	87.91	90.93
soil type under vegetation	70.03	62.51	58.21	70.18	62.77	58.22

A comparatively strong improvement provided by PNN was observed in soil type classification experiments on November and March scenes. Thus, PNN was able to capture some variation under forest canopy beyond that can be provided by simple parametric models. In multi-class experiments more detailed visual inspection revealed particular improvements in identification of urban class areas, and slightly less confusion observed between peatland and agricultural areas.

It should be noted that performance of PNN appears to be crucially dependent on the choice of training data. If selected training data were not representative enough, then obtained results could be even worse than when using simple parametric model, as the latter appears to be more robust in this sense. The problem can be tackled by increasing the number of training data sets, as it also decreases influence of outliers on pdf estimation. However, in practical situations the common problem is lack of the training data, and degraded computational performance of the PNN model when number of hidden layer neurons is too big.

Also, when sigma was set a value higher than optimal, the results provided by PNN tended to be closer to the ML-provided results. This was expected, indicating that under additional extensive averaging Gaussian model for polarimetric features is observed more clearly.

### **3.2.2 Temporal variability of the classification performance**

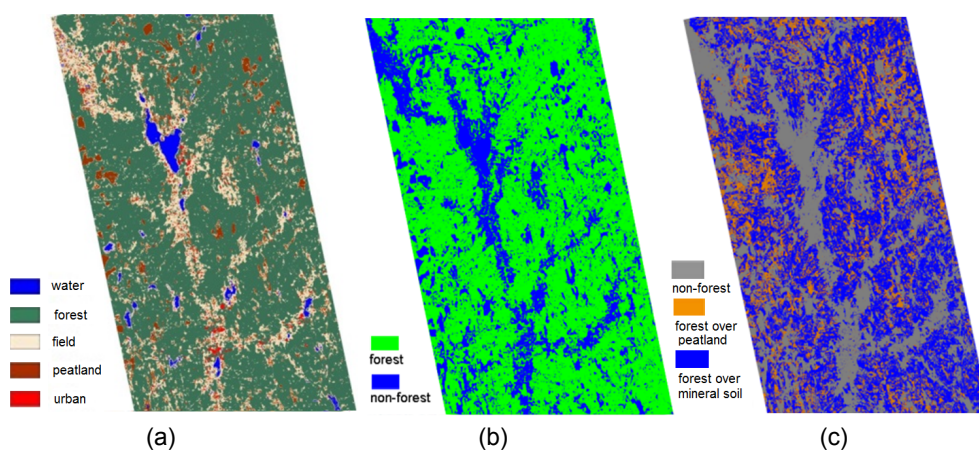
The best classification results in multiclass classification were obtained for the May 2007 data set, with the overall accuracy of 82.65% (see Table 3.2). The corresponding thematic map is shown in Figure 3.3(a). Kappa coefficient of agreement was 0.62. Table 3.2 shows a detailed picture of classification performance for different land cover categories. Some mixing occurred particularly between sparsely forested areas and field (agricultural) areas, fields and peatland, open bogs and forested peatlands, residential and forested areas. It should be stated, that the obvious disagreement (as discussed in [167]) was much smaller than that is apparent from Table 3.2, because of the presence of many land cover classes exhibiting complicated scattering behavior and an actual need to include the spatial context in the classification. For example, gravel pit areas could qualify both for open field and peatland areas, construction sites exhibit characteristics of both urban and open areas, sparsely forested peatlands balance between peatland and forest classes, not to mention such transitional classes as abandoned fields with active forest regrowth, that could be assigned both agricultural and forest class depending on the state of the transition. In the latter case, e.g., training data for class "forest" included both densely and sparsely forested areas, leading to some observed confusion between forested and open areas even in forest/non-forest classification. In this situation, keeping in mind the possibility of application of the trained classifier over larger spatial area, it is the user's accuracy that provides a more reliable identification of the obtained improvement. The same concerns sparse residential areas present on the study site, as a reference urban class from

### 3. Results and discussion

CLC2006 is essentially a land use class including mature vegetated and flat terrain areas.

In understory soil type determination experiments, higher classification accuracy was obtained for the November scene, followed, with significantly worse performance, by the March scene. It strongly favors frozen state of trees for soil type monitoring under forest cover under observed environmental conditions [168], [169], [170], [171]. There, an area with dominating surface scattering contribution reaches maximum coverage in the November scene, while the late March scene under 6 °C temperature has already ceased to provide high enough level of the canopy transmittance, desirable for the soil-type assessment. The worst results were obtained for May 2007 scene, where the volume scattering contribution dominates most strongly.

These results suggest that selection of the training data should be scene-specific (or season-dependent), in order to assure best classification results. It obviously influences sampling strategies during collection of reference data. However, all maps analyzed in Paper IV (see also Figure 3.3) were produced using the same training data sets for all the PolSAR scenes in each of the classification set-ups, in order to perform more objective analysis of relative classification performance.



- (a) 5-classes land cover/use map;
- (b) forest/non-forest map;
- (c) map of soil types (mineral/peatland) under vegetation

**Figure 3.3.** Classification maps from PolSAR data acquired over Kuortane, with the highest total accuracies (Paper IV).

Also, in a real classification scenario, rather than in a modeling study, an additional improvement in classification accuracy can be obtained using the prior probabilities of classes [172]. It can be readily incorporated both in the ML and PNN-based approaches. This a priori information can be obtained, e.g., from coarse-resolution

remote sensing instruments, previously performed classification, or existing reference map, if these data are available and there are good reasons to assume that no major changes occurred in the mapping area.

### 3.2.3 Inferring soil type properties

Classification results shown in Figure 3.3(c) and Table 3.2 suggest some potential for inferring soil type at L-band, even with a single PolSAR data-take. Results were apparently dependent on soil moisture conditions that influence dielectric permittivity of the matter, with particularly high volumetric soil moisture content in the forested peatlands. While no ground measurements were performed, complicating more detailed analysis because of the significant polarimetric diversity, best classification accuracies were obtained for the November dataset as opposed to earlier results in land cover classification. The better performance of PNN in classification of the November and March scenes suggests that the appropriate pdfs were suitable to describe variation beyond that modeled by use of Gaussian-type distribution, for the respective polarimetric features. This suggests possibility of further improvement, if appropriate statistical analysis is performed for separated ground contribution in the overall backscatter. In order to separate the ground and volume contributions over forested areas, one could employ semi-empirical polarization-sensitive forest compensation procedures, or attempt to separate ground and volume contributions from PolSAR data itself using respective polarimetric decompositions. Influence of the adopted decision rule approach, utilizing relative strengths of the basic scattering mechanisms, was comparatively limited, improving classification accuracy by some 2–4% for different values of parameter  $G$  in the decision rule. This can be explained by the fact that still up to 30% of relatively high and/or dense forest could be found over peatland areas. Also, it is important to keep in mind the influence of understory vegetation layer on soil type discrimination capability, which is expected to be positive, but hard to assess quantitatively.

It should be also recognized that much better performance for the particular application of separating different soil types is expected when using multitemporal approach. The relative dielectric permittivity of soils is primarily dependent upon volumetric soil moisture content [173], and strong seasonal variation in soil moisture dynamics is inherently expected for the soil type classes in question. However, such multitemporal analysis was beyond the scope of this study.

### 3.2.4 Comparison of the polarimetric feature sets

Substitution of the alpha angle and entropy features by alternative polarimetric descriptors [174] practically did not influence classification performance. The combination of scattering diversity and surface scattering fraction provided slightly better results when discriminating water and agricultural areas compared to alpha-entropy analysis; the effect in discriminating open bogs and field areas was mixed, and separation of peatlands and water bodies was slightly worse. Scattering di-

versity, and, probably, more importantly surface scattering fraction also favored surface scattering class slightly stronger compared to the alpha-entropy analysis, giving systematically worse results in forest delineation, and systematically better results in the understory soil-type mapping. All these results were observed when combining these polarimetric features with span and anisotropy. To conclude, no major changes were identified when applying alternative polarimetric features on the study test site using multitemporal L-band data. This suggests that a significant improvement in computational efficiency can be achieved at practically no classification accuracy cost by using these alternative parameters, which can be an important factor once multi-polarization data is collected at an increased volume with future space-borne SAR missions. It also indicates, that polarimetric SAR as a classification and inversion technique and interpretation tool has achieved some degree of maturity, offering a richness of possible target descriptors, and requiring careful consideration on what parameters could be useful in a concrete classification scenario, basing, e.g. on previously obtained results in similar studies.

#### **3.2.5 PolSAR suitability for wide-area land cover mapping**

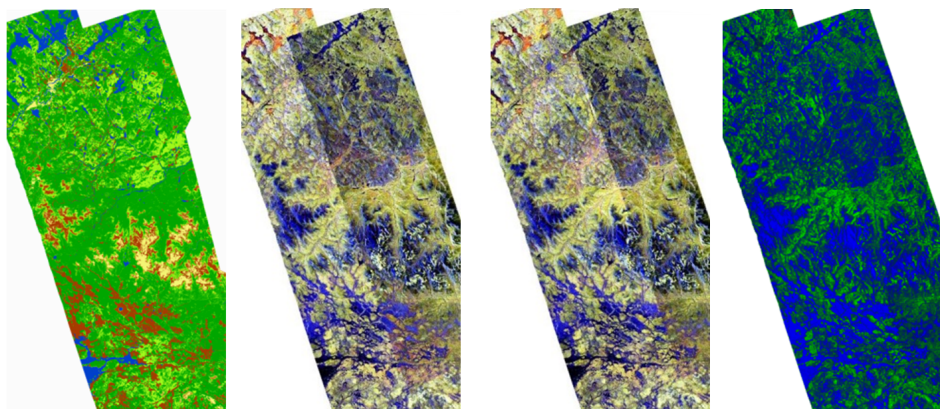
The obtained classification results in land cover and forest mapping compare favorably with results provided by other spaceborne medium resolution remote sensing data. It reveals good potential for producing wide area land cover and forest maps when PolSAR mosaics, as in Paper II, are used. The recent studies indicate that forest and non-forest could be separated using medium resolution satellite data with 80% to 90% overall accuracy. This is valid for the optical, C- and L-band SAR data even when consecutive image acquisitions are available from the same location [167], [175]-[181]. This accuracy range was easily reached in our experiments. The land cover and forest cover classification accuracies range from 50% to 80% depending on the number of classes [181], [182], [183]. While the high classification accuracy of 82.7% achieved for the May 2007 scene can be explained by the primarily forest-dominated environment, an additional space for improvement is possible by performing multitemporal PolSAR classification [43].

#### **3.3 Implication of PolSAR mosaic normalization on thematic mapping**

Results of PolSAR mosaicing study are shown in Figure 3.4. Dominating scattering mechanisms (SMs) were identified using the three-component decomposition (see Paper I) and a simple rule-based approach, with some SM considered dominant if its power accounts for more than 50% of TP in an analyzed resolution cell. The mixed category of pixels appeared to be relatively small and was not used in computing normalization ratios. The implemented approaches allowed obtaining visibly more homogeneous PolSAR data representations when compared to the initial non-corrected mosaic, see Figure 3.4(b),(e).

It is interesting to note that the use of the different model-based decompositions [26], [34], [Paper I] had practically no influence on the pixels' assigned dominating scattering mechanism. It can be explained by the simplicity of the adopted decision rule and the composition of the land cover classes in the scene, mostly characterized by a mixture of volume and surface scattering. Majority of pixels in the overlapping areas were found to preserve their dominant SM, despite, e.g., the actual change in snow wetness. Use of total power with preservation of dominating SM allowed excluding pixels demonstrating strong seasonal change (e.g. jammed ice in the north of the mosaic transferring to open water areas). Some residual imbalance in the south-eastern scene can be explained by influence of the relatively mountainous area in the overlapping area between left- and right-orbit scenes.

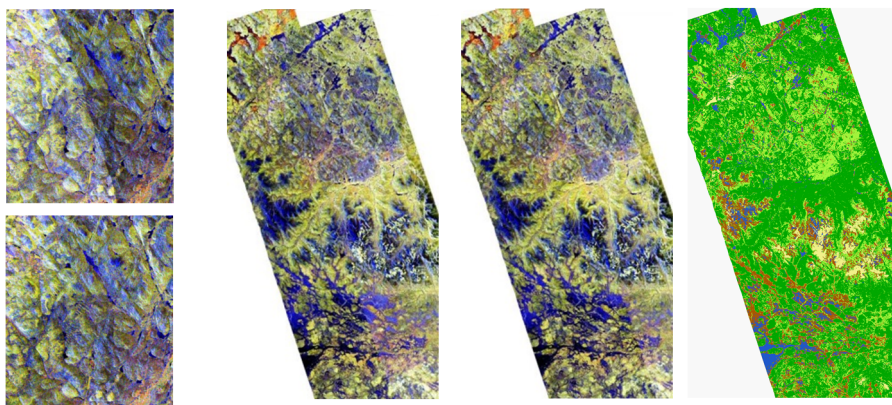
Classification results for both combinations of the polarimetric mosaic along with corresponding normalized versions are collected in Table 3.3, both for multi-class and forest-nonforest classification, with three polarimetric seam-hiding approaches used to correct the mosaic.



**(a)** Reference land cover/use map: blue – water; brown – peat land; light green – sparse forest; dark green – dense forest; yellow – other. © SYKE

**(b)** Pauli RGB representations of the PolSAR mosaic without seam-hiding: (left image) near-range data on top, (right image) far-range data on top. HH-VV is depicted in red, HV in green, HH+VV in blue. © JAXA and METI 2007.

**(c)** Color-coded composite of the PolSAR mosaic: red – double-bounce, green – volume, blue – surface contributions to TP.



**(d)** Enlarged fragments of the mosaic: (up) original; (down) normalized. Color legend follows (a). © JAXA and METI 2007.

**(e)** Pauli RGB representation of the PolSAR mosaic after seam-hiding procedure, normalization strategy after Method 3 is used: (left image) near-range data on top, (right image) far-range data on top. HH-VV is depicted in red, HV in green, HH+VV in blue. © JAXA and METI 2007.

**(f)** Result of supervised classification from PolSAR mosaic shown in (e), right. Color legend follows (a).

**Figure 3.4.** Land cover mapping from fully polarimetric SAR mosaic produced from ALOS PALSAR data acquired over Saariselkä (Paper II).

**Table 3.3.** Results of PolSAR mosaic based land cover classification of the Saariselkä study site, with the overall accuracy estimates given both for multi-class and forest-nonforest (in brackets) classification (Paper II).

	Original	Method 1	Method 2	Method 3
<b>Mosaic 1, Figure 3.4(b)(e), left</b>				
Target decomposition + Wishart + labeling	61.4% (79.2%)	63.3% (81.0%)	63.9% (82.1%)	64.6% (83.4%)
Supervised Wishart	63.1% (81.4%)	65.1% (83.7%)	65.6% (84.5%)	66.7% (85.9%)
<b>Mosaic 2, Figure 3.4(b)(e), right</b>				
Target decomposition + Wishart + labeling	64.4% (83.0%)	65.6% (84.2%)	65.9% (84.4%)	67.2% (86.1%)
Supervised Wishart	66.4% (85.1%)	68.1% (87.0%)	67.7% (86.4%)	69.5% (88.8%)

In supervised Wishart classification a total of 24 training sets covering the whole area of the mosaic were used, representing about 14 thousand out of more than 8 million available pixels. As expected, the supervised classification has provided better classification results, though the difference appeared to be not very significant compared to the unsupervised approach, and generally heavily dependent on the choice of training data. The obtained results emphasize an important role of the total power in PolSAR data classification, often neglected when using pure target model based decompositions, as well as some statistical classification approaches utilizing selected polarimetric features. Application of the proposed polarimetric seam-hiding allowed increasing classification accuracy by some 2.8–3.6%, with the best results obtained for the PolSAR mosaic normalization strategy employing **Method 3**. While these results need further validation in different natural or semi-natural environments, they provide a good insight into what can be expected from polarimetric seam-hiding approaches suggested in Paper II.

As for the relatively low overall classification accuracy, it can be considered the best one attainable under the given seasonal conditions taking into account the multitemporal nature of the mosaic, as well as the original nature of the reference data. Moreover, it is generally difficult to associate available ecological classes to the obtained radar target classifier [50]. For example, the difference in definition of sparse and dense forests is quite technical (percentage of canopy cover and tree height thresholds), and can be hard to capture adequately by radar. Kappa coefficients of agreement [184] were from fair to moderate in all the performed classifications. An additional gain in accuracy of about 3% was achieved when a straightforward water detection based on total backscattered power was utilized, as, e.g.,

in [185], allowing circumventing the confusion between peat land and watered areas.

It is also interesting to note the difference in classification performance of the two versions of the mosaic. In overlapping areas mostly densely and sparsely forested areas were dominating, and the far-range PolSAR data demonstrated slightly higher sensitivity to presence of vegetation than near-range. For the near range data the observed higher confusion between forested and open areas is explained by the higher incidence angle and generally high penetration through canopy at L-band. It resulted in overall higher accuracies for the given land cover composition when far-range areas were used.

## 3.4 Robust SAR-based forest stem volume retrieval

### 3.4.1 General model fitting performance

The model fitting performance is illustrated in Figure 3.5. It shows the results both of the forward model fitting (2.16) and of the inverted model fitting (2.18) along with the models predictions for the training dataset using SAR image acquired over Kuortane on June 27, 2007, HH-polarization. When fitting model (2.15) to the training data, the estimated parameters were  $\sigma_{veg}^0 = -5.8$  dB,  $\sigma_{gr}^0 = -8.3$  dB and  $\beta = 0.031$ , while use of model (2.17) resulted in a slightly broader dynamic range and less curved exponent:  $\sigma_{veg}^0 = -4.6$  dB,  $\sigma_{gr}^0 = -9.1$  dB and  $\beta = 0.011$ . Similar behavior is generally expected for the validation dataset as well, provided that the training dataset is representative enough.

Visual inspection of Figure 3.5 shows that there were a number of forest stands for which stem volume prediction was not possible, analogously to the situation described in [95]. These stands were the ones that had backscatter values outside the dynamic range  $[\sigma_{gr}^0 \dots \sigma_{veg}^0]$ . They are shown with zero stem volume on X-axis in Figure 3.5(c). While this situation is not acceptable in an operational scenario, one possible solution is to set some predefined value for all such stands that exhibit backscatter higher than the backscatter that could be estimated by the model [94]. That value could be, e.g., the maximum stem volume for a stand from the training dataset, or an apparent saturation point value. When using fitting of the inverted model, no such problem occurred, see Figure 3.5(d), though the inverted model predictions of backscatter seem to agree less well. Visual inspection of Figure 3.5 also confirms a systematic bias toward lower estimates noted in [95] when model (2.15) was used. On the other hand, one can observe a bias towards overestimation of stands with a stem volume lower than 100 m<sup>3</sup>/ha when model (2.17) was used in fitting the data. Thus, the main benefit of using the described approach is in avoiding ill-posed results when performing the model inversion.

Both co-polarized (HH) and cross-polarized (HV) channels produced quite similar results. This is in agreement with results reported in, e.g., [89]. As cross-polarized backscatter is determined by volume scattering from forest canopy, it can be expected to be better correlated to components of the canopy. However, the level of HV-channel amplitude correlation to stem volume appeared to be higher only for the Kuortane test site, and RMSE figures did not differ greatly between polarizations. Over the Heinävesi area with more mature forest stands, the HH-channel was giving relatively better results. For both test sites, the increase of L-band backscatter with increasing forest stem volume saturates somewhere close to 150–200 m<sup>3</sup>/ha, as also supported by earlier investigations [71], [73], [89], [95].

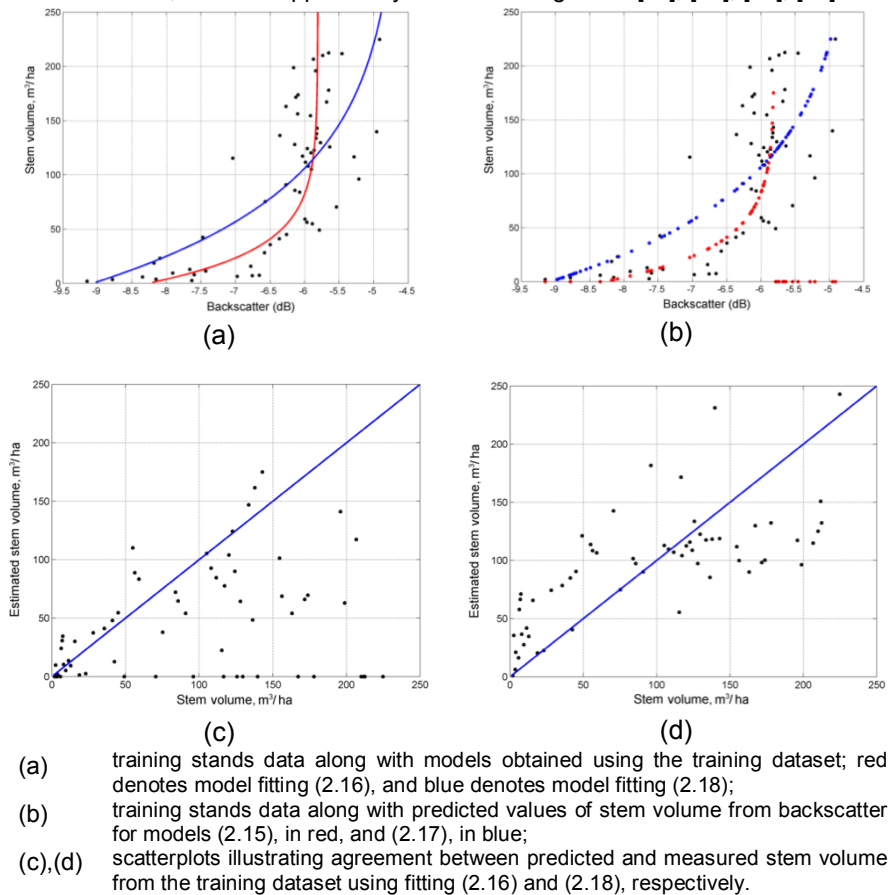


**Figure 3.5.** Model fitting performance for SAR image acquired over Kuortane on 27.06.2007, HH-polarization (Paper III).

Practically no saturation was observed for the Kuortane test site with a lower level of stem volume when cross-validating model predictions against forest inventory data, as shown in Figure 3.6(a). This can be explained by an almost linear de-

### 3. Results and discussion

---

pendence between stem volume and backscatter in the range of 0–150 m<sup>3</sup>/ha when model fitting (2.18) is used. Limiting analysis only to those forest stands where stem volume is between 0 and 200 m<sup>3</sup>/ha gave an improvement of the correlation and RMSE statistics of the HV-channel. This improvement was not so clearly notable in the co-polarized HH data. For example, for a multitemporal regression composite over the Heinävesi test site (Table 3.4, HD<sub>MT</sub>), RMSE improved from 55.9 to 35.6 m<sup>3</sup>/ha for HV-polarization, while for HH-channel the improvement was from 47.0 to 32.7 m<sup>3</sup>/ha. The obtained RMSE of about 30% at stand level indicates a higher suitability of ALOS PALSAR data for mapping low-biomass forest or monitoring of forests at early stages of forest growth.

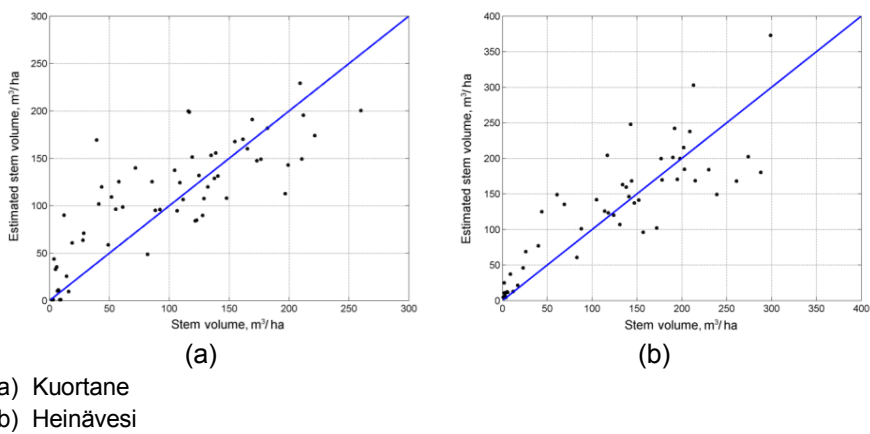


**Figure 3.6.** Scatterplots illustrating agreement between predicted and measured stem volume using validation sets for both study sites, multiple regression (2.19) with HH polarization SAR data used (Paper III).

**Table 3.4.** Stem volume estimation from dual-pol ALOS PALSAR data acquired over the Kuortane and Heinävesi study sites (Paper III).

Scene Id (as in Table 2.1)	Polarization	RMSE, m <sup>3</sup> /ha	RMSE, %	R <sup>2</sup>	Comment
KD <sub>1</sub>	HH	49.7	52.3	0.5	
KD <sub>1</sub>	HV	41.8	44.0	0.64	
KD <sub>2</sub>	HH	45.2	47.6	0.58	
KD <sub>2</sub>	HV	44.4	46.7	0.59	
KD <sub>3</sub>	HH	42.9	45.2	0.62	
KD <sub>3</sub>	HV	42.1	44.3	0.64	
<KD <sub>i</sub> >	HH	42.6	44.8	0.63	ensemble-averaged SAR imagery
<KD <sub>i</sub> >	HV	41.6	43.8	0.64	
KD <sub>MT</sub>	HH	41.2	43.4	0.65	multiple regression
KD <sub>MT</sub>	HV	41.3	43.5	0.65	
HD <sub>1</sub>	HH	65.3	59.4	0.44	
HD <sub>1</sub>	HV	66.7	60.6	0.42	
HD <sub>2</sub>	HH	69	62.7	0.54	
HD <sub>2</sub>	HV	62.6	56.9	0.49	
HD <sub>3</sub>	HH	47.1	42.8	0.71	
HD <sub>3</sub>	HV	56.7	51.5	0.58	
<HD <sub>i</sub> >	HH	55.5	50.4	0.60	ensemble-averaged SAR imagery
<HD <sub>i</sub> >	HV	61.3	55.7	0.51	
HD <sub>MT</sub>	HH	47.0	42.7	0.71	multiple regression
HD <sub>MT</sub>	HV	55.9	50.8	0.59	

Use of both ensemble-averaged imagery and multitemporal regression (2.19) proved to be fruitful, usually improving predictions compared to estimates from individual SAR images (see Table 3.4). The difference was not great, indicating that single-image stem volume retrieval might produce equally good results. However, due to high variability between different dates, multitemporal approach should be favored whenever possible [24],[44],[45]. Inspection of Table 3.4 also suggests the superiority of the multiple regression employed over inversion of ensemble-averaged SAR scenes. Though the improvement was relatively limited, we still expect use of multiple regression of individual predictions (provided by models trained from individual SAR images) to be promising. A particular benefit

could be in the use of multi-seasonal data that can provide higher variation in dynamics of forest backscatter.

Here, as well as in paper III, use of (2.21) in calculating RMSE was justified, as forest stands were approximately the same size, with only few outliers. When the forest stands somewhat vary in size, use of spatial area weighting (2.22) is useful. As it was noted in, e.g., [76], performance of SAR-based estimation over larger forest stands is better. That was also the case both in Kuortane and Heinävesi, as area-weighting in RMSE calculation resulted in improved figures in all the cases. Improvement over the Kuortane test site was very limited, e.g. RMSE for  $KD_1$  (HH-pol) decreased from 49.7 m<sup>3</sup>/ha to 49.4 m<sup>3</sup>/ha, and the best estimate was obtained for  $KD_{MT}$  (HH-pol) as 41.0 m<sup>3</sup>/ha compared to 41.2 m<sup>3</sup>/ha when no area weighting was used. In Heinävesi, the improvement was stronger, e.g.,  $HD_1$  (HH-pol) improved from 65.3 m<sup>3</sup>/ha to 57.8 m<sup>3</sup>/ha, and in the best case  $HD_{MT}$  (HH-pol) improved from 47.0 m<sup>3</sup>/ha to 44.4 m<sup>3</sup>/ha (40.3%). Even better RMSE figures might be reported if area weighting is performed using  $S_i^2$  instead of  $S_i$  in (2.22), however, such weighting strategy should be justified.

#### 3.4.2 Comparison with other stem volume retrieval approaches

The results of this study compare favorably with previous L-band SAR studies in boreal forest. RMSE-values of 30–65% were reported in [95] depending on the imaging mode, with a considerable difference observed between different dates even when the same imaging mode was used. When considering stand-wise stem volume (or biomass) estimation, one should keep in mind the possibility of aggregating produced stand-wise or pixel-wise estimates to larger units, with the idea of producing large-area stem volume maps from SAR mosaics with acceptable accuracy. For instance, [94] has reported an RMSE of higher than 40 t/ha between biomass estimates produced from multitemporal combination of dual-polarization ALOS PALSAR imagery and ground reference data at 150 m pixel resolution. However, when aggregated to county level, the relative RMSE was only 12.9 t/ha.

Comparison is also possible with earlier results from Japanese Earth Resources Satellite (JERS) SAR data at L-band, HH-polarization. RMSE of 59.8 m<sup>3</sup>/ha was obtained in [73] when using a combined multi-date regression approach based on summer scenes at the Ruokolahti study site with stem volume range of 0 – 360 m<sup>3</sup>/ha. Testing was performed using point-wise dataset of stem volume measurements. In the work [76], stem volume was estimated with JERS imagery from a large region of 1 800 km<sup>2</sup> and consisting of 16,000 forest stands with an average area of 4.5 ha and stem volume range of 0–300 m<sup>3</sup>/ha. An RMSE of 56 m<sup>3</sup>/ha was obtained for stands larger than 10 ha. The error increased rapidly with decreasing stand size, but any further increase in the stand size had little effect on the estimation accuracy. In this study, the RMSE was 41.2–47 m<sup>3</sup>/ha using multivariate regression in the case of single HH amplitude, but the average stand size was considerably smaller, 3–4.8 ha depending on the study site. In [85],

a stand-wise stem volume retrieval RMSE of 25% was reported in the study site in Sweden, when a long-term series of JERS SAR imagery was used.

It is also interesting to compare the results obtained in the context of stand-wise stem volume retrieval in boreal forest with optical data. The traditional view is that optical cloud-free data is generally more suitable for retrieval of forest attributes than radar data [186]. However, it appears that accuracies achieved in this study agree well with, or are even superior to, the majority of reported results with optical data in boreal forest. The relative RMSE obtained range from 44.6% to 82% depending on the type of medium resolution optical data employed (e.g., Landsat, ASTER) and the particular stem volume estimation approach adopted (e.g. non-linear multiple regression, neural networks) [187]-[191].

Also, assuming that the SAR-based estimation error is independent of reference ground data error, the corrected error estimate can be calculated. For example, at the Kuortane test site, when fixing the conventional forest inventory error at the level of  $23.6 \text{ m}^3/\text{ha}$ , the corrected RMSE is given as  $\sqrt{41.2^2 - 23.6^2} = 33.8 \text{ m}^3/\text{ha}$ . While validity of these assumptions should be carefully checked, this indicates potential of multi-parametric SAR-based estimation in supplementing conventional stand-wise forest inventory.

### 3.5 Improved forest parameter retrieval using SAR interferometry

Here, we evaluate the performance of forest parameter retrieval approach developed in Paper V and briefly reported in Section 2.2.2.2. In the framework of the suggested RVoG based inversion approach, it was critical to separate areas where ground contribution to complex interferometric coherency is negligible (and the RV model can be used), and those areas where ground contribution is considerable and restricted RVoG inversion with fixed ground-to-volume ratio  $M$  should be implemented.

As experimental data acquired over Kirkkonummi included both single-pass InSAR data acquired at X-band, and repeat-pass InSAR data acquired at L-band, the level of suitability and results obtained differ, and in following are treated in more detail.

#### 3.5.1 X-band InSAR data processing

At X-band, the condition of insignificance of the ground contribution was satisfied over large areas in Kirkkonummi, with relationship between SPC and the LIDAR measured tree height shown in Figure 3.7. Generally, there is a good correlation between SPC and the reference tree height, with SPC located approximately 25% lower than the tree top. However, for canopies lower than 10 m in height the good correlation is lost, and SPC appears to be less than half of the measured tree

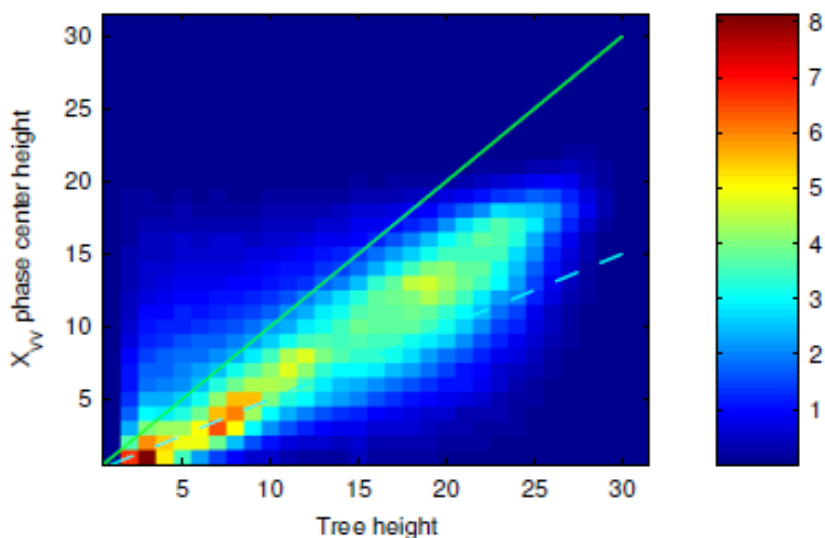
### 3. Results and discussion

---

height. This indicates that for tree stands with height below 10 m, X-band coherence typically already contains a significant ground contribution for boreal forests.

According to the presented boundary cases of the RVoG model, SPC for higher forest is apparently located in the region where ground contribution could be neglected. A further detailed study of the measurements, by also taking into account the coherence amplitude, indicated that the insignificant ground contribution assumption for the RVoG model was fulfilled for several regions.

For those regions, the inversion of the RV decorrelation model was performed in order to retrieve both forest height and extinction coefficient. Figure 3.8(a) shows the distribution of extinction coefficient values retrieved by the described random volume decorrelation model inversion approach. The histogram shows an almost normal distribution with the mean value close to 0.4 dB/m, and with the highest values approaching 0.8 dB/m. Corresponding height values are shown in Figure 3.8(b), indicating that the forest canopies, for which ground contribution can be neglected, are mostly over 20 m high, with practically no trees with tree heights less than 10 m.



The green solid and cyan dashed lines correspond to treetop and half of tree-height locations of the SPC, respectively. One unit on the color bar corresponds to 1000 samples.

**Figure 3.7.** Relationship between interferometric SPC and LIDAR-measured tree height at X-band, VV-polarization InSAR data, Kirkkonummi (Paper V).

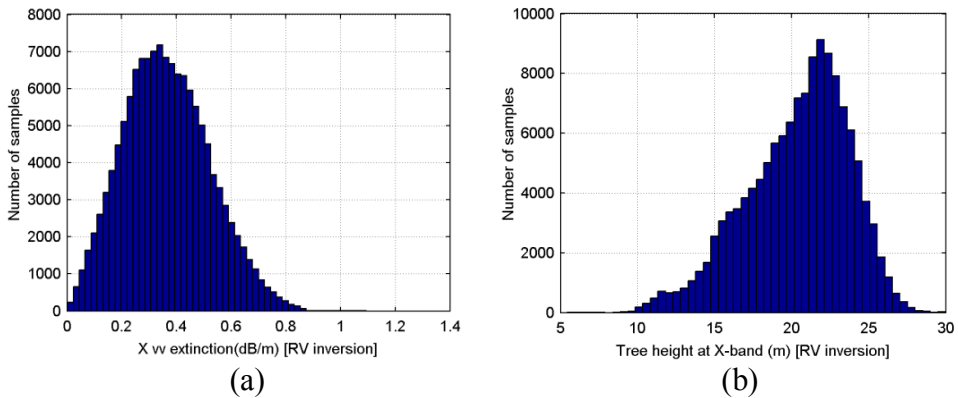


**Figure 3.8.** Random volume model inversion results for areas with negligible ground contribution at X-band, VV-polarization InSAR data, Kirkkonummi (Paper V).

Figure 3.9 shows a pixel by pixel scatterplot between the tree heights retrieved by the volume decorrelation model (2.17) inversion and the corresponding unfiltered LIDAR measured tree heights. The correlation is quite good (Pearson's correlation coefficient  $R=0.83$ ) and no systematic error between these two measurements was noted. This indicates that the insignificant ground contribution assumption for selected areas at X-band is in good agreement with the observations.

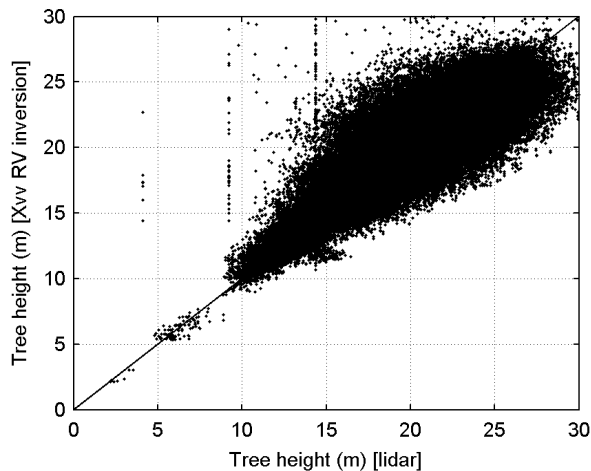


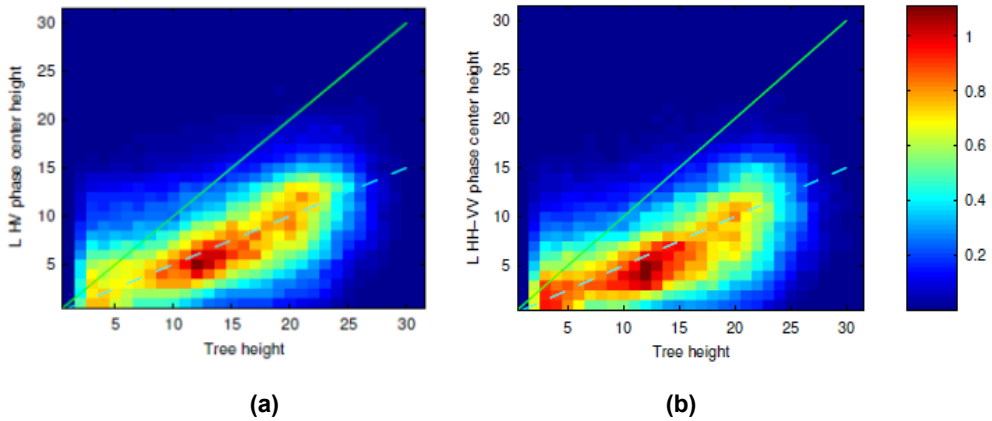
**Figure 3.9.** Relationship between retrieved tree height and LIDAR-measured tree height at X-band for areas with negligible ground contribution, VV-polarization InSAR data, Kirkkonummi (Paper V).

Encouraged by this good correlation, we implemented a simple two stage inversion scheme for single channel X-band data when the ground DEM is known. The first stage of the inversion was performed with the volume decorrelation model (2.26) for areas where the ground contribution was negligible. For the rest of the forested areas we applied the restricted RVoG model inversion, where the value of  $M$  was set to a small predefined number ( $M=0.01$  in this particular case).

An accuracy analysis was performed between the LIDAR measured CHM and the tree height estimates obtained from the proposed combined model inversion approach. The mean extinction coefficient at X-band was estimated to be around 0.4 dB/m, with RMSE = 2.6 m between the obtained InSAR estimates of treetop height and the reference LIDAR measurements. As the processed area represents typical mixed boreal forestland with varying density, an additional analysis was performed on selected homogeneous forest stands, with RMSE approaching 1.5 m. These results are significantly better than the direct interferometric phase height estimates in, e.g., [123], indicating a high potential of quality for the model-based inversion method.

#### 3.5.2 L-band InSAR data processing

The observed relation between the interferometric SPC heights and the LIDAR-measured tree heights is shown in Figure 3.10. Optimum correlation between SPC heights and LIDAR-measured tree heights was obtained using HV polarization. Variability of the SPC height inside the canopy at L-band was clearly larger than at X-band, indicating stronger presence of ground contribution. The SPC height was typically around 50% of the tree height level or just below that. According to the proposed interpretation based on the RVoG model (Section 2.2.2.2), this cannot occur without a ground contribution. However, by applying the *insignificant ground contribution* criterion, few relatively small areas with a high and dense forest on steep slopes in the direction of the incident SAR pulse were found to satisfy the conditions of no-ground contribution. For those areas, the same RV model inversion was performed as for X-band, in order to extract information about the extinction coefficient also at L-band.

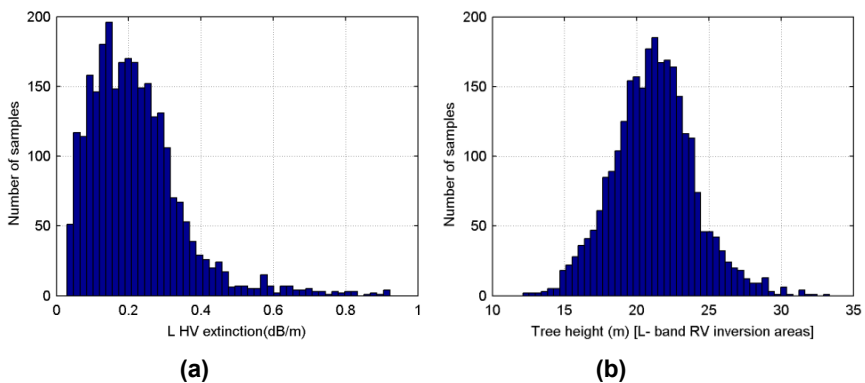


(a) – using HV polarization;  
 (b) – using HH-VV polarization;

The green solid and cyan dashed lines correspond to treetop and half of tree-height locations of the scattering phase center, respectively. One unit on color bar corresponds to 1000 samples.

**Figure 3.10.** Relationship between interferometric SPC and LIDAR-measured tree height at L-band, HH and HH-VV polarizations used, Kirkkonummi (Paper V).

The histogram of extinction coefficient estimates is almost normally distributed as shown in Figure 3.11(a), indicating a stable inversion, with a mean value of 0.18 dB/m at HV polarization and the highest attainable values near 0.6 dB/m. Corresponding height values for the same inversion are shown in Figure 3.11(b).



(a) – histogram of retrieved extinction values;  
 (b) – histogram of retrieved tree heights.

**Figure 3.11.** Random volume model inversion results for areas with negligible ground contribution at L-band, HV-polarization used, Kirkkonummi (Paper V).

### 3. Results and discussion

---

Figure 3.12 shows the pixel by pixel scatter plots between tree height retrieved by the volume decorrelation model inversion and LIDAR measured tree height for the abovementioned polarization combinations. Note the small amount of pixels when compared to the X-band measurement case. The correlation coefficient is at the 0.77 level for HV (0.79 for HH-VV), and there is no systematic error between these two measurements. This indicates that the insignificant ground contribution assumption for the RVoG model appears to be in agreement with these relatively few measurements.

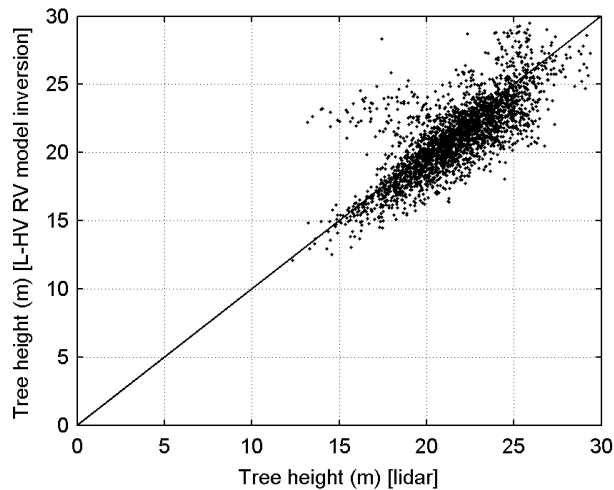


**Figure 3.12.** Relationship between retrieved tree height and LIDAR-measured tree height at L-band (HV-pol) for areas with negligible ground contribution (Paper V).

The same simple two stage inversion scheme was implemented for the L-band HV-polarized measurement (Paper V). The overall height estimation accuracy of this combined approach was 3.4 m when compared to LIDAR measurements, with accuracy better than 2.7 m over selected homogeneous regions. When compared to X-band, the extinction at L-band was relatively low, and appears to be in good agreement with other known studies [105], [192].

## 4. Conclusions

The work described in this thesis was primarily aimed at developing and improving techniques for modeling fully polarimetric backscatter from land cover and forest canopies and retrieving forest cover parameters. Focus was on developing and applying methods in the boreal forest zone. Primarily L-band spaceborne SAR data were used, as it was deemed to be an optimal tool for assessment of forest cover properties in the absence of spaceborne P-band SAR instrument. However, interferometric SAR coherence at X-band proved to be useful tool for retrieval of forest parameters in relatively sparse Finnish forest, and, as such, shows promising potential for use in the other areas of boreal forest biome.

Land cover and forest mapping can benefit from accurate yet simple enough models for interpretation of backscattered signal from terrain. With this idea in mind, in Paper I a new modeling approach and model-based decomposition was suggested, showing improved performance with respect to physical validity of decomposition (physically realizable covariance matrices at each step of decomposition), being quite general to incorporate several previously suggested models, and successfully tested in Finnish boreal forest. Also a simple rule-based approach was suggested, suitable for initial forest-nonforest stratification in an almost automated manner using ratio of retrieved scattering mechanism powers with acceptable accuracy.

L-band forest biomass mapping over wide areas requires accurate mosaicing techniques. Mosaicing of PolSAR data is a step further compared to mosaicing of single- and dual-pol SAR imagery, and can benefit from advanced inter-calibration or normalization techniques between neighboring stripes. Though such normalization techniques are not capable to tackle actual change in scattering phenomena caused by environmental factors, it was shown to improve performance of classification procedures as was demonstrated in Paper II.

High accuracies obtained in general land cover and forest mapping (Paper IV) indicate potential of PolSAR data to be used as primary or even single data source for wide-area mapping, e.g. on the basis of normalized PolSAR mosaics. This is particularly important for intensively cloud-covered areas or polar regions, where optical imagery acquisition is limited. The revisited probabilistic neural network approach (Paper IV) proved useful in capturing non-Gaussian behavior of several polarimetric features, often used in popular PolSAR classification methods. Super-

## 4. Conclusions

---

vised classification with probabilistic neural network proved to be better particularly than standard maximum likelihood based approach, though improvement was relatively limited. The effect is more pronounced over non-homogeneous areas, and is expected to be much stronger at higher resolution with PolSAR imaging instruments operating at shorter wavelengths, with higher levels of texture expected.

Promising results were obtained in mapping soil type (mineral soil and peatland) under vegetation at L-band. A composite classification scheme combining physically motivated rule-based approach followed by ML/PNN classification was implemented for this purpose. While the possibility of inferring soil properties covered by forest should be further supported by extensive ground measurements, we were able to establish a relation between soil-type and several polarimetric features that were previously used in soil moisture mapping. Obviously, there is a high correlation between soil moisture and soil-type, as well as specific forest tree species and forest density.

Paper III concentrated on the development of a robust approach to stem volume retrieval at L-band, with particular focus on multitemporal L-band imagery. A simple semi-empirical model is shown to provide reasonable results also when applied to relatively small forest stands. Particular problems associated with the traditional inversion approach were overcome by using the proposed modification of the model fitting procedure. Multitemporal combination of stem volume estimates obtained from individual SAR scenes proved to be useful and provided better results compared to using estimates from ensemble-averaged SAR scenes. While the best accuracies obtained might not be sufficient for operational forest management, they could be acceptable for making strategic decisions, demonstration and production of large-area forest maps when produced stand-wise stand-volume estimates are aggregated into larger units. The approach presented lays the foundations for producing large-area stem volume maps, both with available data mosaics from ALOS PALSAR as well as with data from future spaceborne missions at L-band.

Investigating behavior of InSAR coherence and SPC against reference LIDAR map in presence of external DEM has allowed developing an effective two-stage inversion procedure in the framework of the RVoG model. This research is described in Paper V. The inversion approach uses both restricted RVoG and simple random volume decorrelation inversion to retrieve tree heights, and also delivers information about the forest extinction. Testing the suggested approach both at X- and L-band using airborne SAR measurements proved suitability of this technique for forest parameter retrieval. At X-band, the accuracy of forest height retrieval was close to 1.5 m, showing good potential for application, e.g., in the TanDEM-X mission.

## 5. Future research

Future research on model-based decompositions should concentrate on further automation and more stability, as the problem of nonnegative eigenvalues seems to be quite solved. One more step is to go further from simple powers of scattering mechanisms to more use of advanced features, such as orientation of scatterers in some preferred direction. Automatic stratification algorithms yet to be demonstrated can be used in initial coarse classification, which can be further improved. This is also very important keeping in mind the possibility of utilizing huge volumes of, e.g., Sentinel-1 data at no cost for users. Also, more effective utilization of decompositions at different frequencies and different applications should be done: crops, ice, snow.

Developed approach for stem volume retrieval should be tested at X- and C-bands, also in order to see where artifacts connected with limited dynamic range of backscattering coefficient still have place.

Algorithm for forest height and extinction retrieval in the boreal forest zone should be further tested and improved with TanDEM-X bistatic SAR interferometric data, with some early results already reported in the literature. Also, if forest appears to be nonhomogeneous, an initial stratification or segmentation step can be applied, based on optical satellite data for different forest species. On the second step, the proposed two-stage inversion algorithm for retrieval of both forest tree height and extinction coefficient might be used.

This is in line with a much broader concept of simultaneous synergetic use of SAR and optical data, which can be done both in physics-based manner, where some parameters of interest are separately retrieved from optical (forest tree species) and SAR (tree height, soil moisture) data, or by simple aggregation of bands followed by segmentation/classification algorithm with further labeling. Optimal ways of fusion of SAR and optical data are yet to be discovered and this area of research needs much more attention.

Also, in order to effectively capitalize on frequent revisiting possibility of new SAR satellite constellations in land cover and forest mapping, effective multitemporal processing techniques should be developed, capable of forming digital multitemporal signatures for land cover classes that can be further used in multitemporal classification methods.

## References

- [1] Y. Pan, R. Birdsey, J. Fang, R. Houghton, P. Kauppi, W. Kurz, O. Phillips, A. Shvidenko, S. Lewis, J. Canadell, P. Ciais, R. Jackson, S. Pacala, A. McGuire, S. Piao, A. Rautiainen, S. Sitch, and D. Hayes, "Large and persistent carbon sink in the world's forests," *Science*, vol. 333, no. 6045, pp. 988–993, 2011.
- [2] S. Quegan, T. Le Toan, "Embedding remote sensing data in models for forest carbon dynamics," *ESA Special Publication*, ESA SP 475, Sheffield, pp. 215–220, 2002.
- [3] A. Rosenqvist, A. Milne, R. Lucas, M. Imhoff, and C. Dobson, "A review of remote sensing technology in support of the Kyoto protocol," *Environmental Science and Policy*, vol. 6, pp. 441–455, 2003.
- [4] T. Le Toan, S. Quegan, I. Woodward, M. Lomas, N. Delbart, G. Picard, "Relating radar remote sensing of biomass to modelling of forest carbon budgets," *Climatic Change*, vol. 67, pp. 379–402, 2004.
- [5] C. Oliver, S. Quegan, "Understanding synthetic aperture radar images," Artech House, 1998.
- [6] J. A. Richards, "Remote sensing with imaging radar," Springer, 2009.
- [7] S. R. Cloude, "Polarisation applications in remote sensing," Oxford University Press, 2010.
- [8] E. Pottier, J.-S. Lee, "Polarimetric radar imaging: From basics to applications," CRC Press, 2009.
- [9] R. F. Hanssen, "Radar interferometry: Data interpretation and error analysis," Kluwer Academic Publishers, Dordrecht, 2001.
- [10] P. A. Rosen, S. Hensley, I. R. Joughin, F. K. Li, S. N. Madsen, E. Rodriguez, and R. M. Goldstein, "Synthetic aperture radar interferometry," *Proc. IEEE*, vol. 88, no. 3, pp. 333–382, Mar. 2000.
- [11] J. S. Lee, W.-M. Boerner, D. L. Schuler, T. L. Ainsworth, I. Hajnsek, K. P. Papathanassiou, and E. Lüneburg, "A review of polarimetric SAR algorithms and their applications," *J. Photogramm. Remote Sens.*, vol. 9, no. 3, pp. 31–80, Sep. 2004.
- [12] [http://www.nrcan.gc.ca/sites/www.nrcan.gc.ca/earth-sciences/files/pdf/resource/tutor/polarim/pdf/polarim\\_e.pdf](http://www.nrcan.gc.ca/sites/www.nrcan.gc.ca/earth-sciences/files/pdf/resource/tutor/polarim/pdf/polarim_e.pdf) [Online] Assessed 9.8.2013

- [13] <http://earth.eo.esa.int/polsarpro/tutorial.html>
- [14] A. C. Frery, A. H. Correia, C. D. da Freitas, "Classifying multifrequency fully polarimetric imagery with multiple sources of statistical evidence and contextual information," *IEEE Trans. Geosci. Remote Sens.*, vol. 45, No. 10, pp. 3098–3109, 2007.
- [15] A. Rosenqvist, M. Shimada, N. Ito, and M. Watanabe, "ALOS PALSAR: A pathfinder mission for global-scale monitoring of the environment," *IEEE Trans. Geosci. Remote Sens.*, vol. 45, no. 11, pp. 3307–3316, 2007.
- [16] M. Shimada, "Advance land-observation satellite (ALOS) and its follow-on satellite, ALOS-2," in *Proc. PolInSAR 2009, ESA Special publication SP-668*, Jan. 2009.
- [17] G. Krieger, I. Hajnsek, K. P. Papathanassiou, M. Younis, and A. Moreira, "Interferometric synthetic aperture radar (SAR) missions employing formation flying," *Proceedings of the IEEE*, vol. 98, no. 5, pp. 816–843, May 2010.
- [18] J. S. Lee, M. Grunes, and R. Kwok, "Classification of multi-look polarimetric SAR imagery based on complex Wishart distribution," *Int. J. Remote Sens.*, vol. 15, no. 11, pp. 2299–2311, Sep. 1994.
- [19] C.-T. Chen, K.-S. Chen, J.-S. Lee, "The use of fully polarimetric information for the fuzzy neural classification of SAR images," *IEEE Trans. Geosci. Remote Sens.*, vol. 41, no. 9, pt. 1, pp. 2089–2100.
- [20] L. Bombrun, J.-M. Beaulieu, "Fisher distribution for texture modeling of polarimetric SAR data," *IEEE Geosci. Remote Sens. Letters*, vol. 5, no. 3, pp. 512–516.
- [21] A. P. Doulgeris, S. N. Anfinsen, T. Eltoft, "Classification with a non-Gaussian model for PolSAR data," *IEEE Trans. Geosci. Remote Sens.*, vol. 46, no. 10, pp. 2999–3009, Oct. 2008.
- [22] A. P. Doulgeris, S. N. Anfinsen, T. Eltoft, "Automated non-Gaussian clustering of polarimetric synthetic aperture radar images," *IEEE Trans. Geosci. Remote Sens.*, vol. 49, no. 10, pp. 3665–3676, Oct. 2011.
- [23] J. S. Lee, D. L. Schuler, R. Lang, and J. Ranson, "K-distribution of the polarimetric SAR imagery," in *Proc. Int. Geosci. Remote Sens. Symp.*, pp. 2179–2181, Aug. 1994.

- [24] S. R. Cloude and E. Pottier, "A review of target decomposition theorems in radar polarimetry," *IEEE Trans. Geosci. Remote Sens.*, vol. 34, no. 2, pp. 498–518, Mar. 1996.
- [25] J. J. Van Zyl, "Unsupervised classification of scattering behavior using radar polarimetry data," *IEEE Trans. Geosci. Remote Sens.*, vol. 27, no. 1, pp. 36–45, Jan. 1989.
- [26] A. Freeman and S. L. Durden, "A three-component scattering model for polarimetric SAR data," *IEEE Trans. Geosci. Remote Sens.*, vol. 36, no. 3, pp. 963–973, May 1998.
- [27] A. Freeman, "Fitting a two-component scattering model to polarimetric SAR data from forests," *IEEE Trans. Geosci. Remote Sens.*, vol. 45, no. 8, pp. 2583–2592, Aug. 2007.
- [28] S. R. Cloude and E. Pottier, "An entropy based classification scheme for land applications of polarimetric SAR," *IEEE Trans. Geosci. Remote Sens.*, vol. 35, no. 1, pp. 68–78, Jan. 1997.
- [29] M. Trudel, R. Magagi, and H. B. Granberg, "Application of target decomposition theorems over snow-covered forested areas," *IEEE Trans. Geosci. Remote Sens.*, vol. 47, no. 2, pp. 508–512, Feb. 2009.
- [30] M. Watanabe, M. Shimada, A. Rosenqvist, T. Tadono, M. Matsuoka, S. A. Romshoo, K. Ohta, R. Furuta, K. Nakamura, and T. Moriyama, "Forest structure dependency of the relation between L-band  $\sigma^0$  and biophysical parameters," *IEEE Trans. Geosci. Remote Sens.*, vol. 44, no. 11, pp. 3154–3165, Nov. 2006.
- [31] I. Hajsek, T. Jagdhuber, H. Schon, and K. P. Papathanassiou, "Potential of estimating soil moisture under vegetation cover by means of PolSAR," *IEEE Trans. Geosci. Remote Sens.*, vol. 47, no. 2, pp. 442–454, Feb. 2009.
- [32] J. D. Ballester-Berman and J. M. Lopez-Sanchez, "Applying the Freeman-Durden decomposition concept to polarimetric SAR interferometry," *IEEE Trans. Geosci. Remote Sens.*, vol. 48, no. 1, pp. 466–479, Jan 2010.
- [33] Y. Yajima, Y. Yamaguchi, R. Sato, H. Yamada, and W.-M. Boerner, "POLARSAR image analysis of wetlands using a modified four-component scattering power decomposition," *IEEE Trans. Geosci. Remote Sens.*, vol 46, no. 6, pp. 1667–1673, June 2008.
- [34] Y. Yamaguchi, T. Moriyama, M. Ishido, and H. Yamada, "Four-component scattering model for polarimetric SAR image decomposition," *IEEE Trans. Geosci. Remote Sens.*, vol. 43, no. 8, pp. 1699–1706, August 2005.

- [35] J. J. van Zyl, Y. Kim, and M. Ariei, "Requirements for model based decompositions," in *Proc. IEEE Geosci. Remote Sens. Symp.*, pp. V-417–V-420, 2008.
- [36] M. Ariei, J. J. van Zyl, and Y. Kim, "A general characterization for polarimetric scattering from vegetation canopies," *IEEE Trans. Geosci. Remote Sens.*, vol. 48, no. 9, pp. 3349–3357, Sept. 2010.
- [37] J. J. van Zyl, M. Ariei, and Y. Kim, "Model-based decomposition of polarimetric SAR covariance matrices constrained for nonnegative eigenvalues," *IEEE Trans. Geosci. Remote Sens.*, vol. 49, no. 9, pp. 3452–3459, Sep. 2011.
- [38] M. Ariei, J. J. van Zyl, and Y. Kim, "Adaptive model-based decomposition of polarimetric SAR covariance matrices," *IEEE Trans. Geosci. Remote Sens.*, vol. 49, no. 3, pp. 1104–1113, Mar. 2011.
- [39] S.-W. Chen, X.-S. Wang, S.-P. Xiao, M. Sato, "General polarimetric model-based decomposition for coherency matrix," *IEEE Trans. Geosci. Remote Sens.*, vol. 52, no. 3, Mar. 2014.
- [40] L. Ferro-Famil, E. Pottier, and J.-S. Lee, "Unsupervised classification of multifrequency and fully polarimetric SAR images based on the H/A/Alpha-Wishart classifier," *IEEE Trans. Geosci. Remote Sens.*, vol. 39, no. 11, pp. 2332–2342, Nov. 2001.
- [41] J. S. Lee, M. R. Grunes, E. Pottier, and L. Ferro-Famil, "Unsupervised terrain classification preserving polarimetric scattering characteristics," *IEEE Trans. Geosci. Remote Sens.*, vol. 42, no. 4, pp. 722–731, Apr. 2004.
- [42] R. Touzi, "Target scattering decomposition in terms of roll-invariant target parameters," *IEEE Trans. Geosci. Remote Sens.*, vol. 45, no. 1, pp. 73–84, Jan. 2007.
- [43] A. Lönnqvist, Y. Rauste, M. Molinier, and T. Häme, "Polarimetric SAR data in land cover mapping in boreal zone," *IEEE Trans. Geosci. Remote Sens.*, vol. 48, no. 10, pp. 3652–3662, Oct. 2010.
- [44] V. Alberga, "A study of land cover classification using polarimetric SAR parameters," *Int. J. Remote Sens.*, vol. 28, no. 17, pp. 3851–3870, Jun. 2007.
- [45] V. Alberga, G. Satalino, and D. K. Staykova, "Comparison of polarimetric SAR observables in terms of classification performance," *Int. J. Remote Sens.*, vol. 29, no. 14, pp. 4129–4150, Jul. 2008.

- [46] I. Guyon, and A. Elisseeff, "An introduction to variable and feature selection," *J. Mach. Learn. Res.*, vol. 3, no. 7–8, pp. 1157–182, 2003.
- [47] L. Bruzzone, and S. Serpico, "A technique for features selection in multiclass problems," *Int. J. Remote Sens.*, vol. 21, no. 3, pp. 549–563, Feb. 2000.
- [48] F. Cao, W. Hong, Y. Wu, and E. Pottier, "An unsupervised segmentation with an adaptive number of clusters using the SPAN/H/ $\alpha$ /A space and the complex Wishart clustering for fully polarimetric SAR data analysis," *IEEE Trans. Geosci. Remote Sens.*, vol. 45, no. 11, pp. 3454–3467, Nov. 2007.
- [49] S. T. Tu, J. Y. Chen, W. Yang, and H. Sun, "Laplacian eigenmaps-based polarimetric dimensionality reduction for SAR image classification," *IEEE Trans. Geosci. Remote Sens.*, vol. 50, no. 1, pp. 170–179, Jan. 2012.
- [50] P. Lumsdon, S. R. Cloude, and G. Wright, "Polarimetric classification of land cover for Glen Affric radar project," *Proc. IEE Radar, Sonar Navig.*, vol. 152, no. 6, pp. 404–412, Dec. 2005.
- [51] M. Ohki, and M. Shimada, "A study of supervised land cover classification by ALOS/Palsar polarimetric interferometry," In. *Proc. EuSAR 2010*.
- [52] M. Takada, Y. Mishima, and S. Natsume, "Estimation of surface soil properties in peatland using ALOS/PALSAR," *Landscape and Ecological Engineering*, vol. 5, no. 1, pp. 45–58, 2009.
- [53] C. Lopez-Martinez, E. Pottier, and S. R. Cloude, "Statistical assessment of eigenvector-based target decomposition theorems in radar polarimetry," *IEEE Trans. Geosci. Remote Sens.*, vol. 43, no. 9, pp. 2058–2074, Sep. 2005.
- [54] D. F. Specht, "Probabilistic neural networks," *Neural Networks*, vol. 3, no. 1, pp. 109–118, 1990.
- [55] P. D. Wasserman, "Advanced Methods in Neural Computing," New York, 1993.
- [56] O. Jiang, E. Aitnouri, S. Wang, D. Ziou, "Automatic detection for ship target in SAR imagery using PNN-model," *Canadian J. Rem. Sens.*, vol. 26, no. 4, pp. 297–305, August 2000.
- [57] Y. Zhang, L. Wu, N. Neggaz, S. Wang, G. Wei, "Remote-sensing image classification based on an improved probabilistic neural network," *Sensors*, vol. 9, pp. 7516–7539, 2009.
- [58] M. Middleton, P. Närhi, R. Sutinen, "Imaging spectroscopy in soil-water based site suitability assessment for artificial regeneration to Scots pine," *ISPRS J. Photogram. Rem. Sens.*, vol. 66, pp. 287–297, 2011.

- [59] G. De Grandi, P. Mayaux, Y. Rauste, A. Rosenqvist, M. Simard, and S. S. Saatchi, "The global rain forest mapping project JERS-1 radar mosaic of tropical Africa: Development and product characterization aspects," *IEEE Trans. Geosci. Remote Sens.*, vol. 38, no. 5, pp. 2218–2233, Sep. 2000.
- [60] P. Siqueira, S. Hensley, S. Shaffer, L. Hess, G. McGarragh, B. Chapman, A. Freeman, "A continental-scale mosaic of the Amazon basin using JERS-1 SAR," *IEEE Trans. Geosci. Remote Sens.*, vol. 38, no. 6, pp. 2638–2644, Nov. 2000.
- [61] M. Shimada, and T. Ohtaki, "Generating large-scale high-quality SAR mosaic datasets: application to PALSAR data for global monitoring," *IEEE J. Sel. Topics Appl. Earth Obs. Remote Sens.*, vol. 3, no. 4, pp. 637–656, Dec. 2010.
- [62] G. De Grandi, A. Bouvet, R. M. Lucas, M. Shimada, S. Monaco, and A. Rosenqvist, "The K&C PALSAR mosaic of the African continent: processing issues and first thematic results," *IEEE Trans. Geosci. Remote Sens.*, vol. 49, no. 10, pp. 3593–3610, Oct. 2011.
- [63] Y. Rauste, A. Lönnqvist, M. Molinier, J.-B. Henry, and T. Häme, "Orthorectification and terrain correction of polarimetric SAR data applied in the ALOS/Palsar context," in *Proc. Int. Geosci. Remote Sens. Symp.*, pp. 1618–1621, 2007.
- [64] J. Koskinen, J. Pulliainen, M. Hallikainen, "Land-use classification employing ERS-1 SAR data," *Photogram. J. Finland*, vol. 14, no. 2, pp. 23–34, 1995.
- [65] M. E. Engdahl, J. Pulliainen, M. Hallikainen, "Segment-based stem volume retrieval in boreal forests using multitemporal ERS-1/2 InSAR data," *Canadian J. Remote Sens.*, vol. 34, no. 1–2, pp. 46–55, 2008.
- [66] C. Dobson, F. T. Ulaby, T. Le Toan, A. Beaudoin, E. S. Kasischke, and N. Christensen, "Dependence of radar backscatter on coniferous forest biomass," *IEEE Trans. Geosci. Remote Sens.*, vol. 30, no. 2, pp. 412–415, 1992.
- [67] H. Israelsson, J. Askne, and R. Sylvander, "Potential of SAR for forest bole volume estimation," *Int. J. Remote Sens.*, vol. 15, no. 14, pp. 2809–2826, 1994.
- [68] Y. Rauste, T. Häme, J. Pulliainen, K. Heiska, and M. Hallikainen, "Radar-based forest biomass estimation," *Int. J. Remote Sens.*, vol. 15, no. 14, pp. 2797–2808, 1994.

- [69] A. Beaudoin, T. Le Toan, S. Goze, E. Nezry, A. Lopes, E. Mougin, et al. "Retrieval of forest biomass from SAR data," *Int. J. Remote Sens.*, vol. 15, pp. 2777–2796, 1994.
- [70] M. Imhoff, "Radar backscatter and biomass saturation: ramifications for global biomass inventory," *IEEE Trans. Geosci. Remote Sens.*, vol. 33, no. 2, pp. 511–518, 1995.
- [71] J. Fransson, and H. Israelsson, "Estimation of stem volume in boreal forests using ERS-1 C- and JERS-1 L-band SAR data," *Int. J. Remote Sens.*, vol. 20, no.1, pp. 123–137, 1999.
- [72] T. Le Toan, A. Beaudoin, J. Riom, and D. Guyon, "Relating forest biomass to SAR data," *IEEE Trans. Geosci. Remote Sens.*, vol. 30, no. 2, pp. 403–411, 1992.
- [73] Y. Rauste, "Multi-temporal JERS SAR data in boreal forest biomass mapping," *Remote Sens. Environ.*, vol. 97, no. 2, pp. 263–275, 2005.
- [74] E. Rignot, J. Way, C. Williams, and L. Viereck, "Radar estimates of aboveground biomass in boreal forests of interior Alaska," *IEEE Trans. Geosci. Remote Sens.*, vol. 32, no. 5, pp. 1117–1124, 1994.
- [75] J. T. Pulliainen, L. Kurvonen, and M. T. Hallikainen, "Multitemporal behavior of L- and C-band SAR observations of boreal forests," *IEEE Trans. Geosci. Remote Sens.*, vol. 37, no. 2, pp. 927–937, 1999.
- [76] L. Kurvonen, J. Pulliainen, and M. Hallikainen, "Retrieval of biomass in boreal forests from multitemporal ERS-1 and JERS-1 SAR images," *IEEE Trans. Geosci. Remote Sens.*, vol. 37, no. 1, Jan. 1999.
- [77] M. Santoro, C. Beer, O. Cartus, C. Schmullius, A. Shvidenko, I. McCallum, U. Wegmüller, and A. Wiesmann, "Retrieval of growing stock volume in boreal forest using hyper-temporal series of Envisat ASAR ScanSAR backscatter measurements," *Remote Sens. Environ.*, vol. 115, no. 2, pp. 490–507, Feb. 2011.
- [78] M. Moghaddam, "Analysis of scattering mechanisms in SAR imagery over boreal forest: results from BOREAS '93," *IEEE Trans. Geosci. Remote Sens.*, vol. 33, no. 5, pp. 1290–1296, Sep. 1995.
- [79] A. C. Morel, S. S. Saatchi, Y. Malhi, N. J. Berry, L. Banin, D. Burslem, R. Nilus, R. C. Ong, "Estimating aboveground biomass in forest and oil palm plantation in Sabah, Malaysian Borneo using ALOS PALSAR data," *Forest Ecology and Management*, vol. 262, no. 9, pp. 1786–1798, 2011.

- [80] R. M. Lucas, J. A. Armston, R. Fairfax, R. Fensham, A. Accad, J. Carreiras, J. Kelly, P. Bunting, C. Clewley, S. Bray, D. Medcalfe, M. Dwyer, M. Bowen, T. Eyre, M. Laidlaw, and M. Shimada, "An evaluation of the ALOS PALSAR L-band backscatter – Above ground biomass relationship Queensland, Australia: Impacts of surface moisture condition and vegetation structure," *IEEE J. Sel. Topics Appl. Earth Obs. Remote Sens.*, vol. 3, no. 4, pp. 576–593, Dec. 2010.
- [81] C. J. Thiel, C. Thiel, C. Schmillius, "Operational large-area forest monitoring in Siberia using ALOS PALSAR summer intensities and winter coherence," *IEEE Trans. Geosci. Remote Sens.*, vol. 47, no. 12, p.1, pp. 3993–4000, 2009.
- [82] M. Santoro, J. E. S. Fransson, L. E. B. Eriksson, M. Magnusson, L. M. H. Ulander, and H. Olsson, "Signatures of ALOS PALSAR L-band backscatter in Swedish forest," *IEEE Trans. Geosci. Remote Sens.*, vol. 47, no. 12, pp. 4001–4019, Dec. 2009.
- [83] J. Carreiras, M. B., Vasconcelos M. J., Lucas R. M., "Understanding the relationship between aboveground biomass and ALOS PALSAR data in the forests of Guinea-Bissau (West Africa)," *Remote Sens. Environ.*, vol. 121, pp. 426–442, 2012.
- [84] S. S. Saatchi, M. Marlier, R. I. Chazdon, D. B. Clark, A. E. Russell, "Impact of spatial variability of forest structure on radar estimation of aboveground biomass in tropical forests," *Remote Sens. Environ.*, vol. 115, no. 11, p. 2836–2849, 2011.
- [85] M. Santoro, L. Eriksson, J. Askne, and C. Schmillius, "Assessment of stand-wise stem volume retrieval in boreal forest from JERS-1 L-band SAR backscatter," *Int. J. Remote Sens.*, vol. 27, no. 16, pp. 3425–3454, 2006.
- [86] S. Enghart, V. Keuck, F. Siegert, "Aboveground biomass retrieval in tropical forests – the potential of combined X- and L-band SAR data use," *Remote Sens. Environ.*, vol. 115, pp. 1260–1271, 2011.
- [87] J. Whitcomb, M. Moghaddam, K. McDonald, J. Kellendorfer, E. Podest, "Mapping vegetated wetlands of Alaska using L-band radar satellite imagery," *Canadian J. Remote Sens.*, vol. 35, No. 1, pp. 54–72, 2009.
- [88] E. J. Rignot, R. Zimmermann, and J. van Zyl, "Spaceborne applications of P band imaging radars for measuring forest biomass," *IEEE Trans. Geosci. Remote Sens.*, vol. 33, no. 5, pp. 1162–1169, 1995.

- [89] G. Sandberg, L. M. H. Ulander, J. E. S. Fransson, J. Holmgren, T. Le Toan, "L- and P-band backscatter intensity for biomass retrieval in hemiboreal forest," *Remote Sens. Environ.*, vol. 115, pp. 2874–2886, 2011.
- [90] Y. Rauste, "Techniques for wide-area mapping of forest biomass using radar data," PhD thesis, *VTT Publications*, vol. 591, Espoo, 2005.
- [91] M. Shimada, T. Tadono, A. Rosenqvist, "Advanced Land Observing Satellite (ALOS) and monitoring global environmental change," *Proceedings of the IEEE*, vol. 98, no. 5, pp. 780–799, May 2010.
- [92] M. Shimada, O. Isoguchi, T. Tadono, and K. Isono, "PALSAR radiometric and geometric calibration," *IEEE Trans. Geosci. Remote Sens.*, vol. 47, no. 12, pp. 3915–3932, 2009.
- [93] M. Shimada, "Advance land-observation satellite (ALOS) and its follow-on satellite, ALOS-2," in *Proc. POLINSAR*, Jan. 2009, ESA Special publication SP-668.
- [94] O. Cartus, M. Santoro, and J. Kelndorfer, "Mapping forest aboveground biomass in the Northeastern United States with ALOS PALSAR dual-polarization L-band," *Remote Sens. Environ.*, vol. 124, pp. 466–478, 2012.
- [95] M. Magnusson, J. E. S. Fransson, L. E. B. Eriksson, G. Sandberg, G. Smith-Jonforsen, and L. M. H. Ulander, "Estimation of forest stem volume using ALOS PALSAR satellite images," in *Proc. Int. Geosci. Remote Sens. Symp.*, 2007, p. 4343–4346.
- [96] D. Zianis, P. Muukkonen, R. Mäkipää, and M. Manuccini, "Biomass and stem volume equations for tree species in Europe," *Silva Fennica Monographs*, vol. 4, pp. 1–63, 2005.
- [97] L. Thirion, E. Colin, and C. Dahon, "Capabilities of a forest coherent scattering model applied to radiometry, interferometry, and polarimetry at P- and L-band," *IEEE Trans. Geosci. Remote Sens.*, vol. 44, no. 4, pp. 849–861, 2006.
- [98] M. L. Williams, "The theory for a forward SAR model: Implementation, applications and challenges," in *Proc. EUSAR*, May 16–18, 2006.
- [99] G. Sun and K. J. Ranson, "Three-dimensional radar backscatter model of forest canopies," *IEEE Trans. Geosci. Remote Sens.*, vol. 33, no. 2, pp. 372–382, 1995.

- [100] Y. C. Lin and K. Sarabandi, "Retrieval of forest parameters using a fractal based coherent scattering model and a genetic algorithm," *IEEE Trans. Geosci. Remote Sens.*, vol. 37, no. 3, pp. 1415–1424, May 1999.
- [101] Y. C. Lin and K. Sarabandi, "A Monte Carlo coherent scattering model for forest canopies using fractal-generated trees," *IEEE Trans. Geosci. Remote Sens.*, vol. 37, no. 1 Part II, pp. 440–451, 1999.
- [102] D. Liu, G. Sun, Z. Guo, K. J. Ranson, and Y. Du, "Three-dimensional coherent radar backscatter model and simulations of scattering phase center of forest canopies," *IEEE Trans. Geosci. Remote Sens.*, vol. 48, no. 1, pp. 349–357, 2010.
- [103] R. N. Treuhaft, B. E. Law, G. P. Asner, and S. Hensley, "Vegetation profile estimates from multialtitude, multifrequency radar interferometric and polarimetric data," *Proc. IEEE Geosci. Remote Sens. Symp.*, vol. 1, pp. 126–128, 2000.
- [104] R. N. Treuhaft, B. D. Chapman, J. R. Dos Santos, F. G. Gonçalves, L. V. Dutra, P. M. L. A. Graça, and J. B. Drake, "Vegetation profiles in tropical forests from multibaseline interferometric synthetic aperture radar, field, and Lidar measurements," *J. Geophys. Res. D Atmos.*, vol. 114, no. 23, 2009.
- [105] R. N. Treuhaft, S. N. Madsen, M. Moghaddam, and J. J. Van Zyl, "Vegetation characteristics and underlying topography from interferometric radar," *Radio Sci.*, vol. 31, no. 6, pp. 1449–1485, 1996.
- [106] R. N. Treuhaft and P. R. Siqueira, "The vertical structure of vegetated land surfaces from interferometric and polarimetric radar," *Radio Sci.*, vol. 35, no. 1, pp. 141–177, 2000.
- [107] K. P. Papathanassiou and S. R. Cloude, "Single-baseline polarimetric SAR interferometry," *IEEE Trans. Geosci. Remote Sens.*, vol. 39, no. 11, pp. 2352–2363, Nov. 2001.
- [108] S. R. Cloude and K. P. Papathanassiou, "Three-stage inversion process for polarimetric SAR interferometry," *IEE Proc Radar Sonar Navig.*, vol. 150, no. 3, pp. 125–134, 2003.
- [109] M. Brandfass, C. Hofmann, J. C. Mura, and K. P. Papathanassiou, "Polarimetric SAR interferometry as applied to fully polarimetric rain forest data," *Proc. IEEE Geosci. Remote Sens. Symp.*, vol. 6, pp. 2575–2577, 9–13 July 2001.

- [110] I. Hajnsek, F. Kugler, S. K. Lee, and K. P. Papathanassiou, "Tropical forest-parameter estimation by means of Pol-InSAR: The INDREX-II campaign," *IEEE Trans. Geosci. Remote Sens.*, vol. 47, no. 2, pp. 481–493, Feb. 2009.
- [111] T. Mette, K. P. Papathanassiou, and I. Hajnsek, "Biomass estimation from polarimetric SAR interferometry over heterogeneous forest terrain," *Proc. IEEE Geosci. Remote Sens. Symp.*, vol. 1, pp. 511–514, 20–24 Sept. 2004.
- [112] I. H. Woodhouse, S. Cloude, K. Papathanassiou, J. Hope, J. Suarez, P. Osborne, and G. Wright, "Polarimetric interferometry in the Glen Affric project: Results & conclusions," *Proc. IEEE Geosci. Remote Sens. Symp.*, vol. 2, pp. 820–822, 2002.
- [113] J. Askne, M. Santoro, G. Smith, and J. E. S. Fransson, "Multitemporal repeat-pass SAR interferometry of boreal forests," *IEEE Trans. Geosci. Remote Sens.*, vol. 41, no. 7, part I, pp. 1540–1550, 2003.
- [114] F. Garestier, P. C. Dubois-Fernandez, and K. P. Papathanassiou, "Pine forest height inversion using single-pass X-band PolInSAR data," *IEEE Trans. Geosci. Remote Sens.*, vol. 46, no. 1, pp. 59–68, 2008.
- [115] J. Praks, F. Kugler, K. P. Papathanassiou, I. Hajnsek, and M. Hallikainen, "Height estimation of boreal forest: Interferometric model-based inversion at L- and X-band versus HUTSCAT profiling scatterometer," *IEEE Geosci. Remote Sens. Lett.*, vol. 4, no. 3, pp. 466–470, 2007.
- [116] F. Garestier, P. C. Dubois-Fernandez, and I. Champion, "Forest height inversion using high-resolution P-band Pol-InSAR data," *IEEE Trans. Geosci. Remote Sens.*, vol. 46, no. 11, pp. 3544–3559, 2008.
- [117] F. Garestier and T. Le Toan, "Estimation of the backscatter vertical profile of a pine forest using single baseline P-band (Pol-)InSAR data," *IEEE Trans. Geosci. Remote Sens.*, vol. 48, no. 9, pp. 3340–3348, 2010.
- [118] J. Praks, M. Hallikainen, F. Kugler and K. P. Papathanassiou. "X-band extinction in boreal forest: Estimation by using E-SAR POLInSAR and HUTSCAT," *Proc. IEEE Geosci. Remote Sens. Symp.*, pp. 1128–1131, 2007.
- [119] J. Praks, M. Hallikainen, J. Seppänen and J. Hyypä, "Boreal forest height estimation with SAR interferometry and laser measurements," *Proc. IEEE Geosci. Remote Sens. Symp.*, pp V-308–V-311, 2009.

- [120] J. Praks, M. Hallikainen, and X. Yu, "Studies of phase center and extinction coefficient of boreal forest using X- and L-band polarimetric interferometry combined with lidar measurements," in *Proc. POLINSAR*, 2009. European Space Agency, (Special Publication) ESA SP, vol. 668 SP, 2009.
- [121] G. Krieger, I. Hajnsek, K. P. Papathanassiou, M. Younis, and A. Moreira, "Interferometric synthetic aperture radar (SAR) missions employing formation flying," *Proc. IEEE*, vol. 98, no. 5, pp. 816–843, 2010.
- [122] Izzawati, E. D. Wallington, and I. H. Woodhouse, "Forest height retrieval from commercial X-band SAR products," *IEEE Trans. Geosci. Remote Sens.*, vol. 44, no. 4, pp. 863–870, 2006.
- [123] H. Balzter, A. Luckman, L. Skinner, C. Rowland, and T. Dawson, "Observations of forest stand top height and mean height from interferometric SAR and LiDAR over a conifer plantation at Thetford Forest, UK," *Int. J. Remote Sens.*, vol. 28, no. 6, pp. 1173–1197, 2007.
- [124] M. L. Tighe, D. King, H. Balzter and H. McNairn. "Comparison of X/C-HH InSAR and L-PolInSAR for canopy height estimation in a lodgepole pine forest," in *Proc. POLINSAR*, 2009, European Space Agency, (Special Publication) ESA SP, vol. 668 SP, 2009.
- [125] C. G. Brown, K. Sarabandi, L. E. Pierce, "Model-based estimation of forest canopy height in Red and Austrian pine stands using shuttle radar topography mission and ancillary data: A proof-of-concept study," *IEEE Trans. Geosci. Remote Sens.*, vol. 48, no. 3, pp. 1105–1117, Mar. 2010.
- [126] L. A. Bessette and S. Ayasli, "Ultra-wideband and CARABAS II foliage attenuation and backscatter analysis," *Proc. IEEE Radar Conf.*, pp. 357–362. Atlanta, GA, May 1–3, 2001.
- [127] B. Mercer, Q. Zhang, M. Schwaebisch, M. Denbina, and S. Cloude, "Forest height and ground topography at L-Band from an experimental single-pass airborne Pol-InSAR system," *Proc. POLINSAR*, 2009. European Space Agency, (Special Publication) ESA SP, vol. 668 SP, 2009.
- [128] M. Törmä, M. Haakana, S. Hatunen, P. Härmä, M. Kallio, M. Katila, T. Kiiski, M. Mäkisara, J. Peräsaari, H. Piepponen, R. Repo, R. Teiniranta, and E. Tomppo, "Finnish Corine 2006-project: Determining changes in land cover in Finland between 2000 and 2006," *Remote Sensing for Environment Monitoring, GIS Applications and Geology VIII, Proceedings of SPIE*, vol. 7110, pp. 71100V-71100V-12, 2008.
- [129] [Online]. Available: <http://sia.eionet.europa.eu/CLC2006/>.

- [130] P. Härmä, R. Teiniranta, M. Törmä, R. Repo, E. Järvenpää, and M. Kallio, "Production of CORINE2000 land cover data using calibrated LANDSAT 7 ETM satellite image mosaics and digital maps in Finland," in *Proc. Int. Geosci. Remote Sens. Symp.*, Sep. 2004, vol. 4, pp. 2703–2706.
- [131] A. Haara and K. T. Korhonen. "Kuvioittaisen arvioinnin luotettavuus (Reliability of stand-wise forest inventory data, in Finnish). *Metsätieteen aikakauskirja*, vol. 4, pp. 489–508, 2004.
- [132] Y. Rauste, A. Lönnqvist, M. Molinier, J.-B. Henry, and T. Häme, "Orthorectification and terrain correction of polarimetric SAR data applied in the ALOS/Palsar context," in *Proc. Int. Geosci. Remote Sens. Symp.*, 2007, pp. 1618–1621.
- [133] D. Small, "Flattening gamma: Radiometric terrain correction for SAR imagery," *IEEE Trans. Geosci. Remote Sens.*, vol. 49, no. 8, pp. 3081–3093, Aug. 2011.
- [134] J.-S. Lee, M. R. Grunes, T.L. Ainsworth, L.-J. Du, D. L. Schuler, and S. R. Cloude, "Unsupervised classification using polarimetric decomposition and the complex Wishart classifier," *IEEE Trans. Geosci. Remote Sens.*, vol. 37, no. 5, pp. 2249–2258, Sep. 1999.
- [135] L. Ferro-Famil, E. Pottier, and J.-S. Lee, "Unsupervised classification of multifrequency and fully polarimetric SAR images based on the H/A/Alpha-Wishart classifier," *IEEE Trans. Geosci. Remote Sens.*, vol. 39, no. 11, pp. 2332–2342, Nov. 2001.
- [136] E. Pottier, L. Ferro-Famil, S. Allain, S. Cloude, I. Hajnsek, K. Papathanassiou, A. Moreira, M. Williams, A. Minchella, M. Lavallo, and Y.-L. Desnos, "Overview of the PolSARpro v4.0 Software. The open source toolbox for polarimetric and interferometric polarimetric SAR data processing," in *Proc. Int. Geosci. Remote Sens. Symp.*, pp. IV936–IV939, 2009.
- [137] E. Parzen, "On estimation of a probability density function and mode," *Annals of Mathematical Statistics*, vol. 33, pp. 1065–1076, 1962.
- [138] K. Z. Mao, K. C. Tan, and W. Ser, "Probabilistic neural-network structure determination for pattern classification," *IEEE Trans. Neural Networks*, vol. 11, pp. 1009–1016, 2000.
- [139] D. Srinivasan, X. Jin, and R. L. Cheu, "Evaluation of adaptive neural network models for freeway incident detection," *IEEE Trans. Intelligent Transportation Systems*, vol. 5, no. 1, pp. 1–11, Mar. 2004.

- [140] L. Rutkowski, "Adaptive probabilistic neural network for pattern classification in time-varying environment," *IEEE Trans. Neural Networks*, vol. 15, No. 4, pp. 811–827, Jul. 2004.
- [141] W. An, Y. Cui, and J. Yang, "Three-component model-based decomposition for polarimetric SAR data," *IEEE Trans. Geosci. Remote Sens.*, vol. 48, no. 6, June 2010.
- [142] L. Zhang, B. Zou, H. Cai, and Y. Zhang, "Multiple-component scattering model for polarimetric SAR image decomposition," *IEEE Geoscience and Remote Sensing Letters*, vol. 5, no. 4, Oct. 2008.
- [143] S. V. Nghiem, S. H. Yueh, R. Kwok, and F. K. Li, "Symmetry properties in polarimetric remote sensing," *Radio Science*, vol. 27, no. 5, pp. 693–711, Sep./Oct. 1992.
- [144] M. Arii, J. J. van Zyl, and Y. Kim, "Retrieval of soil moisture under vegetation using polarimetric scattering cubes," in *Proc. Int. Geosci. Remote Sens. Symp.*, pp. 1323–1326, 2010.
- [145] Y. Kim and J. van Zyl, "Vegetation effects on soil moisture estimation," in *Proc. Int. Geosci. Remote Sens. Symp.*, 2004, pp. 800–802.
- [146] M. Moghaddam and S. Saatchi, "Estimating subcanopy soil moisture with radar," *Journal of Geophysical Research D*, vol. 105, no. 11, pp. 14899–14911, 2000.
- [147] A. K. Cajander, "Studien über die Moore Finnlands," *Acta Forestalia Fennica*, vol. 2, no. 3, pp. 1–208, 1913.
- [148] A. K. Cajander, "Forest types and their significance," *Acta Forestalia Fennica*, vol. 56, pp. 1–71, 1949.
- [149] Y. Kim and J. van Zyl, "Comparison of forest parameter estimation techniques using SAR data," in *Proc. Int. Geosci. Remote Sens. Symp.*, pp. 1395–1397, 2001.
- [150] J. C. Curlander, "Location of spaceborne SAR imagery," *IEEE Trans. Geosci. Remote Sens.*, vol. GE-20, no. 3, pp. 359–364, July 1982.
- [151] J. Pulliainen, "Investigation on the backscattering properties of Finnish boreal forests at C- and X-band: A semi-empirical modeling approach," Ph.D. dissertation, Rep. 19, Lab. Space Technol., Helsinki Univ. of Technol., Espoo, p. 119, 1994.
- [152] J. Pulliainen, P. Mikkilä, M. Hallikainen, J-P. Ikonen, "Seasonal dynamics of C-band backscatter of boreal forests with applications to biomass

- and soil moisture retrieval," *IEEE Trans. Geosci. Remote Sens.*, vol. 34, no. 6, pp. 758–770, 1996.
- [153] E. Attema and F. Ulaby, "Vegetation modeled as a water cloud," *Radio Sci.*, vol. 13, no. 2, pp. 357–364.
- [154] S. Quegan, T. Le Toan, J. J. Yu, F. Ribbes, N. Floury, "Multitemporal ERS SAR analysis applied to forest mapping," *IEEE Trans. Geosci. Remote Sens.*, vol. 38, no. 2, pp. 741–753, Mar. 2000.
- [155] S. Quegan and J. J. Yu, "Filtering of multichannel SAR images," *IEEE Trans. Geosci. Remote Sens.*, vol. 39, no. 11, pp. 2373–2379, Nov. 2001.
- [156] L. Thirion-Lefevre, E. Colin-Koeniguer, "Investigating attenuation, scattering phase center, and total height using simulated interferometric SAR images of forested areas," *IEEE Trans. Geosci. Remote Sens.*, vol. 45, no. 10, pp. 3172–3179, 2007.
- [157] S. R. Cloude, "Polarization coherence tomography," *Radio Sci.*, vol. 41, 2006.
- [158] T. Mette et al.. "Forest and the random volume over ground – nature and effect of 3 possible error types", Germany: EUSAR, 2006.
- [159] R. Touzi, "Speckle effect on polarimetric target scattering decomposition of SAR imagery," *Can. J. Remote Sens.*, vol. 33, no. 1, pp. 60–69, 2007.
- [160] J.-S. Lee, J.-H. Wen, T. L. Ainsworth, K.-S. Chen, A. J. Chen, "Improved sigma filter for speckle filtering of SAR imagery," *IEEE Trans. Geosci. Remote Sens.*, vol. 47, no. 1, pp. 202–213, Jan. 2009.
- [161] J. S. Lee, M. R. Grunes, and G. De Grandi, "Polarimetric SAR speckle filtering and its implication for classification," *IEEE Trans. Geosci. Remote Sens.*, vol. 37, no. 5, pp. 2363–2373, 1999.
- [162] C. Lopez-Martinez, and X. Fabregas, "Model-based polarimetric SAR speckle filter," *IEEE Trans. Geosci. Remote Sens.*, vol. 46, no. 11, pp. 3894–3907, Nov. 2008.
- [163] G. Vasile, E. Trouve, J. S. Lee, and V. Buzuloiu, "Intensity-driven adaptive-neighborhood technique for polarimetric and interferometric sar parameters estimation," *IEEE Trans. Geosci. Remote Sens.*, vol. 44, no. 8, pp. 1609, 2006.

- [164] J. S. Lee, M. R. Grunes, D. L. Schuler, E. Pottier, and L. Ferro-Famil, "Scattering-model-based speckle filtering of polarimetric SAR data," *IEEE Trans. Geosci. Remote Sens.*, vol. 44, no. 1, pp.176–187, Jan. 2006.
- [165] J.-S. Lee, T. L. Ainsworth, J. P. Kelly, and C. Lopez-Martinez, "Evaluation and bias removal of multilook effect on entropy/alpha/anisotropy in polarimetric SAR decomposition," *IEEE Trans. Geosci. Remote Sens.*, vol. 46, no. 10, Oct. 2008.
- [166] J.-S. Lee, J.-H. Wen, T. L. Ainsworth, K.-S. Chen, and A. J. Chen, "Improved sigma filter for speckle filtering of SAR imagery," *IEEE Trans. Geosci. Remote Sens.*, vol. 47, no. 1, pp. 202–213, Jan. 2009.
- [167] D. H. Hoekman, M. A. M. Vissers, and N. Wielaard, "PALSAR wide-area mapping of Borneo: Methodology and map validation," *IEEE J. Sel. Topics Appl. Earth Obs. Remote Sens.*, vol. 3, no. 4, part 2, pp. 605–617, Dec. 2010.
- [168] J. Way, J. Paris, E. Kasischke, C. Slaughter, L. Viereck, N. Christensen, M. C. Dobson, F. T. Ulaby, J. Richards, A. Milne, A. Sieber, F. J. Ahern, D. Simonett, R. Hoffer, M. Imhoff, and J. Weber, "The effects of changing environmental conditions on microwave signatures of forest ecosystems: Preliminary results of the March 1998 Alaskan aircraft experiment," *Int. J. Remote Sens.*, vol. 11, no. 7, pp. 1119–1144, 1990.
- [169] F. J. Ahern, D. J. Leckie, and J. A. Drieman, "Seasonal changes in relative C-band backscatter of northern forest cover types," *IEEE Trans. Geosci. Remote Sens.*, vol. 31, no. 3, pp. 668–680, May 1993.
- [170] E. Rignot, J. B. Way, K. McDonald, L. Viereck, C. Williams, P. Adams, C. Payne, W. Wood, and J. Shi, "Monitoring of environmental conditions in Taiga forest using ERS-1 SAR," *Remote Sens. Environ.*, vol. 49, pp. 145–154, 1994.
- [171] C. Proisy, E. Mougin, E. Dufrene, and V. le Dantec, "Monitoring seasonal changes of a mixed temperate forest using ERS-SAR observations," *IEEE Trans. Geosci. Remote Sens.*, vol. 38, no. 1, pp. 540–552, Jan. 2000.
- [172] A. H. Strahler, "The use of prior probabilities in maximum likelihood classification of remotely sensed data," *Remote Sens. Environ.*, vol. 10, no. 2, pp. 135–163, 1980.
- [173] I. Hajnsek, "Inversion of surface parameters using polarimetric SAR", PhD thesis, Friedrich-Schiller-Universität Jena, 2001.

- [174] J. Praks, E. Colin Koeniguer, and M. T. Hallikainen, "Alternatives to target entropy and alpha angle in SAR polarimetry," *IEEE Trans. Geosci. Remote Sens.*, vol. 47, no. 7, pp. 2262–2274, July 2009.
- [175] M. Sgrenzaroli, A. Baraldi, G. De Grandi, H. Eva, and F. Achard, "A novel approach to the classification of regional-scale radar mosaics for tropical vegetation mapping," *IEEE Trans. Geosci. Remote Sens.*, vol. 42, no. 11, pp. 2654–2669, 2004.
- [176] T. Häme, Y. Rauste, L. Sirro, and N. Stach, "Forest cover mapping in French Guiana since 1992 using satellite radar imagery," in *Proc. ISRSE Symposium*, Stresa, Italy, 4–9 May 2009.
- [177] M. Simard, S. Saatchi, and G. De Grandi, "The use of decision tree and multiscale texture for classification of JERS-1 SAR data over tropical forest," *IEEE Trans. Geosci. Remote Sens.*, vol. 38, no. 5, pp. 2310–2321, 2000.
- [178] T. Evans, M. Costa, M., K. Telmer, and T. S. F. Silva, "Using ALOS PALSAR and Radarsat-2 to map land cover and seasonal inundation in the Brazilian Pantanal," *IEEE J. Sel. Topics Appl. Earth Obs. Remote Sens.*, vol. 3, no. 4, pp. 560–575, 2010.
- [179] R. Haapanen, A. R. Ek, M. E. Bauer, and A. O. Finley, "Delineation of forest/nonforest land use classes using nearest neighbor methods," *Remote Sens. Environ.*, vol. 89, no. 3, pp. 265–271, Feb. 2004.
- [180] T. Häme, "Final report on forest monitoring in Europe with remote sensing (FMERS)," Centre Earth Obs., Espoo, Finland, 1999.
- [181] T. Häme, J. Kilpi, Y. Rauste, O. Antropov, H. Ahola, M. Rautiainen, L. Sirro, and S. Bounpone, "Improved mapping of tropical forests with optical and SAR imagery, Part I: Forest cover and accuracy assessment using multi-resolution Data," *IEEE J. Sel. Topics Appl. Earth Obs. Remote Sens.*, vol. 6, no. 1, pp. 74–91, Feb. 2013.
- [182] G. Nangendo, A. K. Skidmore, and H. van Oosten, "Mapping east African forests and woodlands – A comparison of classifiers," *ISPRS J. Photogr. Remote Sens.*, vol. 61, 293–404, 2007.
- [183] W. S. Walker, C. M. Stickler, J. M. Kellndorfer, K. M. Kirsch, and D. C. Nepstad, "Large-area classification and mapping of forest and land cover in the Brazilian Amazon: A comparative analysis of ALOS/PALSAR and Landsat data sources," *IEEE J. Sel. Topics Appl. Earth Obs. Remote Sens.*, vol. 3, no. 4, part 2, pp. 594–604, Dec. 2010.

- [184] R. G. Congalton, "A review of assessing the accuracy of classifications of remotely sensed data," *Remote Sens. Environ.*, vol. 37, no. 1, pp. 35–46, 1991.
- [185] P. Mishra, D. Singh, and Y. Yamaguchi, "Land cover classification of PALSAR images by knowledge based decision tree classifiers based on SAR observables," *Prog. Electromag. Res. B*, vol. 30, pp. 47–70, 2011.
- [186] J. Hyypä, H. Hyypä, M. Inkinen, M. Engdahl, S. Linko, and Y.-H. Zhu, "Accuracy comparison of various remote sensing data sources in the retrieval of forest stand attributes," *Forest Ecology and Management*, vol. 128, pp. 109–120, 2000.
- [187] P. Kilpeläinen, and T. Tokola, "Gain to be achieved from stand delineation in LANDSAT TM image-based estimates of stand volume," *Forest Ecology and Management*, vol. 124, pp. 105–111, 1999.
- [188] T. Tokola, and J. Heikkilä, "Improving satellite image based forest inventory by using a priori site quality information," *Silva Fennica*, vol. 31, pp. 67–78, 1997.
- [189] E. Tomppo, M. Nilsson, M. Rosengren, P. Aalto, and P. Kennedy, "Simultaneous use of Landsat-TM and IRS-1C WiFS data in estimating large area stem volume and aboveground biomass," *Remote Sens. Env.*, vol. 82, no. 1, pp. 156–171, 2002.
- [190] P. Muukkonen, and J. Heiskanen, "Estimating biomass for boreal forests using ASTER satellite data combined with standwise forest inventory data," *Remote Sens. Env.*, vol. 99, no. 4, pp. 434–447, 2005.
- [191] H. Mäkelä, and A. Pekkarinen, "Estimation of forest stand volumes by Landsat TM imagery and stand-level field-inventory data," *Forest Ecology and Management*, vol. 196, no. 2-3, pp. 245–255, 2004.
- [192] H. Shinohara, T. Homma, H. Nohmi, H. Hirohara, T. Tagawa, "Relation between L-band microwave penetration / backscattering characteristics and state of trees," In *Proc. Int. Geosci. Remote Sens. Symp. 1992*, 26–29 May 1992, Houston, Texas, USA.

## Errata

The author regrets following typos appearing in the text of published articles:

1. Paper I, page 3847, third sentence in the second paragraph, symbol of parameter " $\gamma$ " is missing. The sentence should be read as "GVSM in the form (8) with additional degree of freedom provided by the use of  $\gamma$  may be further incorporated in two-component modeling experiments in the manner of Freeman [13]."
2. Paper IV, page 4, Figure 2: the word "North" on the right hand side of Figure 2(e) doesn't belong there and should be ignored.



Remote sensing offers a wide range of instruments suitable to meet the growing need for consistent, timely and cost-effective monitoring of land cover and forested areas. One of the most important instruments is SAR technology, where transfer of advanced SAR imaging techniques from mostly experimental small test-area studies to satellites enables improvements in remote assessment of land cover on a global scale.

In this thesis, several methods were developed utilizing Earth observation data collected using such advanced SAR techniques, as well as their application potential was assessed. The focus was on use of SAR polarimetry and SAR interferometry to improve performance and robustness in assessment of land cover and forest properties in the boreal zone. Particular advances were achieved in land cover classification and estimating several key forest variables, such as forest stem volume and forest tree height.



ISBN 978-952-60-5522-0  
ISBN 978-952-60-5523-7 (pdf)  
ISSN-L 1799-4934  
ISSN 1799-4934  
ISSN 1799-4942 (pdf)

**Aalto University**  
**School of Electrical Engineering**  
**Department of Radio Science and Engineering**  
[www.aalto.fi](http://www.aalto.fi)

**BUSINESS +  
ECONOMY**

**ART +  
DESIGN +  
ARCHITECTURE**

**SCIENCE +  
TECHNOLOGY**

**CROSSOVER**

**DOCTORAL  
DISSERTATIONS**